University of Wollongong

Research Online

University of Wollongong Thesis Collection 2017+

University of Wollongong Thesis Collections

2023

Liquid-Solid Triboelectric Nanogenerators

Jing You

Follow this and additional works at: https://ro.uow.edu.au/theses1

University of Wollongong

Copyright Warning

You may print or download ONE copy of this document for the purpose of your own research or study. The University does not authorise you to copy, communicate or otherwise make available electronically to any other person any copyright material contained on this site.

You are reminded of the following: This work is copyright. Apart from any use permitted under the Copyright Act 1968, no part of this work may be reproduced by any process, nor may any other exclusive right be exercised, without the permission of the author. Copyright owners are entitled to take legal action against persons who infringe their copyright. A reproduction of material that is protected by copyright may be a copyright infringement. A court may impose penalties and award damages in relation to offences and infringements relating to copyright material. Higher penalties may apply, and higher damages may be awarded, for offences and infringements involving the conversion of material into digital or electronic form.

Unless otherwise indicated, the views expressed in this thesis are those of the author and do not necessarily represent the views of the University of Wollongong.

Research Online is the open access institutional repository for the University of Wollongong. For further information contact the UOW Library: research-pubs@uow.edu.au

Liquid-Solid Triboelectric Nanogenerators

Jing You

Supervisors:
Prof. K. W. See and Prof. Xiaolin Wang

This thesis is presented as part of the requirement for the conferral of the degree:
PHD

University of Wollongong
Faculty of Engineering and Information Sciences
School of Physics

July 2023

Abstract

The triboelectric nanogenerator (TENG) has emerged as a notable innovation in energy research, converting mechanical energy into electrical energy through the triboelectric effect and electrostatic induction. Of its many variations, the liquid-solid mode TENG has gained significant attention due to its inherent wear resistance, mechanical durability, and consistent operation.

This research provides a focused exploration into the interactions between solids and liquids within the domain of TENGs. Beginning with an overview of TENGs—from the general background to their various operational modes, followed by a comprehensive literature review of solid-liquid TENGs.

Central to this research is the introduction of an equivalent circuit model abstracted for a water-solid mode TENG. Relying on the basic principles of first-order lumped circuit theory, this model describes the TENG as a series of capacitors connected by a water resistor. This model serves as a foundation to understand the main output characteristics and the factors influencing them. To validate this theoretical approach, we developed a three-dimensional water-solid TENG array consisting of multiple single-wire TENGs. This array is efficient at capturing small energy movements from water, thus supporting the accuracy of our theoretical model.

Additionally, we delve into the realm of non-contact TENG designs. A new model, composed of copper rings and a charged dielectric sphere, has been proposed to elucidate the working mechanism of TENGs primarily driven by the effect of electrostatic induction. To complement this, two additional models - the vertical and horizontal double copper rings - are discussed. Using the finite element method, these models are examined in detail, indicating an effective theoretical foundation for understanding and predicting the output performance of non-contact model TENGs for practical applications.

In-depth comprehensive modeling and simulations reveal the characteristics and capabilities of various TENG configurations, particularly highlighting the role of the Electric Double Layer in Solid-liquid contact. Utilizing the Gouy-Chapman-Stern (GCS) Model, the research clarifies the dynamic process in the solid-liquid interfaces of TENGs.

In conclusion, this thesis expatiates a mix of practical experiments and theoretical modeling, suggesting a comprehensive understanding of the electrical behaviors of solid-liquid TENGs, aiming to inspire further innovations and applications in the area of energy harvesting.

Acknowledgments

I would like to express my heartfelt gratitude to my supervisors, Prof. Xiaolin Wang, for his continuous guidance and encouragement, and Prof. K. W. See, for his generous financial support during my PhD period.

I extend my sincere appreciation to my esteemed collaborators, Prof. Zhong Lin Wang and Prof. Jiajia Shao, for their invaluable professional guidance and unwavering academic support on my research project.

A special thanks goes to my colleagues and friends, Dr. Frank Fei Yun, Dr. Lei Chen, Dr. Weiyao Zhao, Dr. Zhi Li, Dr. Zengji Yue, Dr. Jon Knott, Mengyun You, Fangli Zhang, and Xin Guo, for their camaraderie and support throughout this journey.

My deepest gratitude goes out to the staff and administrators at the University of Wollongong, Australian Institute of Innovative Materials (AIIM), Institute for Superconducting and Electronic Materials (ISEM). I am particularly thankful to Prof. Shixue Dou, Prof. Will Price, Dr. Germanas Peleckis, Dr. Zheyin Yu, Crystal Mahfouz, Naomi Davis, and Narelle Badger for their assistance and cooperation.

I am deeply appreciative of Dr. Tania Silver for her invaluable help in editing and polishing my papers.

Finally, I want to acknowledge the unwavering support and encouragement from my parents and my partner Yahua He.

I am also grateful for the financial support received from the International Postgraduate Tuition Awards, which covered the full fee charged by the University for my Doctor of Philosophy degree, and the Faculty Scholarship, which provided stipends during my PhD period.

Certification

I, Jing You, declare that this thesis submitted in fulfilment of the requirements for the conferral of the degree Doctor of Philosophy, from the University of Wollongong, is wholly my own work unless otherwise referenced or acknowledged. This document has not been submitted for qualifications at any other academic institution.

Jing You

July 19, 2023

List of Names or Abbreviations

- **List of Abbreviations**

Abbreviation	**Full name**
TENG	Triboelectric nanogenerator
TENGs	Triboelectric nanogenerators
EDL	Electric Double Layer
SL	Stern Layer
DL	Diffuse Layer
GCS	Gouy–Chapman–Stern
CE	Contact Electrification
Kapton	Polyimide
PTFE	Polytetrafluoroethylene
O-TENG	Oil–solid triboelectric nanogenerator
DC-FluTENG	Direct-current fluid-flow-based TENG
MSDC-TENG	Metal-semiconductor direct-current triboelectric nanogenerator
DEG	Droplet-based electricity generator
ITO	Indium tin oxide
ENG	Electrical nanogenerator
AFP	Amorphous fluoropolymer

DFT	Density functional theory
HOMO-LUMO	Gap between the highest occupied and lowest unoccupied molecular orbitals
BSNG	Bionic stretchable nanogenerator
PDMS	Polydimethylsiloxane
TMS	Triboelectric microfluidic sensor
LS	Liquid-solid-contact
SOS	Save Our Souls
RF	Radio frequency
R-TENG	Rotating triboelectric nanogenerator
RhB	Rhodamine B
Cu	Copper
DI	Deionized
3D	Three-dimensional
EDLCs	Electric double layer capacitors
AC	Alternating current
VDR	vertical double copper ring model
HDR	horizontal double copper ring model
FEM	Finite element method
OC	Open-circuit

SC	Short-circuit

• **List of Symbols**

Symbol	Name	Unit
φ	potential	V
x	distance	m
E_A, E_B	occupied energy levels of electrons	V
E_1, E_2	potential energies for electrons to escape	V
C_P	capacitor of PTFE	F
C_1	capacitor formed at the water/PTFE interface	F
C_2	capacitor formed at the water/aluminium interface	F
R_w	impedance of the water droplet	Ω
R_L	impedance of the external load	Ω
$\mathrm{d}q_{(t)}/\mathrm{d}t$	derivative of the transferred charge with respect to time	C
V_{OC}	open-circuit voltage	V
Q_{SC}	short-circuit	C

	transferred charges	
C_{top}	capacitance near the water-PTFE surface	F
C_i	capacitance of the dielectric	F
$C_{EDLC,t}$	EDLC formed at the water-PTFE interfacial area	F
$C_{EDLC,b}$	EDLC formed at the water−bottom electrode interfacial area	F
R_w	resistance of water	Ω
R_L	external resistance in the external circuit	Ω
S_w	contact area between the water and the PTFE	m^2
S_b	contact area between the water and the bottom electrode	m^2
d_0	effective thickness of the multi-	m

	dielectric layer	
d_1, d_2	thickness of Kapton and PTFE respectively	m
ε_1, ε_2	relative permittivity of Kapton and PTFE respectively	F/m
λ_w	width of the EDLC	m
ε_w	dielectric constant of DI water	F/m
C_{bot}	capacitance formed at the bottom electrode-water surface	F
ε_0	Permittivity of vacuum	F/m
φ_{top}	Voltage across top EDLC	V
φ_{bot}	Voltage across bottom EDLC	V
r_{s}	radii of charged sphere	m
r_{c}	radii of copper rings	m
ρ_{s}	Surface charge density of charged	C/m^2

	sphere	
d	displacement of the sphere	m
h	height between the double vertical copper rings	m
S	horizontal distance between the center of the double copper rings	m
S_0	closest distance between the double horizontal copper rings	m

Table of Contents

List of Tables, Figures and Illustrations

- **List of Figures**

Figure 1.1. Schematic illustration of the first TENG and its operation cycle.

Figure 1.2. Coordination system and mathematical parameters defined for describing (a) contact-separation, (b) lateral-sliding mode, (c) single-electrode mode, (d) free-standing mode, and (e) rolling mode TENGs, respectively.

Figure 1.3. Typical models of an EDL. (a) Schematic of an EDL in a liquid in contact with a positively-charged solid. If the solid is negatively-charged, the charge distribution will be the inverse. Schematic of the (b) Helmholtz plate EDL model, (c) Gouy–Chapman diffuse EDL model, (d) Stern EDL model, and (e) BDM EDL model.

Figure 2.1. Typical liquid-dielectric mode TENG. (a) Schematic diagram of the three-dimensional water-solid TENG array, (b) Typical electrical double layer formed on the water-dielectric interface area and the relevant variation of electrostatic potential φ with distance x from the electrode and (c) The full equivalent circuit model of the water-solid triboelectric nanogenerator. (d) Schematic illustration on the triboelectric mechanism of the FO-TENG (The O-TENG modified with different amounts of Fc(x) and Fs(y) is noted as FO-TENG(x–y)) and (e) transferred charge curves of the FO-TENG compared with other O-TENGs for oil-solid contact. (f) Method for testing the amount of charge on water droplet after L-S friction. (g) Simplified model of the measurement method. The tested material contacts the liquid metal of mercury, and then separates periodically. The positive electrode of the electric meter is connected to the mercury,

and the negative is connected to the copper electrode. (h) The setup of AFM platform for the thermionic emission experiments.

Figure 2.2. Typical liquid-semiconductor mode TENG. (a) The setup of the tribovoltaic experiments and the external circuit, (b) the oscillogram of open-circuit voltage when a DI water droplet slides on the P-type silicon wafer (0.1 Ω cm) at 20 mm/s, and the droplet static contact diameter is 2.5 mm, (d) the oscillogram of short-circuit current when a DI water droplet slides over the P-type silicon wafer (0.1 Ω cm) at 20 mm/s, and the droplet static contact diameter is 2.5 mm. (c) Energy band diagram of the N-type Si and the DI water, (e) the setup of the experiments and (f) a schematic diagram of the generation of tribo-current.

Figure 2.3. Typical liquid-metal mode TENG. (a) Side (left) and top (right) views of a snapshot of the Pt (111)-water interface from a DFTMD trajectory. Pt, watA, watB and watC are colored in grey, blue, magenta and red, respectively. The isosurfaces represent the electron density difference profile of the interface before and after water interacts with the metal surface electronically, and the regions colored in cyan and yellow indicate electron depletion and accumulation, respectively. (b) Schematic showing the experimental setup of DC-FluTENG and (c) structure diagram of DC-FluTENG in comparison with a conventional single-electrode-based TENG.

Figure 2.4. (a) An electron-cloud-potential-well model proposed for explaining CE and charge transfer. d, distance between two nuclei; E_A and E_B, occupied energy levels of electrons; E_1 and E_2, potential energies for electrons to escape. (b) Interatomic interaction potential between two atoms when they are at equilibrium position.

Figure 2.5. (a)-(b) Wang's hybrid EDL model and the "two-step" process on its formation. (a) In the first step, the molecules and ions in the liquid impact the solid surface due to the thermal motion and the pressure from the liquid, which leads to electron transfer between them; meanwhile, ions may also attach to the solid surface. (b) In the second step, free ions in the liquid would be attracted to the electrified surface due to electrostatic interactions, forming an EDL. (c) The setup of the charging experiments, where the negative charges generated on the SiO_2 surface could be electrons and O^- ions induced by surface ionization reaction. ('O' is the Oxygen atom, 'Si' is the silicon atom and 'O^-' is the Oxygen ion). (d) The decay of the CE charge (induced by contacting with the DI water at room temperature) on the SiO_2 surface at different substrate temperatures.

Figure 2.6. Liquid-Solid CE based on Tribovoltaic effect. (a)-(c) The electric output characteristics of the metal-semiconductor-based direct-current triboelectric nanogenerator (MSDC-TENG). (d) The setup of conductive atomic force microscopy experiment platform, the diamond coated tip was controlled to rub on the Si sample with a certain load, during the rubbing, the current between the tip and sample was recorded in the CAFM. (e) The setup of the experiments, the coupling of photovoltaic effect and tribovoltaic effect at the DI water and Si wafer interface under light irradiation and (f) energy band diagram of the N-type Si and the DI water.

Figure 2.7. Equivalent Circuit Model of Liquid-Solid TENG. (a) Schematic diagram of droplet-based electricity generator (DEG) and (b) circuit model, in the switched-off mode, there is no capacitor formed at the water/aluminium interface. As a result, C_P and C_I remain in an open circuit and there is no charge flow between them. When the aluminium electrode and PTFE are connected by the water droplet

(switched-on mode), another capacitor, C_2, is established at the water/aluminium interface, forming a closed circuit. R_w, R_L and $\mathrm{d}q_{(t)}/\mathrm{d}t$ in the circuit are, respectively, the impedance of the water droplet, the impedance of the external load and the derivative of the transferred charge with respect to time. (c) Experimental setup, (d) full equivalent circuit and (e) simplified equivalent circuit of the water drop electricity generator.

Figure 2.8. (a) The diagrams of influential mechanism of the surface charge density on the formation of electric double layer with the solid surface charged much negatively, less negatively, less positively, and much positively. (b) The analysis of the local polarized electric field on SiO_2 surface. (c) The adsorption energy between SiO_2 surface with Na^+ ion, Cl^- ion, and H_2O molecule under different charge densities. (d) Sketch of seven polymers. Polytetrafluoroethylene (PTFE), polypropylene (PP), polyvinylidene difluoride (PVDF), polydimethylsiloxane (PDMS), Nylon 66, polyimide (Kapton), polyethylene terephthalate (PET), and water. The dashed areas depict their monomers.

Figure 2.9. (a) Schematic illustrations of the disk TENG, (b) schematic diagram and (c) the circuit diagram of the TENG-driven water splitting system. (d) Scheme diagram of bionic stretchable nanogenerator (BSNG) with double layer structure, which is mainly constructed by silicone, polydimethylsiloxane (PDMS), electrification liquid and ionic solution electrode. (e) Scheme diagram of the bionic channels in BSNG. (f) Output signal of BSNG in one working cycle

Figure 2.10. (a) Structure of the water wave motion sensor rooted in water wave friction, (b) peak values of voltage and (c) peak values of current for the device. (d) The structure diagram of the hybridized TENG. (e) The dependences of the V_{oc} and

Isc values on the flowing water rate of the disk-TENG. (f) The dependences of *Voc* and *Isc* values on wind speed of the disk-TENG when it is driven by wind. (g) Structural schematic diagram of the liquid rate sensor and gas rate sensor. For liquid rate sensor, the inset 1 shows the photograph of the sensor fabricated on a medical infusion tube, the inset 2 shows the surface SEM image of PTFE layer (scale bar: 5 μm), the inset 3 shows the contact angle which indicates the hydrophobic property of the PTFE surface. For the gas flow rate sensor, the inset 1 shows the photograph of the sensor fabricated on a PE tube, the inset 2 shows the surface SEM image of PTFE layer (scale bar: 3 μm), the inset 3 shows the contact angle of the air bubble on the PTFE surface. (h) 3D graph shows the output frequency of self-powered triboelectric micro-fluidic sensor (TMS) with various capillaries under different external flow rate.

Figure 2.11. TENGs as scanning probe. (a) Working mechanism of the droplet-TENG. When a drop of liquid flows through the polymer surface, the charge transfer between liquid and solid occurred, and the current signals were measured by the two Cu electrodes separately. (b) Working mechanism of the pixeled droplet-TENG. When a water droplet flows through the tilted fluorinated ethylene propylene surface, the charge transfer between liquid and solid occurred, and the induced charges at each point were measured by the electrode arrays on the backside. (c) Structure of the pixeled droplet-TENG: the top layer is dielectric polymer film (FEP film) for contact electrification with water droplet; the middle layer is a PMMA plate, and the Cu electrode array (12 × 36 Cu electrodes) penetrates the PMMA plate; the bottom layer is a signal processor.

Figure 2.12. (a) The blue energy harvested by the network of the liquid-solid-contact buoy triboelectric nanogenerators. (b) The structure of a buoy, the buoy

contains an inner liquid and several polymer films, which function as several TENGs. (c) Illustrations of the R- TENG. (i) the optical image and (ii) the schematic exploded view of the R-TENG which consists of a rotator and a stator. (iii) PCB patterns of the rotator and stator; inserts are the sectional optical images of PCBs. (d) Schematic diagram of the Cu^{2+} and RhB removing powered by transformed and rectified TENG (R&T TENG). (e) Structure of the self-powered microfluidic transport system based on TENG and electrowetting technique to control the mini vehicle carrying a tiny gear.

Figure 3.1. Electrical measurement system includes two parts: (a) digital multimeter and (b) the Labview platform.

Figure 3.2. Liner motor includes two parts: (a) controller of the liner motor and (b) the moving motor.

Figure 3.3. Me3D (Australia) 3D printer consists of a 3-axial stage and motor. The raw materials are driven by the motor which is controlled by a specially designed program on the computer.

Figure 4.1. (a) Schematic diagram of the water-solid triboelectric nanogenerator and (b) photograph of the moving part setup. (c) Typical electrical double layer formed on the water-dielectric interface area and the relevant variation of electrostatic potential (φ) with distance x from the electrode. (d) The full equivalent circuit model of the water-solid triboelectric nanogenerator. (e) Step-by-step illustration showing the working principle of the water-solid triboelectric nanogenerator.

Figure 4.2. (a) Open-circuit voltage (V_{OC}) and (b) short-circuit transferred charges

(Q_{SC}) of the water-solid triboelectric nanogenerator when the areas of the PTFE and Cu are 25 cm^2 and 170 cm^2, respectively. Comparison of the V_{OC} for different (c) material selections, (d) sizes of PTFE, (e) sizes of the bottom electrode. (f) Extracted peaks of V_{OC} and Q_{SC} for different sizes of the bottom electrode. Basic outputs of the (g) V_{OC} and (h) Q_{SC} for different velocities of the moving part. (i) Comparison of the open-circuit voltage densities reported in recent years. Note that the V_{OC} of this work exhibits the largest value.

Figure 4.3. (a) Schematic diagram of the single-wire TENG. Comparison of the (b) V_{OC} and (c) Q_{SC} of the single-wire TENG with increasing immersion length, and (d) corresponding extracted peaks of V_{OC} and Q_{SC}; Note that the depth of DI water is fixed at 14 cm. (e) Extracted peaks of V_{OC} and Q_{SC} at different depths of the DI water.

Figure 4.4. Open-circuit voltage density and transferred charge density of the single-wire TENG at different immersion length, with water depth fixed at 14 cm.

Figure 4.5. Comparison of the (a) open-circuit voltage V_{OC} and the (b) short-circuit transferred charge Q_{SC} of the single-wire TENG with increasing water depth.

Figure 4.6. (a) Schematic diagram of the three-dimensional water-solid TENG array, constructed from many single-wire TENGs. (b) The equivalent circuit model of the TENG array. (c-d) Transferred charges Q_{SC} and the extracted peaks of Q_{SC} enhancement with the increase of the integrated wire number. (e-f) Open circuit voltage V_{OC} and the extracted peaks of V_{OC} with the increase of the integrated wire number.

Figure 4.7. (a) Optical images of a single-wire TENG (left) and a TENG array with

when a charged sphere passes through. (c) – (f) Electric potential and surface charge density of the copper ring when charged spheres with different radii pass through the charged sphere (the radius of the charged sphere, r_s = 0.1 cm, 0.5 cm, and 1.0 cm, while the radius of the copper ring, r_c = 1.5 cm). (g) Distribution of electric potential (*V*) and (*h*) its contours when the sphere is positively charged and negatively charged separately.

Figure 6.3. Simulation results for a charged sphere passing through single copper ring. (a) Electric potential and (b) surface charge density of the copper ring when a charged sphere passes through single copper rings with different radii (r_s = 0.5 cm, r_c = 0.6 cm, 1.5 cm, and 3.0 cm). (c) Electric potential and (d) surface charge density of the copper ring when charged spheres pass through with different charge densities (r_s = 0.5 cm, r_c = 1.5 cm, ρ_s = 1 μC/m2, 10 μC/m2, and 50 μC/m2). (e) Contours of electric potential (V) when charged spheres (ρ_s = 10 μC/m2, r_s = 0.5 cm) pass through single copper rings with different radii (r_c = 0.6 cm, 1.5 cm, and 3.0 cm).

Figure 6.4. Surface charge density for different positions of the copper ring in the single copper ring model.

Figure 6.5. Simulation results for a charged sphere passing through vertical double copper rings (ρ_s = 10 μC/m2, r_s = 0.5 cm, with the radius of the double vertical copper rings the same, r_c = 1.5 cm). (a) Electric potential difference (in the open-circuit condition) and transferred charge density (in the short-circuit condition) between double vertical copper rings when a charged sphere pass through at different heights of the top ring (where the height between the double vertical copper rings, *h* = 0.1 cm, 0.5 cm, 1 cm, 2 cm, and 3 cm). Surface charge density of

different positions on the copper ring under (b) open-circuit (OC) conditions and (c) short-circuit (SC) conditions. (d) Electric potential of vertical double rings in the OC condition when h changes (*h* = 0.5 cm, 2 cm, 3 cm, 5 cm, 10 cm, and 20 cm). (e) three-Dimensional distribution of electric potential (indicated by colors) and electric field (indicated by arrows) when a charged sphere pass through the double vertical copper rings separated by 0.5 cm. (f) Distribution of electric potential under OC conditions when h changes (*h* = 0.1 cm, 1.0 cm, and 3.0 cm).

Figure 6.6. Simulation results for a charged sphere passing through offset double copper rings (ρ_s = 10 μC/m2, r_s = 0.5 cm, with the radii of the double vertical copper rings the same, r_c = 1.5 cm). (a) Electric potential difference between double offset copper rings in the OC condition when the charged sphere passes through at different horizontal offsets s (*s* = 0.2 cm, 0.8 cm, 2.2 cm, 2.8 cm, and 3.0 cm). (b) Transferred charge density between double offset copper rings in the SC condition when s changes (*s* = 0.5 cm, 2.5 cm, and 3.0 cm). (c) Structure of charged sphere passing through double copper rings and relevant parameters. The variables in the structure are defined as follows: r_s represents the radius of the charged dielectric sphere, r_c represents the radius of both copper rings, *d* represents the displacement of the sphere, *h* represents the vertical height between the double copper rings, S_0 represents the minimum horizontal distance between the double copper rings, and *S* represents the horizontal distance between the center of the double copper rings. (d) three-Dimensional distribution of electric potential (colors) and electric field (arrows) when the charged sphere passes through the offset vertical copper rings horizontal offset of 0.5 cm. (e) Distribution of electric potential in the OC conditions when s changes (*s* = 0.5 cm, 2.5 cm, and 3.0 cm).

Figure 6.7. Electric potentials of both copper rings in the OC condition in the

crossed double copper rings model, with varying horizontal distance s between the double copper rings.

Figure 6.8. Electric potentials of both copper rings in the OC condition in the horizontal double copper ring model, where the minimum distance S_0 between double copper rings varied from 0.5 cm to 10 cm.

Figure 6.9. Simulation results of charged sphere passing through horizontal double copper rings (ρ_s = 10 μC/m^2, r_s = 0.5 cm, the radii of the double horizontal copper rings are the same, r_c = 1.5 cm). (a) Electric potential difference between double horizontal copper rings when the closest distance between the double horizontal copper rings S_0 changes (S_0 = 0.5 cm, 1 cm, 2 cm, 3 cm, 5 cm, and 10 cm). (b) Electric potential and (c) surface charge density of both horizontal copper rings under OC conditions when S_0 = 0.5 cm. (d) Surface charge density comparison when the horizontal double copper rings are under OC and SC conditions. (e) Distribution of electric potential (colors) and electric field (arrows) when the charged sphere passes through the double horizontal copper rings. (f) Contours of the electric potential (V) under OC conditions when the distance between the double horizontal copper rings S_0 changes (S_0 = 0.5 cm, 2 cm, and 5 cm).

- **List of Tables**

Table 4.1 Parameters utilized in the numerical calculation.

Table 6.1 Parameters utilized in the numerical calculations for the single-copper-ring mode TENG.

Table 6.2 Parameters utilized in the numerical calculations for the vertical double-copper-ring mode TENG.

Table 6.3 Parameters utilized in the numerical calculations for the horizontal double-copper-ring mode TENG.

Chapter 1. Introduction

1.1 General background of triboelectric nanogenerator

1.1.1 Unraveling TENG's Origins

The triboelectric effect is a common phenomenon we encounter daily. It happens when two distinct materials touch, often leading to what many industries view as a problematic outcome. This is because the static charges from this effect can cause issues like ignitions, dust explosions, and electronic damage, to name a few. Historically, these charges were seen primarily as potential hazards. However, from an energy perspective, they can be viewed as a form of stored capacitive energy. Early inventors recognized this potential, giving rise to classic devices like the friction machine and the Van de Graaff generator[1]. While triboelectrification's main applications had been limited to processes like air filtering and photocopying, its potential was vastly underutilized.

This limited view began to change in 2012 when Wang's group introduced the triboelectric nanogenerators (TENGs) (**Figure 1.1**), redefining our perception of triboelectrification from mere "electrostatic charging" to a promising means of "electricity generation". This innovative approach opened new horizons for energy harvesting and creating self-powered devices[2]. The brilliance of TENGs lies in their ability to harness the triboelectric effect and combine it with electrostatic induction. So, while the triboelectric effect places static charges on materials that touch, electrostatic induction uses these charges to convert mechanical energy into electricity, capitalizing on the principles of Maxwell's displacement current.

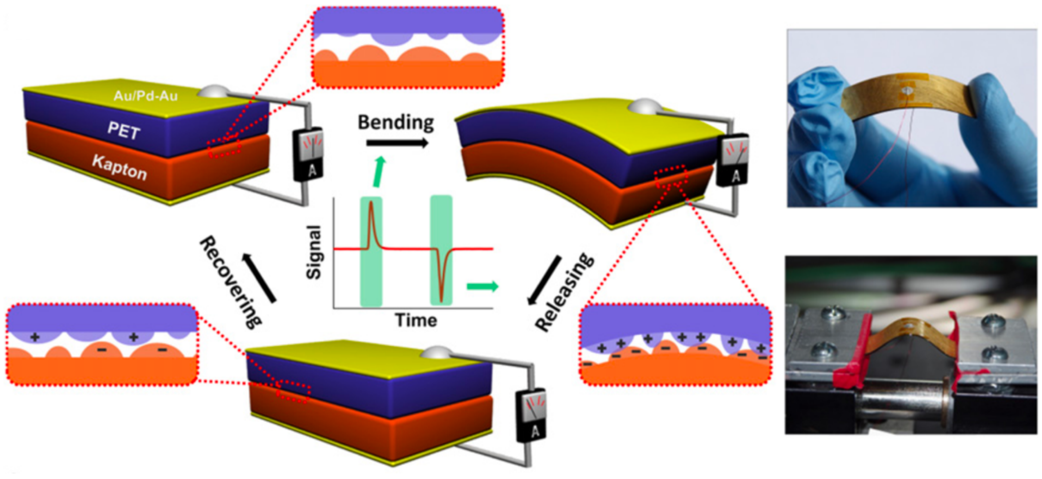

Figure 1.1. Schematic illustration of the first TENG and its operation cycle.[2]

To charge dielectric polymers, such as those used in dielectric balls, one typically employs a process called triboelectric charging, which is contact electrification (CE) in the thesis. This involves rubbing or contacting two different materials, causing an exchange of electrons between them. The resulting imbalance of charges leads to one material becoming negatively charged while the other becomes positively charged. For example, if a dielectric polymer is rubbed with a material that has a higher electron affinity, the polymer may lose electrons and become positively charged. Conversely, if it is rubbed with a material that has a lower electron affinity, the polymer may gain electrons and become negatively charged. Materials with high dielectric constants and low conductivity can help maintain charge stability. Materials with these properties such as PTFE and Kapton can effectively store charge for longer periods of time.

1.1.2 Basic working Modes of TENG

Contact-Separation Mode

The contact-separation mode of TENG operates on a simple principle involving two dielectric materials with different tendencies to attract electrons. At least one of these materials is an insulator, as depicted in **Figure 1.2a**[3]. When these two materials come into contact, they generate opposing static charges on their surfaces due to their unique electron affinities. As the materials separate, this touching and parting create a voltage difference between the electrodes found on their outer layers. When these electrodes are connected with an external device, the electrical difference pushes electrons from one electrode to flow towards the other, trying to neutralize the imbalance. However, when the materials contact again, this voltage difference disappears, causing the previously moved electrons to return to their original position. In essence, by repeatedly touching and then separating the two materials, electrons are made to oscillate between the electrodes. This consistent movement produces an alternating current (AC) in any connected external circuit.

Lateral-Sliding Mode

In the lateral-sliding mode of TENG, the focus is on the relative sliding of two dielectric materials against each other, as illustrated in **Figure 1.2b**[3]. When these materials—each possessing unique triboelectric properties—make contact, a consequential surface charge transfer arises, attributable to the Contact Electrification (CE) effect. In situations where the contacting surfaces are perfectly aligned, the electrical landscape remains static. This stasis is due to the comprehensive balance between the positive charges on one material and the negative charges on the other, ensuring no current is initiated. However, when an external force instigates a relative shift parallel to their interfacing boundary, this electrostatic equilibrium is perturbed. The ensuing misalignment means that the triboelectric charges no longer counterbalance. This imbalance then forges an effective dipole polarization, aligning itself with the displacement's direction. As a direct result, a discernible potential difference emerges across the paired electrodes.

Single-Electrode Mode

The single-electrode configuration of TENGs is especially adept at monitoring the motion of unanchored objects. In the context of a coupled dielectric and metal plate configuration, as shown in **Fig. 1.2c**[3], the proximity of a charged dielectric instigates an induction current within the metal plate, a response to equilibrate the electrostatic environment. As the dielectric recedes from this metal plate, the induced current reroutes itself to the ground. This mode finds its primary utility in harnessing energy from autonomously moving entities without necessitating direct wired connections. Typical applications encompass human ambulation, vehicular motion, keystrokes, among other dynamic activities.

Free-Standing Mode

The free-standing mode is ingeniously devised to mitigate frictional forces between paired dielectrics (as referenced in **Fig. 1.2d** [3]. When a set of congruent, symmetrically-positioned electrodes is situated beneath a dielectric layer—maintaining dimensions commensurate with the mobile object and ensuring a minute separation between the object and electrode—an intriguing dynamic ensues. If the moving object, having been pre-charged via a triboelectric mechanism, draws near or retreats from these electrodes, it induces an asymmetric charge distribution within the intermediary medium. This asymmetry prompts electron movement between the paired electrodes, aiming to restore local potential equilibrium. Resultantly, the rhythmic oscillations of the electrons in response to the object's oscillatory motion yield an AC current output. Noteworthy is this mode's dual capability: it not only capitalizes on the energy from mobile objects but also maintains the system's portability, obviating the need for grounding.

Rolling Mode

The rolling mode, as depicted in **Fig. 1.2e**, represents a synthesis of the four previously described modes[4; 5]. Its primary mechanism leverages the rolling contact electrification (CE) that transpires between spheres and a solid substrate. Thoughtful electrode design beneath this substrate can lead to the generation of power, attributed to the disrupted charge equilibrium instigated by the rolling spheres. A salient advantage of this mode is its capacity to substantially diminish material wear during triboelectrification, all while preserving a robust output.

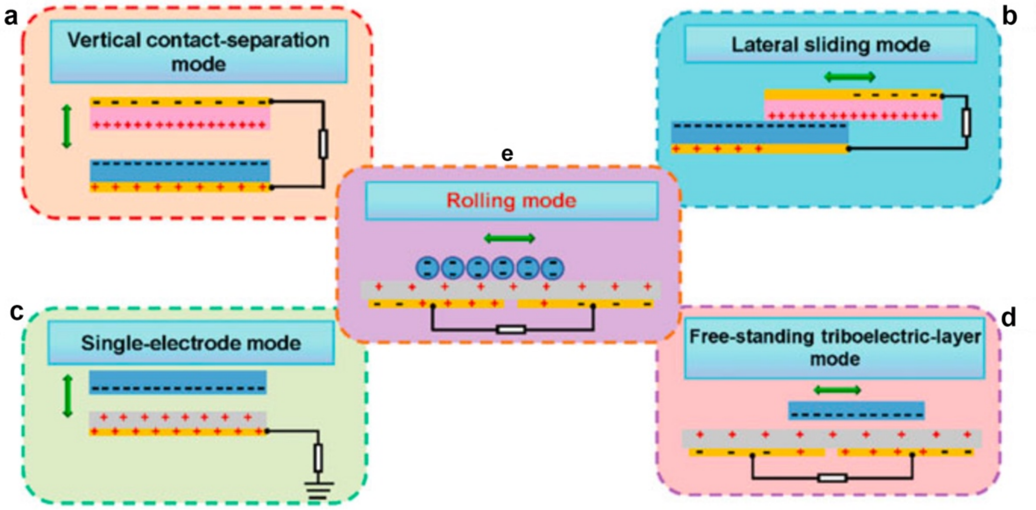

Figure 1.2. Coordination system and mathematical parameters defined for describing (a) contact-separation, (b) lateral-sliding mode, (c) single-electrode mode, (d) free-standing mode, and (e) rolling mode TENGs, respectively.

1.2 Electric Double Layer Model and Solid-liquid TENG

1.2.1 Traditional Electric Double Layer Model

The Electric Double Layer (EDL) model stands as a cornerstone in electrochemistry, shedding light on the intricate dynamics of charge and potential distribution at the liquid-solid juncture. The roots of this model trace back to Helmholtz's 1853 study[6], where he posited the existence of two juxtaposed layers of counter charges at the electrode/electrolyte boundary. While Helmholtz's contribution marked a pivotal point, the model wasn't exempt from scrutiny. The year 1913 saw Gouy and Chapman[7] presenting an enhancement; they proposed that ions, rather than being firmly anchored to the solid boundary, spread across a thin neighboring layer.

The EDL's understanding underwent a transformation in 1924 when Stern merged the insights from Helmholtz's foundational model with the adjustments posited by Gouy and Chapman[8]. This integrated framework underscored two distinct charge regions: the Stern Layer (SL) and the Diffuse Layer (DL). The SL is distinguished by its ions, frequently in a hydrated form, adhering tightly to the electrode with their charge. Conversely, the DL is characterized by a concentration gradient of ions, wherein ions antipodal to the electrode's charge diminish in presence as the distance from the electrode surface increases.

Fig. 1.3 visually presents the combined Gouy–Chapman–Stern (GCS) EDL model, a construct that has notably influenced research domains such as electrolyte capacitors, electrowetting, and electrochemical reactions. Central to this model is the external field's role in EDL formation, particularly discernible in pre-charged insulators and electrodes subjected to an external field. It holds particular relevance for materials with specialized chemical constituents, for instance, carbon derivatives enriched with carboxylic groups (-COOH) that inherently magnetize ions. Its wide applicability spans not only traditional areas like corrosion prevention and energy storage but also extends to interdisciplinary fields, including biomedical engineering.

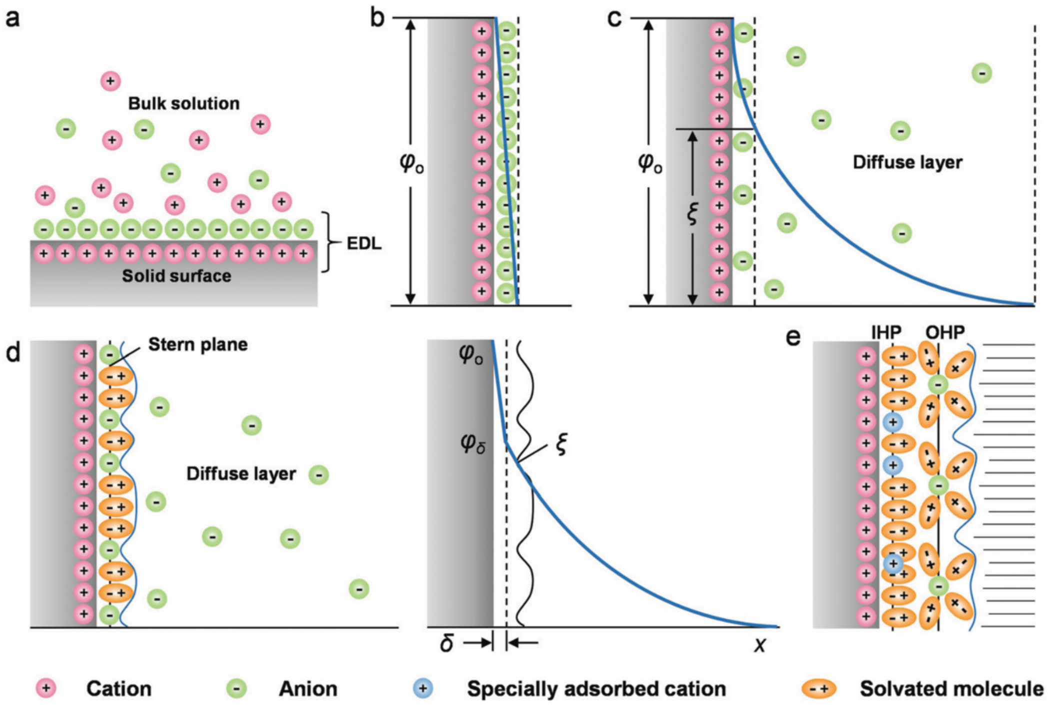

Figure 1.3. Typical models of an EDL. (a) Schematic of an EDL in a liquid in contact with a positively-charged solid. If the solid is negatively-charged, the charge distribution will be the inverse. Schematic of the (b) Helmholtz plate EDL model, (c) Gouy–Chapman diffuse EDL model, (d) Stern EDL model, and (e) BDM EDL model.

1.2.2 EDL model for solid-liquid triboelectric nanogenerator

The hybrid EDL model, known as Wang's hybrid layer, introduced by Wang et al.[9], sheds new light on solid-liquid interface dynamics in Triboelectric Nanogenerators. Instead of solely attributing the charge exchange process to ion adsorption, this model's foundation rests on a “two step” mechanism and emphasizes the significant role of electron transfer. Initially, due to thermal motion and liquid pressures, liquid molecules interact with the solid surface, facilitating electron transfer. This is particularly prominent in fluorine-rich materials. Once this electron movement occurs, free ions in the liquid are attracted to the electrified surface, forming an EDL, resembling traditional models. However, simultaneous ionization reactions occur, producing both electrons and ions. A notable product of this process is the H_2O^+ cation, which quickly transforms into OH and H_3O^+ radicals[10; 11].

Key insights from the hybrid EDL model include the intertwined nature of ionization reactions and electron transfers in affecting potential distribution. This is evident in specific cases like the CE between SiO_2-water and PTFE-water[12; 13]. Furthermore, the model reveals nuances in electron trapping at surface states and the pivotal role of electron transferrin solid-liquid CE. Beyond elucidating charge distributions, the model emphasizes the intricate behavior of electrons, whether sequestered in surface states or engaged in essential transfers, which subsequently dictate the solid-liquid interactions in Nanogenerators.

1.3 Purpose of this Work

This research delves into the intricacies of the solid-liquid TENG, an area progressively attracting attention across multidisciplinary research fields. Recognizing a gap in the literature concerning the mechanisms of the solid-liquid triboelectric nanogenerators, this thesis aspires to bridge this void.

The initial chapters establish a foundational understanding of TENG and its research trajectory, followed by an extensive literature review in Chapter 2, which examines the characteristics of solid interfaces, the underlying physical concepts, and their prospective applications. Subsequent chapters are methodologically oriented, with Chapter 3 detailing the experimental framework, Chapter 4 analyzing the electrical performance of the water-solid mode TENG, Chapter 5 investigating the output performance of copper ring based non-contact TENG and Chapter 6 extending insights through simulation studies. The research concludes in Chapter 7, offering integrated perspectives and highlighting potential future research directions, thereby emphasizing the overarching relevance and contribution of this study in the TENG landscape.

1.4 Structure of the Thesis

This thesis is organized into seven distinct chapters, the details of which are outlined below:

Chapter 1 provides an introduction to the general background of TENG, emphasizing the foundational theory of solid-liquid TENG. It further delves into the prevailing research interests concerning this topic.

Chapter 2 offers an exhaustive literature review on the triboelectricity at the solid-liquid interface. This chapter focuses on variations in the solid interface and the underlying physical principles, as well as potential applications of solid-liquid TENG.

Chapter 3 delineates the experimental methodologies, encompassing the fabrication process, instruments used, and the simulation software and procedures employed.

Chapter 4 discusses the electrification performance and mechanisms of the water-solid mode TENG. The work in chapter 4 is published on *ACS nano*, DOI: 10.1021/acsnano.1c00795.

Chapter 5 developed a copper ring based TENG, generating power based on electrostatic induction only.

Chapter 6 evaluates simulation outcomes related to electrical characteristics under varied circuit conditions for three representative non-contact TENG models. The work in chapter 5 and chapter 6 is published on *EcoMat*, DOI: 10.1002/eom2.12392.

Chapter 7 culminates the thesis with a summary of the primary conclusions drawn from my PhD research. It further posits potential future avenues and applications of solid-liquid TENG in interdisciplinary studies.

Chapter 2. Literature Review

2.1 Introduction

TENGs have emerged as a promising technology for energy harvesting[14-19], converting mechanical energy into electrical energy through the triboelectric effect and electrostatic induction. The triboelectric effect refers to the phenomenon of charge transfer that occurs when two dissimilar materials come into contact and separate. This effect has been extensively studied in solid-solid interfaces, where materials with different electron affinities and work functions interact to generate static electricity. However, the exploration of the triboelectric effect at the solid-liquid interface, where one of the materials is in a liquid state, has gained significant attention in recent years. The concept of solid-liquid interface triboelectricity brings about new opportunities and challenges. Liquid-solid TENGs offer unique advantages over their solid-solid counterparts, such as flexibility, adaptability, and the ability to harvest energy from various liquid-based environments. These characteristics make them particularly suitable for applications in fields such as biomechanics, environmental monitoring, wearable devices, and human-machine interfaces. Furthermore, the abundance and diverse properties of liquids provide a rich platform for exploring novel materials and engineering designs to enhance the performance and efficiency of TENGs.

This review section focuses on the fundaments and applications of solid-liquid interface triboelectricity, aiming to provide a comprehensive understanding of the field and highlight its potential for various technological advancements. We begin by defining the concept of solid-liquid interface triboelectricity and discussing its historical development. We delve into the motivations behind exploring liquid-solid TENGs, including the need for sustainable energy harvesting, the advantages of liquid-based environments, and the unique challenges associated with this interface. The subsequent sections of this literature review delve into the fundamental working modes of liquid−solid TENGs, exploring three key modes: liquid-dielectric, liquid-semiconductor, and liquid-metal. Each mode has distinct properties and mechanisms, which we will discuss in detail, drawing upon relevant studies and experimental findings. We will explore the physical fundament of liquid−solid TENGs, including the "Wang Transition" for Contact Electrification (CE) and Wang's Hybrid Electric Double Layer (EDL) model, as well as the mechanisms of liquid−solid CE based on density functional theory. Understanding the charge transfer and charge states at the liquid-solid interface is crucial for comprehending the underlying mechanisms of liquid−solid TENGs. Therefore, we will delve into the theoretical and experimental investigations of charge states at the interface and discuss their implications for device performance and energy harvesting efficiency. Furthermore, this review section will explore the broad range of applications enabled by liquid−solid TENGs. We will discuss their role as micro/nano-power sources, providing sustainable energy for various devices and systems. Additionally, we will examine their utility as self-powered sensors, enabling autonomous and continuous monitoring in diverse applications. Furthermore, we will explore the integration of liquid−solid TENGs into scanning probe systems, offering enhanced imaging capabilities and nanoscale manipulation. Finally, we will discuss other emerging applications, such as blue energy harvesting, water and wastewater treatment and the electrowetting technique.

In conclusion, literature section aims to provide a comprehensive overview of the emerging field of solid-liquid interface triboelectricity. By exploring the fundamental working modes, physical fundament, charge transfer mechanisms, and applications of liquid−solid TENGs, we aim to foster a deeper understanding of the underlying principles and potential applications of this technology. Through a comprehensive examination of the literature and key research findings, we strive to shed light on the advancements made in the field and highlight the challenges and opportunities that lie ahead. It is our hope that the literature review section will serve as a valuable resource for researchers, engineers, and professionals interested in the field of solid-liquid interface triboelectricity. By providing a detailed exploration of the fundamental concepts, mechanisms, and applications, we aim to inspire further research and innovation in this rapidly evolving area.

2.2. Three fundamental working modes of the Liquid−Solid TENG

2.2.1 Liquid-dielectric mode

The liquid-dielectric mode is one of the fundamental working modes in the realm of solid-liquid interface triboelectric nanogenerators (TENGs). In this mode, the interface between a liquid and a dielectric material is utilized to induce triboelectric charging and subsequent energy harvesting. The liquid employed in this mode serves as the medium for charge transfer and ion adsorption. The working principle of the liquid-dielectric mode can be understood as follows: When a dielectric material comes into contact with a liquid, a charge transfer occurs due to the difference in electron affinity and electronegativity between the two materials. The contact electrification process leads to the redistribution of charges, resulting in the generation of a voltage potential across the interface. Upon separation, the accumulated charges are further separated, creating an electrical potential difference that can be harvested as electrical energy[20-24].

Numerous studies have explored the liquid-dielectric mode and demonstrated its potential for efficient energy conversion. Various liquids have been investigated, including water, organic solvents, and electrolytes. For example, You et al. [25] reported the use of water as the liquid medium in a liquid-dielectric TENG, where multidielectric layer constructed from polyimide (Kapton) tape and polytetrafluoroethylene (PTFE) films served as the dielectric material (**Figures 2.1a, 2.1b and 2.1c**). They developed an equivalent circuit model and governing equations for the water−solid mode TENG, which can be extended to other types of liquid−solid TENGs. Their model, based on the first-order lumped circuit theory, represents the water−solid TENG as a series connection of two electric double layer capacitors and a water resistor. By examining the output characteristics and critical influences of the model, they provided insights into the relevant physical mechanisms underlying the operation of the water−solid mode TENG. Similarly, Zhao et al. [26] introduced a self-powered, long-lasting, and highly selective oil–solid triboelectric nanogenerator (O-TENG) for energy harvesting and intelligent monitoring (**Figures 2.1d and 2.1e**). The O-TENG exhibited excellent electrical output, outperforming O-TENGs made from commercial dielectric materials. The O-TENG-based sensor exhibited exceptional sensitivity and remarkable durability, present a promising approach for enhancing the output and durability of O-TENGs in oil–solid contact, while also enabling intelligent energy harvesting and oil condition monitoring. Nie et al. [27] conducted a comprehensive investigation to elucidate the mechanism of contact electrification between a liquid triboelectric layer and a solid material (**Figure 2.1f**). Their study focused on the triboelectrification process between PTFE and various solvents, including water, NaCl, and CuSO4. The findings revealed that the charge transfer between water and PTFE primarily involved electron transfer, while ion transfer played a dominant role in the charge transfer between ionic liquids (e.g., NaCl) and PTFE. The concentration of ions in the solution played a crucial role in the amount of transferred charges. Initially, as the ion concentration increased, the transferred charges also increased. However, after reaching a peak, the transferred charges gradually decreased and eventually reached zero. This behavior was attributed to the accumulation of ions at the solid-liquid interface, leading to a decrease in the electron transfer process due to the screening effect. Notably, irrespective of the type of ion, the amount of charge generation between the ionic liquids and PTFE exhibited a similar pattern. In the cases of NaCl and CuSO4, the maximum charge transfer occurred at an ion concentration of 1×10^{-5} mol L^{-1} upon contact with the PTFE surface. These findings provide valuable insights into the charge transfer mechanisms between liquid triboelectric layers and solid materials, shedding light on the intricate interplay between electron and ion transfers in contact electrification phenomena.

Notably, Shiquan Lin et al. [28] conducted a study focused on quantifying electron transfer in liquid-solid contact electrification and investigating the formation of the electric double-layer (**Figure 2.1g**). In their investigation, Lin et al. examined the contact electrification between liquids and solids and studied the decay of charge on solid surfaces after liquid-solid contact under different thermal conditions. To differentiate the contribution of electron transfer from that of ion transfer on the charged surfaces, they applied the theory of electron thermionic emission. Their comprehensive study revealed the presence of both electron transfer and ion transfer in liquid-solid contact electrification. Building upon these findings, the researchers proposed a two-step model that encompasses electron and/or ion transfer, and they successfully demonstrated the formation of an electric double-layer in the process of liquid-solid contact electrification.

Furthermore, Haiyang Zou et al. [29] made significant contributions to the understanding of the triboelectric series, which is essential for characterizing charge transfer between liquid and solid materials (**Figure 2.1h**). By introducing a universal method to quantify the triboelectric series for various polymers, they established a fundamental materials property for quantitative triboelectrification. Through experiments involving the measurement of materials with a liquid metal under well-defined conditions, their method standardized the evaluation of surface triboelectrification. They derived a normalized triboelectric charge density, which revealed the intrinsic character of polymers in terms of gaining or losing electrons. This quantitative triboelectric series serves as a textbook standard, facilitating the application of triboelectrification for energy harvesting and self-powered sensing purposes. The research by Haiyang Zou et al. clarifies the charge polarity and magnitude in liquid-solid interactions, contributing to the design and optimization of liquid-dielectric TENGs.

Moreover, to enhance the performance of the liquid-dielectric mode in solid-liquid interface triboelectric nanogenerators (TENGs), researchers have explored various design configurations. These include the use of structured surfaces such as micro/nanostructured patterns or porous materials, which effectively increase the contact area and facilitate more efficient charge transfer. Additionally, the introduction of functional coatings or surface modifications on the dielectric material has been investigated to alter its surface properties and enhance the triboelectric charging process.

These studies, among others, collectively contribute to the growing body of knowledge in the field of liquid-dielectric TENGs. By elucidating the underlying mechanisms and providing insights into performance enhancement, they pave the way for practical applications of these devices. In summary, the liquid-dielectric mode of solid-liquid interface TENGs offers a promising avenue for energy harvesting. By leveraging the interface between a liquid and a dielectric material, charge transfer and separation can be achieved, leading to the generation of electrical energy. Through careful selection of liquid and dielectric materials, as well as design optimization, the performance of liquid-dielectric TENGs can be significantly improved, enabling their application in micro/nano-power sources, self-powered sensors, and other emerging fields.

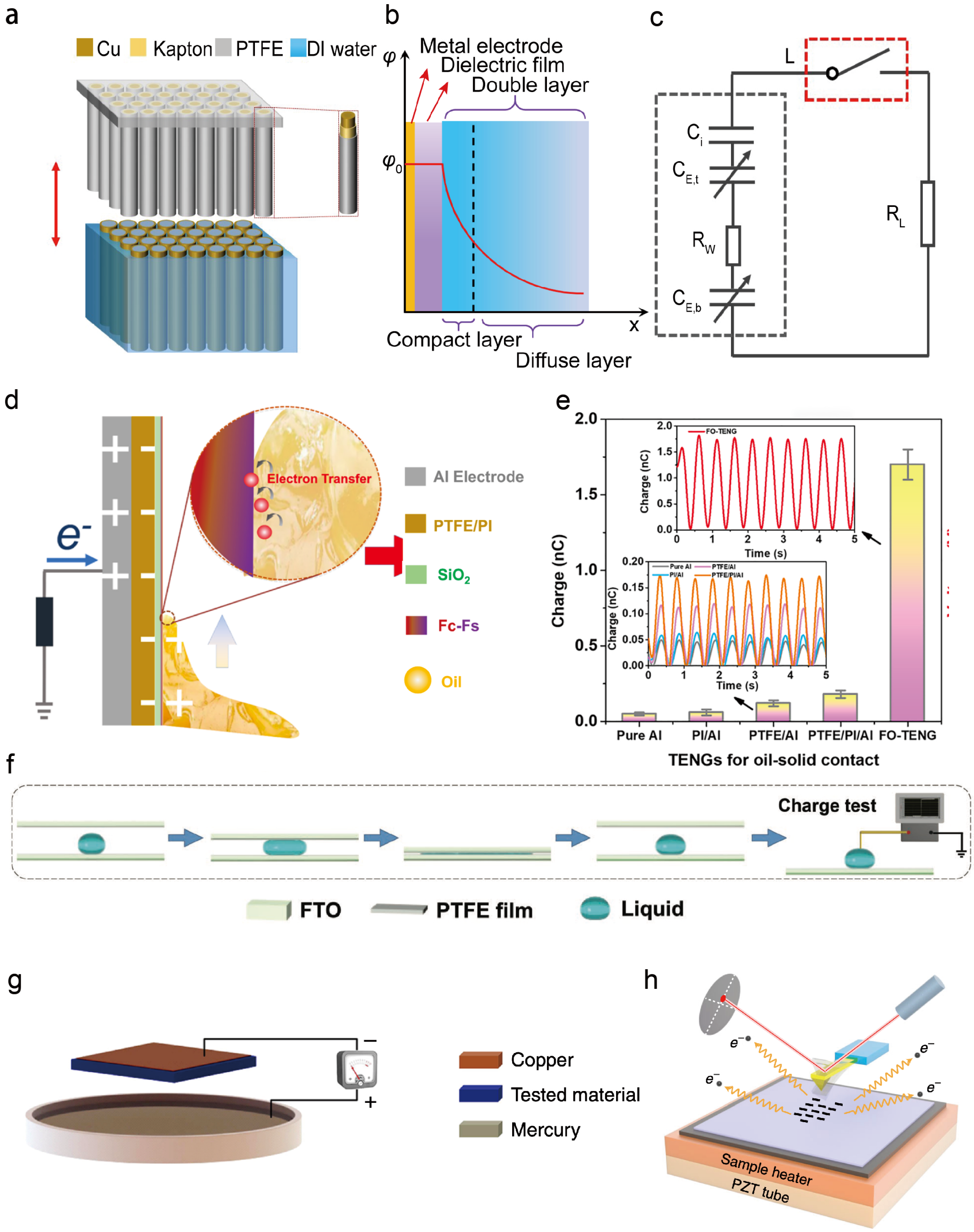

Figure 2.1. Typical liquid-dielectric mode TENG. (a) Schematic diagram of the three-dimensional water–solid TENG array, (b) Typical electrical double layer formed on the water–dielectric interface area and the relevant variation of electrostatic potential *φ* with distance *x* from the electrode and (c) The full equivalent circuit model of the water–solid triboelectric nanogenerator. (d) Schematic illustration on the triboelectric mechanism of the FO-TENG (The O-

TENG modified with different amounts of Fc(x) and Fs(y) is noted as FO-TENG(x–y)) and (e) transferred charge curves of the FO-TENG compared with other O-TENGs for oil-solid contact. (f) Method for testing the amount of charge on water droplet after L-S friction. (g) Simplified model of the measurement method. The tested material contacts the liquid metal of mercury, and then separates periodically. The positive electrode of the electric meter is connected to the mercury, and the negative is connected to the copper electrode. (h) The setup of AFM platform for the thermionic emission experiments.

2.2.2 Liquid-Semiconductor mode

The liquid-semiconductor mode is another fundamental working mode in the realm of solid-liquid interface triboelectric nanogenerators (TENGs). In this mode, the interface between a liquid and a semiconductor material is utilized to induce triboelectric charging and subsequent energy harvesting. The presence of a semiconductor in contact with the liquid enables the generation and separation of charges through the tribovoltaic effect. The working principle of the liquid-semiconductor mode can be understood as follows: When a semiconductor material comes into contact with a liquid, the contact electrification process induces the transfer of electrons between the two materials. This electron transfer generates a voltage potential at the liquid-semiconductor interface. Subsequent charge separation occurs upon separation of the materials, resulting in the formation of an electrical potential difference that can be utilized for energy harvesting.

Several studies have explored the liquid-semiconductor mode and demonstrated its potential for efficient energy conversion[30-32]. For instance, Shiquan Lin et al. [33] designed experiments to investigate the tribovoltaic effect at aqueous solution and silicon interface, in which a syringe conductive needle was used to drag a DI water droplet to slide over a silicon wafer surface (**Figure 2.2a**), and the tribo-current and tribo-voltage were recorded (**Figures 2.2b and 2.2d**). It was found that a DC tribo-current can be generated during the sliding, as shown in **Fig. 2.2d**. The direction of the tribo-current was from p-type silicon to the aqueous solution or from aqueous solution to the n-type silicon in the external circuit, implying that the electrons moved from p-type silicon side to the aqueous solution side or from n-type silicon side to the aqueous solution side at the interface. Combining I-V characterizations, the direction of the tribo-current at the sliding aqueous solution-silicon interface was found to be the same with the direction of the built-in electric field at the interface, which was consistent with the tribovoltaic effect.

In the realm of tribovoltaic effect research, the impact of temperature on liquid-solid interfaces has been investigated by Mingli Zheng et al. [34]. Their study delved into the relationship between temperature and the tribo-voltage and tribo-current at interfaces such as water/Si and water/metal during sliding (**Figure 2.2e**). The findings unveiled a direct correlation, indicating that increasing the temperature resulted in higher tribo-voltage and tribo-current outputs (**Figure 2.2f**). Furthermore, the researchers demonstrated the synergistic effect of the liquid's pH value and temperature on the tribovoltaic effect. To explain the observed data, an energy band model was proposed (**Figure 2.2c**), highlighting the role of "bindington" energy—energy released through the formation of chemical bonds between the liquid and solid—in driving the generation of the tribovoltaic effect. These significant findings shed light on the intricate interplay between temperature, pH value, and the tribovoltaic effect at liquid-solid interfaces, contributing to the advancement of energy harvesting technologies in this domain.

These studies, among others, have contributed to advancing the understanding of the liquid-semiconductor mode and its applications in energy harvesting. By leveraging the unique properties of semiconductors in conjunction with liquid materials, charge transfer and separation can be achieved, enabling the conversion of mechanical energy into electrical energy.

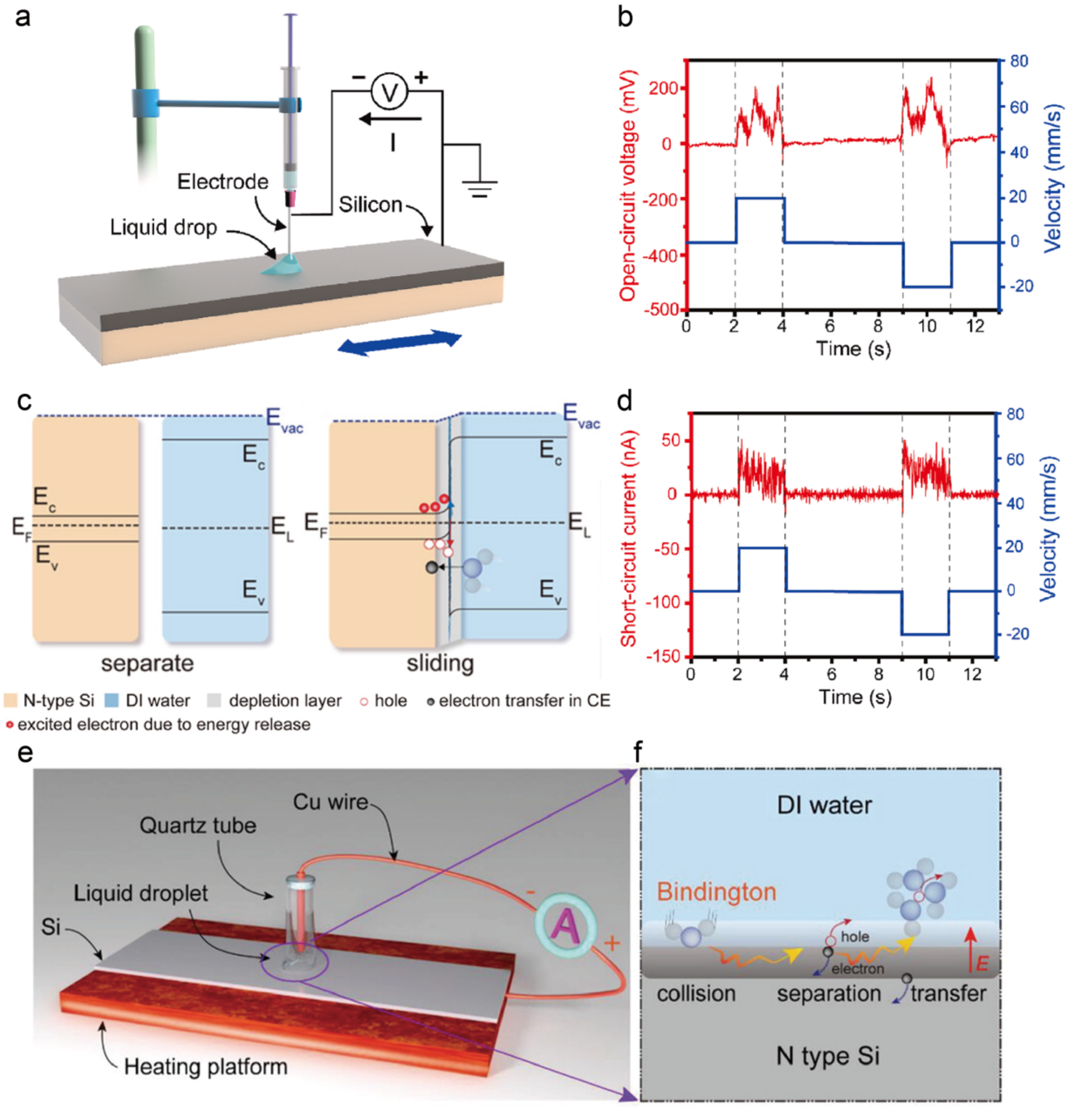

Figure 2.2. Typical liquid-semiconductor mode TENG. (a) The setup of the tribovoltaic experiments and the external circuit, (b) the oscillogram of open-circuit voltage when a DI water droplet slides on the P-type silicon wafer (0.1 Ω cm) at 20

mm/s, and the droplet static contact diameter is 2.5 mm, (d) the oscillogram of short-circuit current when a DI water droplet slides over the P- type silicon wafer (0.1 Ω cm) at 20 mm/s, and the droplet static contact diameter is 2.5 mm. (c) Energy band diagram of the N-type Si and the DI water, (e) the setup of the experiments and (f) a schematic diagram of the generation of tribo-current.

2.2.3 Liquid−Metal mode

The liquid-metal mode is a significant working mode in the realm of solid-liquid interface triboelectric nanogenerators (TENGs). In this mode, the interface between a liquid and a metal material is utilized to induce triboelectric charging and subsequent energy harvesting. The presence of a metal in contact with the liquid enables efficient charge transfer and separation through various mechanisms.

The working principle of the liquid-metal mode can be understood as follows: When a metal material comes into contact with a liquid, the contact electrification process induces charge transfer between the two materials. This charge transfer occurs due to the difference in work functions and electron affinities between the metal and the liquid. The redistribution of charges at the liquid-metal interface leads to the generation of a voltage potential that can be harvested as electrical energy.

Several studies have explored the liquid-metal mode and demonstrated its potential for efficient energy conversion. For instance, Jiabo Le et al. [35] provided theoretical insights into the vibrational spectra of metal-water interfaces using density functional theory-based molecular dynamics (**Figure 2.3a**). Although their study focused on the vibrational properties, it contributed to the understanding of the interface behavior between metals and liquids, which is crucial for elucidating the charge transfer mechanisms and optimizing the performance of liquid-metal mode TENGs.

In addition, another study by Jun Zhao et al. [36] presented a direct-current fluid-flow-based TENG (DC-FluTENG) for mechanical-to-electrical energy conversion from flowing water (**Figure 2.3b**). The falling of a water droplet from a pipe was demonstrated to generate direct current in the external circuit by contacting a separated electrode. The device exhibited distinct characteristics of pulsed direct current, enabling it to directly drive electronic devices without requiring a rectifier (**Figure 2.3c**). The experimental results showed an open-circuit voltage of 35 V, a short-circuit current of 3.7 μA, and a peak power of 57.6 μW. The DC outputs of the device allowed for improved portability and energy utilization efficiency, with the ability to directly power commercial temperature and humidity IoT sensors. The study also investigated factors such as water droplet type, flow rate, and electrode material, which affected the output performance of the direct-current fluid-flow-based TENG.

The liquid-metal mode offers unique advantages due to the excellent electrical conductivity of metals. This enables efficient charge transfer and low-resistance pathways for current flow, leading to improved energy harvesting capabilities. Additionally, the selection of appropriate metal materials and the optimization of their surface properties can further enhance the performance of liquid-metal TENGs.

It is worth noting that the liquid-metal mode can be explored with different liquid media, such as water, organic solvents, or electrolytes, depending on the specific application requirements. The choice of the liquid influences the charge transfer mechanisms and the overall performance of the TENG system.

In summary, the liquid-metal mode of solid-liquid interface TENGs offers a promising approach for energy harvesting. By utilizing the interface between a liquid and a metal material, efficient charge transfer and separation can be achieved, enabling the conversion of mechanical energy into electrical energy. Further research and optimization in this mode will contribute to the development of practical applications in micro/nano-power sources, self-powered sensors, and other emerging fields.

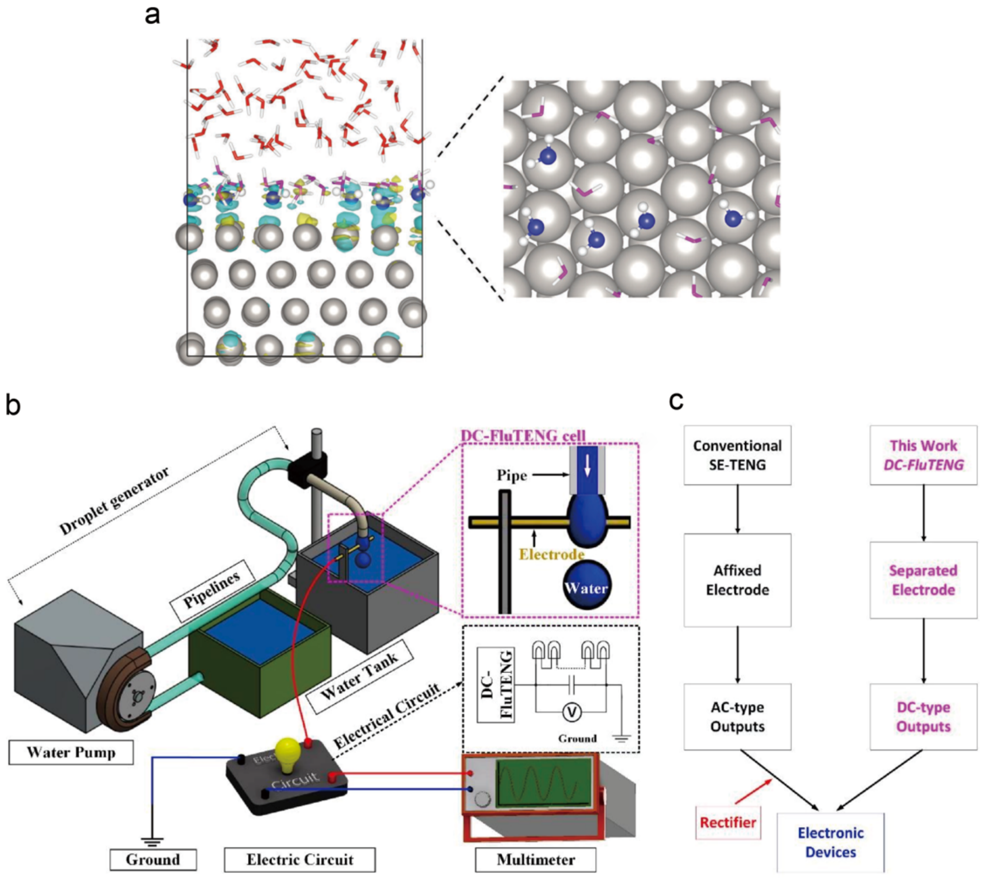

Figure 2.3. Typical liquid-metal mode TENG. (a) Side (left) and top (right) views of a snapshot of the Pt (111)–water interface from a DFTMD trajectory. Pt, watA, watB and watC are colored in grey, blue, magenta and red, respectively. The isosurfaces represent the electron density difference profile of the interface before and after water interacts with the metal surface electronically, and the regions colored in cyan and yellow indicate electron depletion and accumulation, respectively. (b) Schematic showing the experimental setup of DC–FluTENG and

(c) structure diagram of DC–FluTENG in comparison with a conventional single–electrode–based TENG.

2.3 Physical fundament of Liquid−Solid TENG

2.3.1 “Wang Transition” for CE and Wang’s Hybrid EDL Model

Contact electrification at the liquid-solid interface is a complex phenomenon that plays a crucial role in the operation of solid-liquid interface triboelectric nanogenerators. Traditionally, CE has been extensively studied in solid-solid interfaces, where charge transfer occurs between two solid materials upon contact and separation. However, the introduction of liquids into the CE process introduces additional complexities due to the presence of ions and the formation of EDLs. Understanding the underlying processes of CE and the formation of electric double layers is essential for optimizing the performance of liquid-solid TENGs. The "Wang transition" and Wang's hybrid EDL model provide valuable insights into these processes, shedding light on the mechanisms involved at the liquid-solid interface[37-40].

As depicted in **Fig. 2.4** [41], the peak energy level (highest occupied energy level of an atom) occupied by an atom from material A exceeds that of an atom from material B. In the absence of close contact, there's no overlap of the electron clouds of atoms from both materials. Consequently, electrons will not transfer from atom A to B, attributable to the formidable potential barrier between them. The overlap of electron clouds within charge exchange (CE) processes facilitates electron transfer and can be interpreted as the formation of a chemical bond with an extended bond length relative to traditional chemical bonds. Upon the separation of two contacting surfaces, atom A, which has undergone electron loss, is influenced by the surrounding atoms on the material A surface. This interaction leads to the bond between the two atoms (atom A and atom B) extending in length and eventually breaking, and atom A will separate from atom B, resulting in CE.

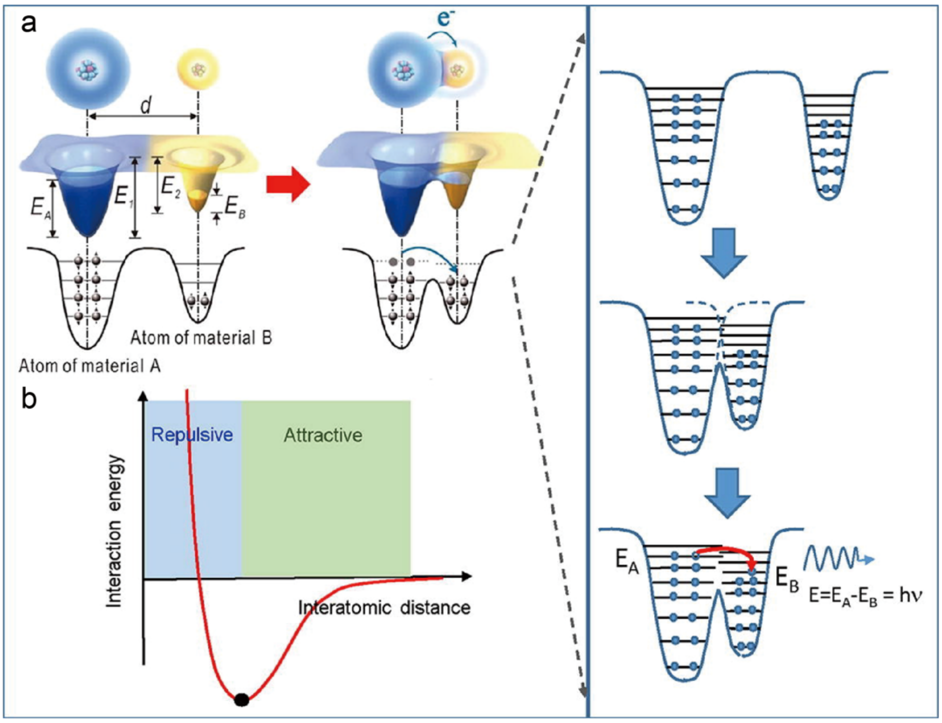

Figure 2.4. (a) An electron-cloud-potential-well model proposed for explaining CE and charge transfer. *d*, distance between two nuclei; E_A and E_B, occupied energy levels of electrons; E_1 and E_2, potential energies for electrons to escape. (b) Interatomic interaction potential between two atoms when they are at equilibrium position.

The electron transfer process is a strong effect that should be considered during the CE between liquid and solid, and thus the electron transfer should not be ignored in the formation of the EDL. Wang's hybrid layer, which is firstly proposed by Wang et al. in 2018 [41], and a "two-step" process for the formation are elaborated with the consideration of both electron transfer and ion adsorption (chemical interaction). Initially, liquid molecules and ions engage the solid surface due to thermal activity and liquid pressure. The overlapping electron clouds between solid atoms and water molecules facilitate electron exchange. Traditional EDL models suggest that the ionized interaction on the liquid-solid interface induces more charges on the surface, which results in the charge distribution and compensation in the diffusion layer. In the hybrid layer, the charge transfer between solid and liquid molecules causes even more charges to be accumulated at the surface. This electron transfer process works parallel with ion adsorption process[40]. Lin et al. [28]studied the CE between liquids and solids and investigated the decay of CE charges on the solid surfaces after liquid-solid CE at different thermal conditions (**Figures 2.5c and 2.5d**). The contribution of electron transfer is distinguished from that of ion transfer on the charged surfaces by using the theory of electron thermionic emission. Their experiments show that there are both electron transfer and ion transfer in the liquid-solid CE. This is the first time that the “two-step” model about the formation of EDL, in which the electron transfer plays a dominant role in liquid-solid CE, is verified experimentally.

These studies, along with others, have significantly advanced our understanding of CE at the liquid-solid interface and the formation of EDLs. The "Wang transition" and Wang's hybrid EDL model serve as critical tools for investigating and comprehending the complex charge transfer mechanisms and the behavior of the EDL in liquid-solid CE.

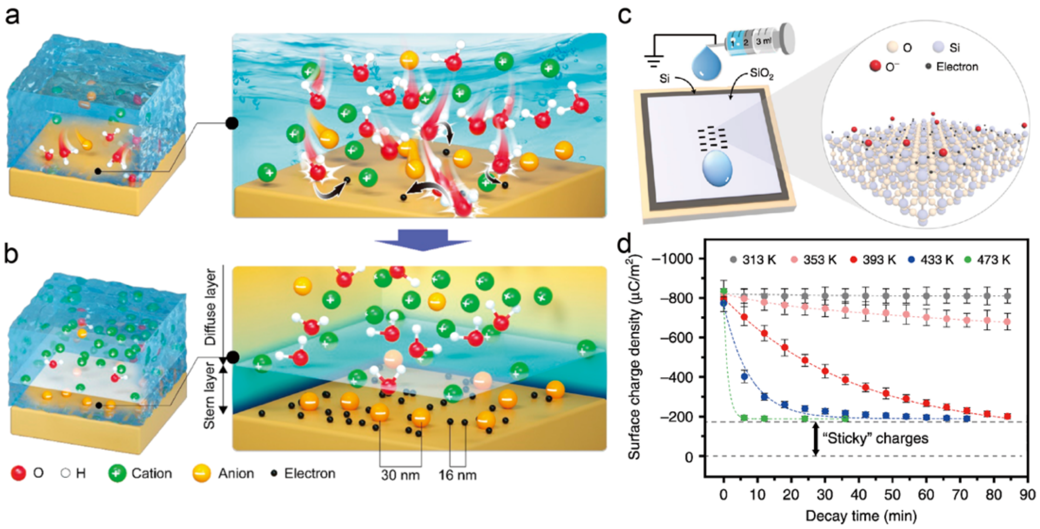

Figure 2.5. (a)-(b) Wang's hybrid EDL model and the "two-step" process on its formation. (a) In the first step, the molecules and ions in the liquid impact the solid surface due to the thermal motion and the pressure from the liquid, which leads to electron transfer between them; meanwhile, ions may also attach to the solid surface. (b) In the second step, free ions in the liquid would be attracted to the electrified surface due to electrostatic interactions, forming an EDL. (c) The setup of the charging experiments, where the negative charges generated on the SiO2 surface could be electrons and O^- ions induced by surface ionization reaction. ('O' is the Oxygen atom, 'Si' is the silicon atom and 'O^-' is the Oxygen ion). (d) The decay of the CE charge (induced by contacting with the DI water at room temperature) on the SiO_2 surface at different substrate temperatures.

2.3.2 Liquid−Solid CE based on Tribovoltaic effect

The tribovoltaic effect, a phenomenon that involves the generation of an electric potential difference upon contact and separation between different materials, has garnered significant attention in the context of liquid−solid contact electrification within the field of triboelectric nanogenerators. This section explores the fundamental principles and mechanisms underlying liquid−solid CE based on the tribovoltaic effect [31; 33; 41-47].

The tribovoltaic effect generates an electric potential through the combination of contact electrification (CE) and the triboelectric effect. When two surfaces with different electronegativities come into contact, the newly formed bond releases energy known as "bindington." The tribovoltaic effect is responsible for CE involving semiconductors, in which electrons are excited at the P-N junction or the Schottky junction during friction. The excited electrons are further driven by the built-in electric field to move from one side to the other side at the interfaces, generating a direct current. The effect is similar to the photovoltaic effect, with the only difference being that the electron-hole pairs in the triboelectric effect are excited by the "bindington" rather than light irradiation. The tribovoltaic effect in liquid−solid CE is governed by various factors, including the materials involved, their surface properties, and the nature of the liquid medium. Researchers have extensively investigated this effect to understand its mechanisms and optimize its performance in TENG applications.

Chi Zhang and Zhong Lin Wang’s group, in their study [45], were the first to demonstrate the presence of the tribovoltaic effect between metal and solid surfaces. They introduced a metal-semiconductor direct-current triboelectric nanogenerator (MSDC-TENG) built on the principle of the tribovoltaic effect (**Figure 2.6a**). This effect is enhanced by the direct voltage and current generated when a metal/semiconductor is rubbed against another semiconductor. The forming atomic bonds release frictional energy, exciting non-equilibrium carriers which, under the influence of the built-in electric field, are separated directionally to form a current. When the metal and silicon are slid against each other, the MSDC-TENG consistently exhibits an open-circuit voltage (10–20 mV) (**Figure 2.6b**), short-circuit direct-current output (10–20 μA) (**Figure 2.6c**), and a low impedance characteristic (0.55–5 kΩ). The researchers conducted a systematic study on these working parameters to understand their effects on electrical output and impedance characteristics. This groundbreaking work not only broadens the scope of material candidates for TENGs to include semiconductors in addition to organic polymers, but also provides a fresh perspective on an electric energy conversion mechanism based on the tribovoltaic effect.

Additionally, a study conducted by Shiquan Lin et al. [33] explored the tribovoltaic effect at liquid-semiconductor interfaces. This research involved generating both tribo-voltage and tribo-current by moving a droplet of DI water across a silicon surface with varied doping types and concentrations. The analysis of voltage-current measurements indicated the presence of a built-in electric field at the interface between the DI water and silicon. The direction of both the tribo-voltage and tribo-current was found to be dependent on this built-in electric field, which suggests that the tribo-voltage and tribo-current were induced by the tribovoltaic effect. Consequently, it can be inferred that the energy released from electron transfer, when the liquid contacts the silicon, stimulates the electron-hole pairs at the silicon surface. Driven by the built-in electric field at the liquid-solid junction, the electron and hole are separated, culminating in the observed tribo-voltage and tribo-current. This study marks a significant milestone in our understanding as it is, the first experimental verification of the tribovoltaic effect at the liquid-solid interface.

Building on this body of research, a study by Mingli Zheng et al. [46] provided microscopic evidence supporting the existence of the tribovoltaic effect. They successfully generated a direct current by sliding an N-type diamond coated tip over Si samples with various doping concentrations (**Figure 2.6d**). The study discovered that the tribo-current between the Si samples escalated in line with an increase in both the density of the surface states of the Si samples and the sliding load. This observation lends credence to the idea that the tribo-current between two semiconductors (or a semiconductor and a metal) is induced by the tribovoltaic effect. The findings suggest that at the interface, the energy released due to the transition of electrons from the surface states of one semiconductor to another, and also from bond formation across the sliding interface, could potentially excite electron-hole pairs. Additionally, the separation of the electron-hole pairs by the built-in electric field at the PN, NN, and Schottky junctions may induce the observed current. To the best of our understanding, this is the first time the tribovoltaic effect has been clearly explained and validated at a microscopic level. These findings also propose a novel method for enhancing the output current in electric generators based on the tribovoltaic effect.

In a groundbreaking study in 2021, Zhong Lin Wang's group [44] formulated the first fundamental physical mechanism of the tribovoltaic effect. This study centred on generating tribo-voltage and tribo-current at the DI water-semiconductor interfaces under light irradiation (**Figure 2.6e)**. The research revealed that the directions of the tribo-current and photo-current were congruent and both dependent on the built-in electric field at the interface between the DI water and semiconductors. Significantly, it was found that light irradiation amplified the tribo-current, with the enhanced tribo-current intensifying proportionately to the light intensity and inversely to the light wavelength. This supports the hypothesis that the tribo-current was instigated by the tribovoltaic effect. In this process, the electron-hole pairs at the interface are excited by the "bindington" and mobilised by the built-in electric field at the heterojunction. Furthermore, the researchers proposed an energy band model (**Figure 2.6f**) to explicate the interaction between the tribovoltaic and photovoltaic effects. In this model, the enhancement of the tribovoltaic current is attributed to the increased concentration of electron-hole pairs under light irradiation.

These studies, among others, highlight the pivotal role of the tribovoltaic effect in liquid−solid contact electrification within the realm of TENGs. By delving into various material combinations and uncovering intrinsic mechanisms, researchers have broadened our comprehension and laid a foundation for enhancing the efficiency of liquid−solid TENGs. Such understanding means that the generation of an electric potential difference during the contact and separation of diverse materials can be harnessed more effectively, leading to promising applications in micro/nano-power sources, self-powered sensors, and beyond.

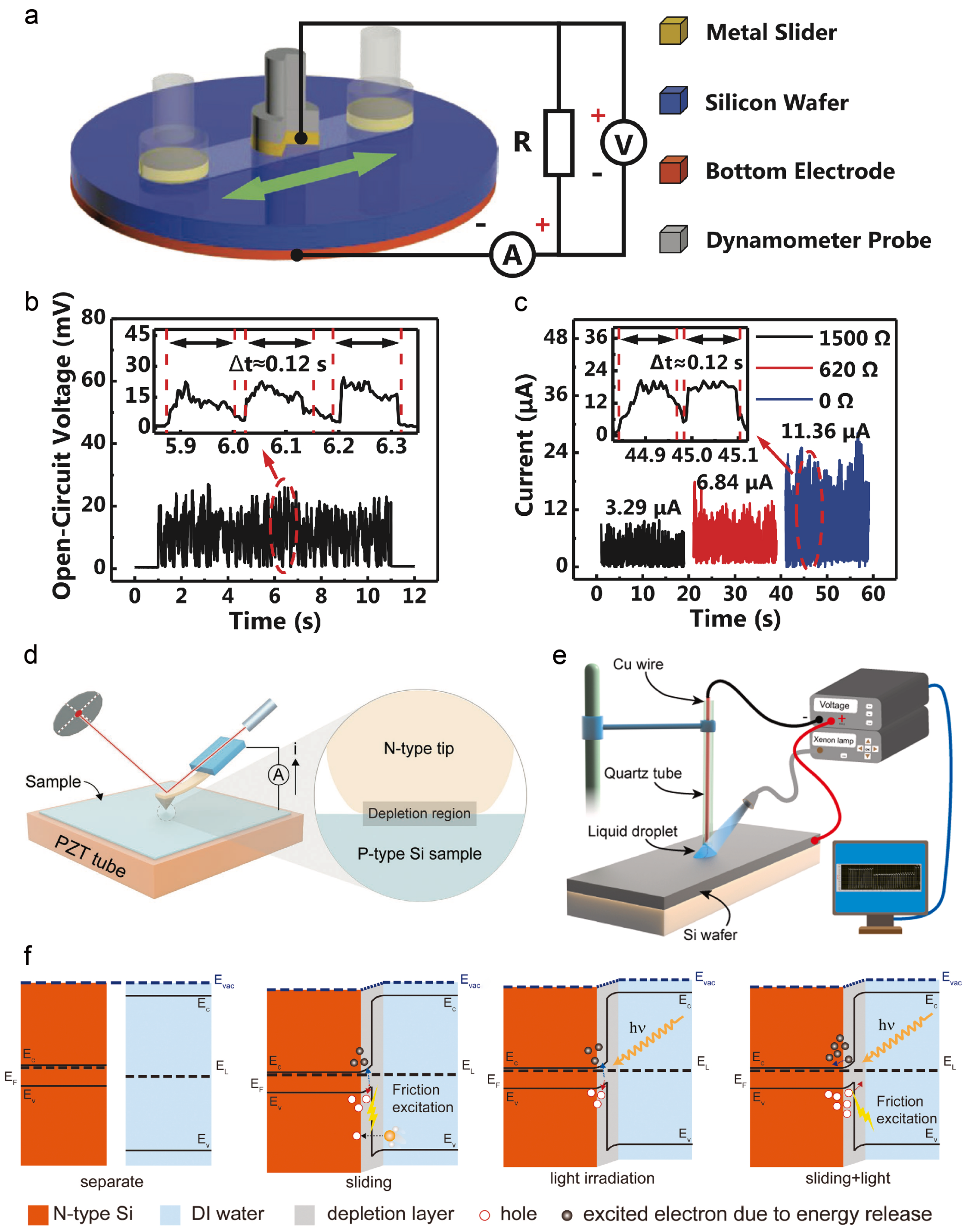

Figure 2.6. Liquid−Solid CE based on Tribovoltaic effect. (a)-(c) The electric output characteristics of the metal-semiconductor-based direct-current triboelectric nanogenerator (MSDC-TENG). (d) The setup of conductive atomic force microscopy experiment platform, the diamond coated tip was controlled to rub on the Si sample with a certain load, during the rubbing, the current between the tip and sample was recorded in the CAFM. (e) The setup of the experiments, the

coupling of photovoltaic effect and tribovoltaic effect at the DI water and Si wafer interface under light irradiation and (f) energy band diagram of the N-type Si and the DI water.

2.3.3 Equivalent Circuit Model of Liquid−Solid TENG

The development of equivalent circuit models has proven to be a valuable approach for understanding and analyzing the electrical behavior of TENGs, including those operating on the liquid-solid interface. The equivalent circuit models of liquid-solid TENGs typically include components such as resistors, capacitors, and current and voltage sources, which capture the various aspects of the device's operation. By utilizing equivalent circuit models, researchers can gain insights into the underlying mechanisms governing the electrical behavior of liquid-solid TENGs. These models enable the optimization of device parameters, such as electrode geometry, material properties, and mechanical motion, to enhance the overall performance and energy conversion efficiency of the TENG system[48-50].

The theoretical frameworks proposed by Niu et al. [51-55], Jiang et al. [56] and Shao et al. [57] provide a solid foundation for developing these models specifically for liquid-solid TENGs. Delving into the realm of basic electrodynamics, TENGs are categorized into five distinct operational modes based on their foundational electrostatic induction processes. These encompass the contact-mode TENGs, sliding-mode TENGs, single-electrode TENGs, freestanding TENGs, and rotary-mode TENGs. Each operational mode of TENG is distinguished by its intrinsic output attributes such as open-circuit voltage, short-circuit transferred charges, and inherent capacitance, which are elucidated comprehensively. As its core, the operative mechanism of TENGs is underscored by a conjugation of contact electrification and electrostatic induction. Through the process of contact electrification, electrostatic charges are engendered and subsequently maintained on the dielectric surface. Subsequently, two equivalent capacitances emerge between the tribo-charged dielectric surface and each of the metal electrodes. As there is a positional shift in the dielectric, alterations in the ratio of these capacitances instigate electron transfer between the metal electrodes under short-circuit conditions. The differential behavior in these capacitance changes elucidates the diverse foundational modes of TENGs. These framework serves as a basis for constructing equivalent circuit models for various TENG configurations, including those operating on the liquid-solid interface.

Wanghuai Xu et al. [58] proposed a droplet-based electricity generator (DEG) based on the finding that continuous impinging water droplets on a fluorinated material lead to a high charge density on its surface. The DEG device, illustrated in **Fig.2.7a**, is constructed by drop-casting polytetrafluoroethylene (PTFE) combined with a small aluminium fragment onto a glass substrate precoated with indium tin oxide (ITO). When a water droplet impinges and spreads on the device, it bridges the previously separate components, resulting in a closed-loop electrical system. In the associated circuit model, the expanding droplet acts as a resistor while the PTFE functions as a capacitor, C_P, with the water/PTFE representing the top plate and PTFE/ITO the bottom plate. In the switched-off state, no capacitor emerges at the water/aluminium juncture, thereby keeping C_P and C_1 in an open circuit, preventing charge flow (see **Fig. 2.7b**). Conversely, in the switched-on state, the connection of the aluminium electrode and PTFE by the water droplet results in the creation of an additional capacitor, C_2, at the water/aluminium boundary, converting the previously open circuit into a closed one. Within the circuit, $\mathrm{R_w}$, $\mathrm{R_L}$ and $\mathrm{d}q_{(t)}/\mathrm{d}t$ in the circuit are the impedance of the water droplet, the impedance of the external load and the time derivative of the transferred charge, respectively. This circuit model effectively predicts the DEG device's output characteristics, aligning with experimental findings.

Hao Wu et al. [59] developed quantitative model of the electrical response caused by the impact of a drop onto an electrical nanogenerator (ENG) surface, as depicted in **Fig. 2.7c.** They deployed millimeter-sized droplets from a specific height onto surfaces that were either horizontal or slightly inclined. These surfaces were coated with an amorphous fluoropolymer (AFP), specifically Teflon. Prior to experimentation, these polymer films were electrically charged. An electrode on the substrate is connected to a thin Pt wire, positioned parallel to the substrate, via an external load resistor R. The comprehensive equivalent circuit of the water drop electricity generator is presented in **Fig. 2.7d**. Here, $C_{env.}$ represents the capacitance from the environment before the water droplet contacts the wire. Given $C_{env.} \rightarrow 0$, it can be considered as an open circuit. Hence, the section of **Fig. 2.7d** involving $C_{env.}$ can be substituted by a switch, S, in the simplified circuit. Upon the droplet's contact with the Pt wire, a faradaic impedance forms at the Pt electrode/electrolyte interfaces. Considering the double layer capacitance is considerably larger than the dielectric capacitance and the overall circuit's capacitance is calculated as $C = (\Sigma\ 1/C_i)^{-1}$, the electric double layer capacitance at the electrode/electrolyte C_i interface, $C_{pt\text{-}el}$, becomes negligible. Similarly, the electric double layer capacitance at the dielectric/electrolyte interface, C_{EDL}, is also negligible within the circuit. As a result, the circuit can be simplified as displayed in **Fig. 2.7e**.

In summary, the development of equivalent circuit models has been instrumental in advancing our theoretical understanding of liquid-solid TENGs. These models, when properly constructed and utilized, provide a powerful tool for analysis, optimization, and design of liquid-solid TENG systems.

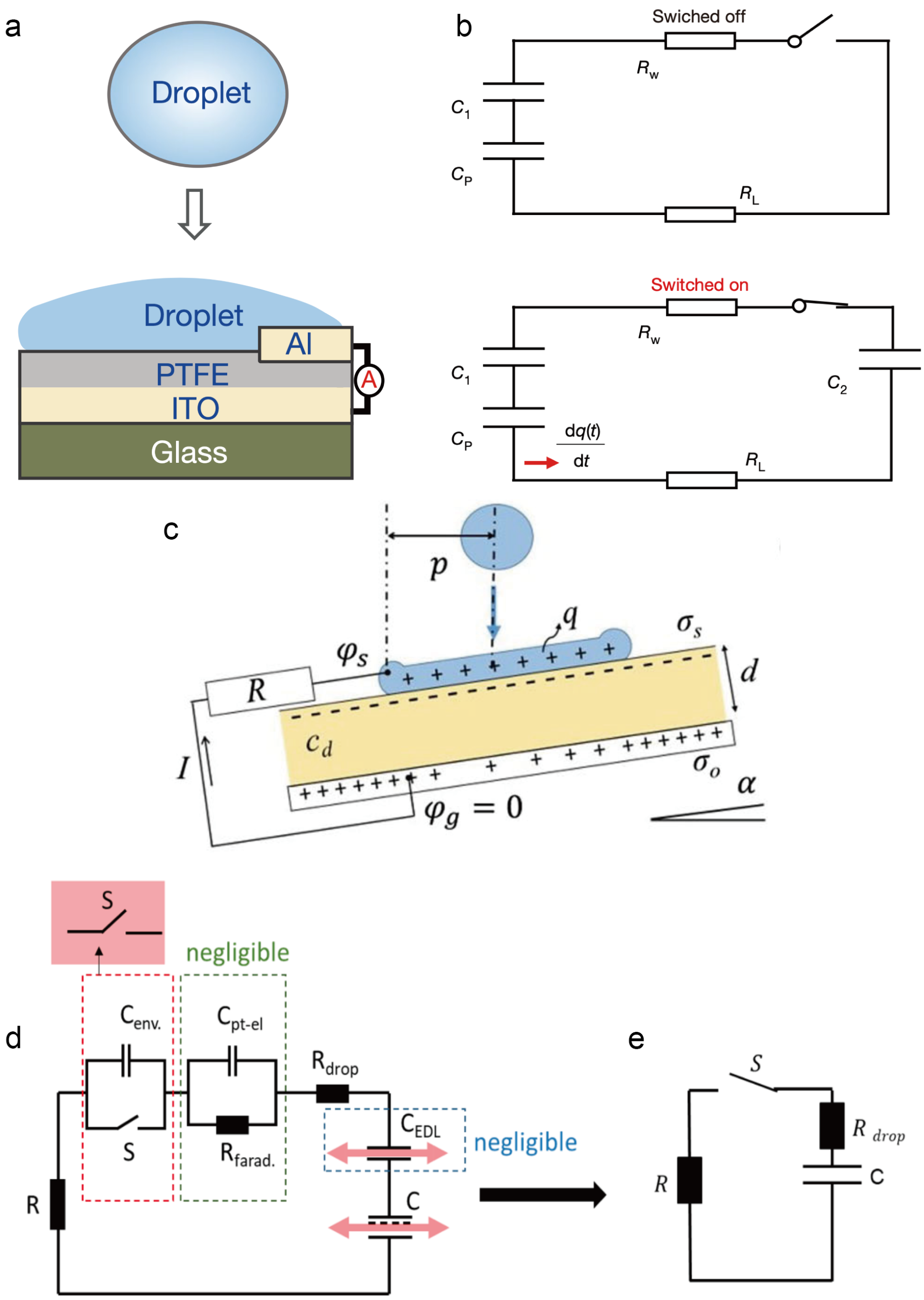

Figure 2.7. Equivalent Circuit Model of Liquid−Solid TENG. (a) Schematic diagram of droplet-based electricity generator (DEG) and (b) circuit model, in the switched-off mode, there is no capacitor formed at the water/aluminium interface. As a result, C_P and C_1 remain in an open circuit and there is no charge flow between them. When the aluminium electrode and PTFE are connected by the water droplet

(switched-on mode), another capacitor, C_2, is established at the water/aluminium interface, forming a closed circuit. R_w, R_L and d$q(t)$/dt in the circuit are, respectively, the impedance of the water droplet, the impedance of the external load and the derivative of the transferred charge with respect to time. (c) Experimental setup, (d) full equivalent circuit and (e) simplified equivalent circuit of the water drop electricity generator.

2.3.4 Mechanisms of Liquid−Solid CE based on the density functional theory

Understanding the mechanisms underlying contact electrification at the liquid−solid interface is essential for unraveling the fundamental processes involved in triboelectric nanogenerators. Density functional theory (DFT) has emerged as a powerful tool for investigating the mechanisms of CE at the atomic and molecular levels. In this section, we explore the insights gained from DFT studies regarding the mechanisms of liquid−solid CE.

Jun Wu et al. [60] conducted an atomic-level investigation on the effect of contact electrification on the liquid-solid electric double layer, utilizing first-principles and molecular dynamics simulations. This study revealed that liquid-solid contact electrification influences not only the concentration distribution of the molecules/ions in the electric double layer but also has the potential to reverse its polarity depending on the specific surface charge density. The proposed mechanism is illustrated in **Fig. 2.8**. When the SiO_2 surface is negatively charged, the electric field generated by these negative charges synergistically amplifies with the inherent local polarized electric field. This mutual enhancement results in the strengthening of the electric double layer (as shown in **Fig. 2.8a**). Conversely, when the SiO_2

surface is positively charged, the electric field generated by these positive charges counteracts its intrinsic local polarized electric field. This opposition leads to a restraint, or even a reversal, of the electric double layer (demonstrated in **Fig. 2.8b**). The underlying principle here is that the surface charge density on the solid surface can substantially influence the adsorption energy between the anion/cation and the solid surface. These findings not only support Wang's two-step model but also offer a more detailed understanding of how liquid-solid contact electrification influences the formation of the electric double layer.

Yang Nan et al. [61] employed density functional theory to study CE at the water/polymer interface. In their work, some representative polymers containing different functional groups and repeat units are selected (**Figure 2.8c**) to investigate CE in contact with water. The study delved into various factors, including the influence of the water layer, molecular chain length, contact modes, electrostatic potential, and work function before and after CE. Their results highlight that electron transfer predominantly occurs at the water/polymer interface when the two materials come into contact. Moreover, only the outermost layer of the water has a significant contribution. The HOMO-LUMO gap states on the surface act as electron acceptors, and notably, a wider HOMO-LUMO gap enhances electron transfer efficiency. Yang Nan's research clarifies the complex mechanisms underlying CE, offering profound insights into the dynamics of charge transfer and distribution at the liquid-solid interface.

The use of DFT in studying liquid-solid CE has also facilitated the exploration of the influence of environmental factors, such as temperature and humidity, on the CE process. By considering the vibrational and electronic properties of the materials, DFT calculations have provided insights into the temperature-dependent charge transfer and the influence of moisture on the CE behavior. Furthermore, DFT simulations have enabled the exploration of the impact of surface modifications, such as coatings or functionalization, on the CE process. These studies have highlighted the importance of surface properties and the potential for engineering the CE behavior through surface modifications.

Density functional theory has provided valuable insights into the mechanisms of liquid-solid CE at the atomic and molecular levels[23; 62-69]. By considering electronic structures, interfacial interactions, and environmental factors, DFT simulations have enhanced our understanding of charge transfer processes, electric double layer formation, and the influence of surface modifications. The combination of DFT studies with experimental investigations paves the way for designing improved liquid-solid TENGs and exploring new applications in energy harvesting.

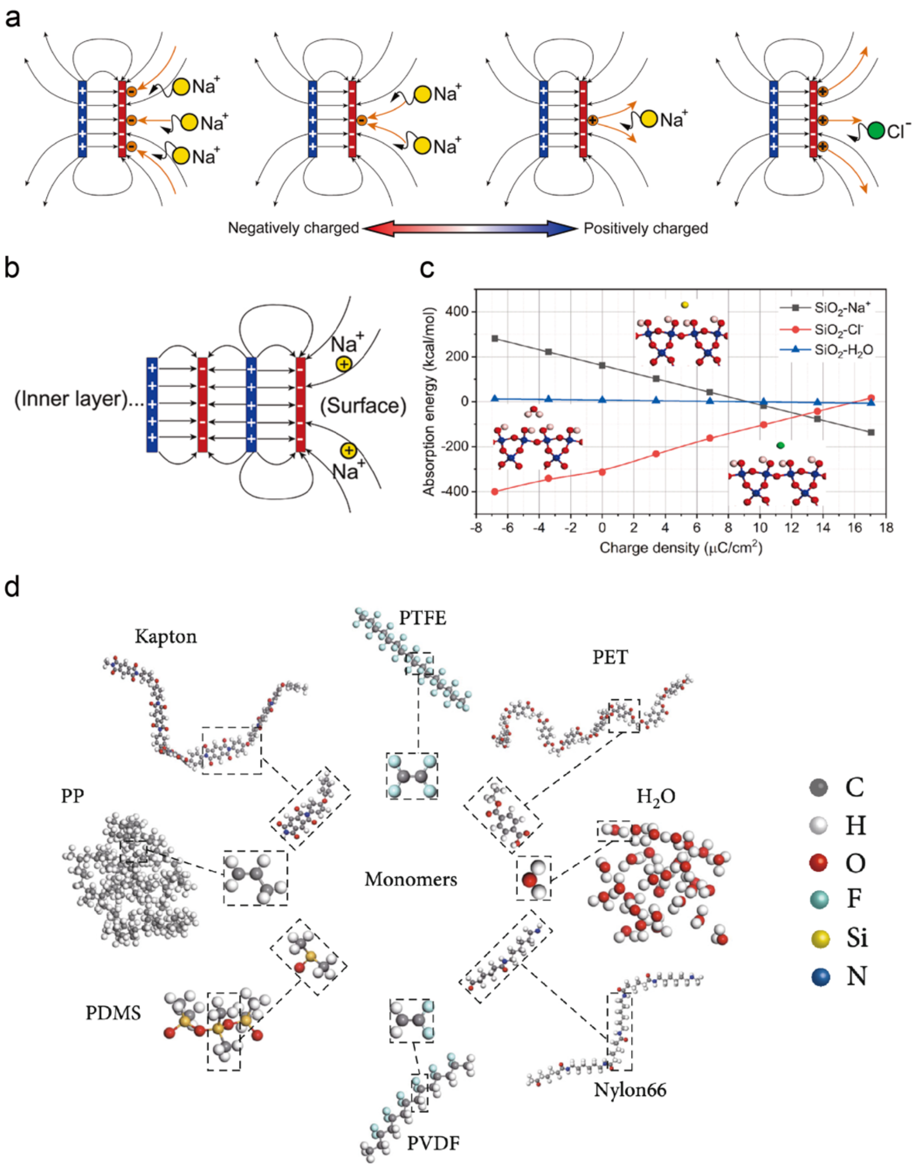

Figure 2.8. (a) The diagrams of influential mechanism of the surface charge density on the formation of electric double layer with the solid surface charged much negatively, less negatively, less positively, and much positively. (b) The analysis of the local polarized electric field on SiO_2 surface. (c) The adsorption energy between SiO_2 surface with Na^+ ion, Cl^- ion, and H_2O molecule under different charge densities. (d) Sketch of seven polymers. Polytetrafluoroethylene (PTFE), polypropylene (PP), polyvinylidene difluoride (PVDF), polydimethylsiloxane (PDMS), Nylon 66, polyimide (Kapton), polyethylene terephthalate (PET), and water. The dashed areas depict their monomers.

2.4 Applications of Liquid−Solid TENG

2.4.1 As micro/nano-power sources

One of the remarkable applications of liquid−solid triboelectric nanogenerators (TENGs) lies in their potential as micro/nano-power sources. The ability to convert mechanical energy into electrical energy at small scales opens up a wide range of possibilities for self-sustained power generation in various microelectronic and nanoscale devices. Micro/nano-power sources based on liquid-solid TENGs offer several advantages over traditional energy harvesting technologies. They can harness ambient mechanical energy sources, such as vibrations, human motion, or fluid flow, to generate electricity, thereby providing a sustainable and self-powered solution. Additionally, liquid-solid TENGs exhibit a compact and lightweight design, making them highly suitable for integration into miniaturized electronic devices and wearable technologies. In this section, we explore the applications of liquid-solid TENGs as micro/nano-power sources and their significant contributions to the field.

Wei Tang et al. [70] introduced the first self-powered water splitting system by integrating a TENG with a water splitting unit (**Figures 2.9a, 2.9b and 2.9c**). When the assembled TENG operates at a rotating speed of 600 rpm, the system yields hydrogen at a rate of 6.25×10^{-3} mL min^{-1} using a 30% (w.t.) KOH solution. Interestingly, when the electrolyte is swapped out for pure water, the water splitting efficiency increases by 4-5 times compared to that powered by an electrochemical workstation, primarily due to the TENG's high voltage output. Moreover, the TENG can be powered by the flow of regular tap water, illustrating its capability as a truly self-sustaining water splitting system. Consequently, TENG-driven water splitting emerges as a viable method for in-situ hydrogen production, whether for energy storage or chemical reactions, without the need for an external power source.

Yang Zou and colleagues [71] reported a bionic stretchable nanogenerator (BSNG) designed for underwater energy harvesting, inspired by the structure of ion channels found in the electrocyte's cytomembrane of electric eels (electrophorus electricus). To replicate this structure, a mechanical control channel was created using the stress-mismatch between polydimethylsiloxane (PDMS) and silicone (**Figure 2.9d**). The BSNG allows two distinctive working modes: achieving an open-circuit voltage of over 170 V in dry conditions and more than 10 V (**Figure 2.9f**) in a liquid environment. These performance metrics are enhanced by combining the benefits of the TENG, positioning the BSNG as a versatile tool for energy harvesting and underwater sensing. Combining the triboelectrification effects from flowing liquid with principles of electrostatic induction, practical underwater applications of this bionic stretchable nanogenerator have been demonstrated, including monitoring human motion in various positions and facilitating undersea rescue systems. With its exceptional flexibility, stretchability, impressive tensile fatigue resistance (surpassing 50,000 cycles), and superior underwater functionality, the bionic stretchable nanogenerator stands out as a promising sustainable power source for soft wearable electronics deployed underwater.

In summary, liquid-solid TENGs offer tremendous potential as micro/nano-power sources, enabling self-sustained energy harvesting for various microelectronic and nanoscale devices[72-78]. Their compact design, ability to harness ambient mechanical energy, and integration capabilities with other technologies make them highly attractive for applications in water splitting, underwater sensing, and beyond. Continued research and development in this area will further unlock the possibilities of liquid–solid TENGs, leading to advancements in self-powered micro/nano-systems and contributing to the field of sustainable energy harvesting.

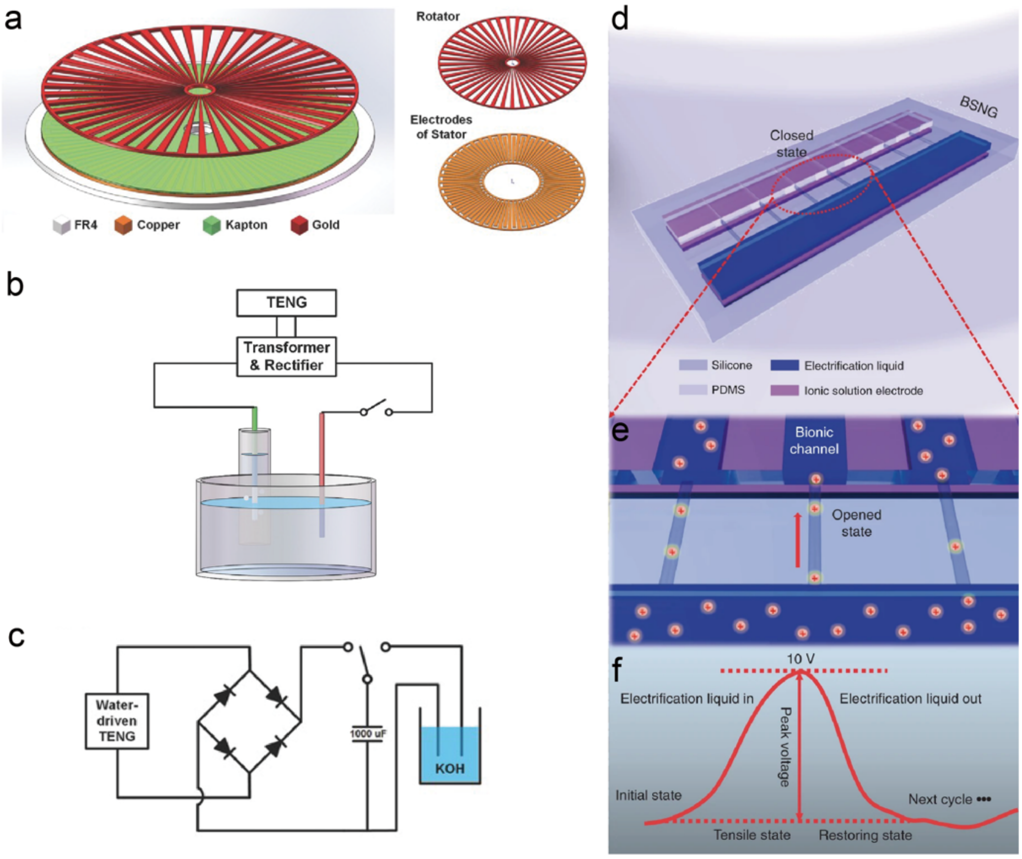

Figure 2.9. (a) Schematic illustrations of the disk TENG, (b) schematic diagram and (c) the circuit diagram of the TENG-driven water splitting system. (d) Scheme diagram of bionic stretchable nanogenerator (BSNG) with double layer structure, which is mainly constructed by silicone, polydimethylsiloxane (PDMS), electrification liquid and ionic solution electrode. (e) Scheme diagram of the bionic channels in BSNG. (f) Output signal of BSNG in one working cycle

2.4.2 As Self-powered sensors

Self-powered sensors represent a significant application domain for liquid-solid triboelectric nanogenerators (TENGs). These sensors have the ability to autonomously generate electrical power from mechanical energy sources in their surrounding environment, eliminating the need for external power supplies or batteries. Self-powered sensors based on liquid-solid TENGs offer several advantages over conventional sensors. They provide a sustainable and independent power source, enabling continuous and reliable operation without the need for frequent battery replacements or wired connections. This feature is particularly advantageous for fluid energy harvesting, where battery life and power availability are critical factors. In this section, we delve into the applications of liquid-solid TENGs as self-powered sensors and their contributions to the field.

Guofeng Song's group [79] reported a water wave motion sensor (**Figure 2.10a**) based on water wave friction. By merging both the mechanisms that the outermost interface friction with water waves and the traditional TENG functionality, the sensor can detect enhancements in water waves at mild frequencies in typical living environments. Through systematic testing under various water levels and frequencies, from low to high, the team observed and analyzed voltage and current signals. These signals can reach up to approximately 60 V and 20 μA (**Figures 2.10b and 2.10c**), respectively, during specific surging wave conditions. Notably, the device can register even minor changes in water levels, clearly visualizing waveform variations. It is anticipated that this technology will showcase significant advancements in environmental monitoring, as well as maritime security and navigation, having profound implications for everyday life.

Fluid energy encompasses a range of sources, from large-scale ones like wave energy to water flow energy, frequently found in rivers and pipelines. A novel water wheel-based hybrid TENG has been developed by Zhong Lin Wang's group [80]. This combines a water-TENG and a disk-TENG to simultaneously harvest both electrostatic and mechanical energies from flowing water (**Figure 2.10d**). The water-TENG features wheel blades coated with superhydrophobic surfaces, which are further covered by PTFE thin films with nanostructures. This design enables the single-electrode-based TENG to harvest electrostatic energy from the water. On the other hand, the disk-TENG consists of two disks. One of these disks rotates in tandem with the wheel blades when impacted by flowing water, functioning as a rotating disk mode TENG to harvest the water's mechanical energy. Notably, the disk-TENG's short-circuit current is directly proportional to both the rate of flowing water and wind speed (see **Figures 2.10e and 2.10f**). This characteristic highlights the hybrid TENG's potential as a self-powered sensor for measuring both water flow and wind speed. The hybridized TENG provides a novel approach to harvest multiple types of energies from the environment.

In addition to wave energy and water flow energy, droplet energy serves as an important source of liquid sensing. Leveraging droplet energy sensing, Jie Chen et al. [81] introduced a self-powered triboelectric microfluidic sensor (TMS). This sensor capitalizes on the signals generated from droplets or bubbles through capillary action and the triboelectrification effects at the liquid/solid interface, enabling real-time liquid and gas flow detection (**Figure 2.10g**). Through alternating capillaries of different diameters, both the sensor's detection range and sensitivity can be tuned (**Figure 2.10h**). Evidence from monitoring the transfusion process for a patient and observing the gas flow from an injector indicates that the TMS offers significant potential for crafting a self-powered micro total analysis system.

In summary, self-powered sensors based on liquid−solid TENGs offer tremendous potential for a wide range of applications. Their ability to harvest mechanical energy and convert it into electrical power enables continuous and autonomous sensing without the need for external power supplies or batteries. These sensors find applications in environmental monitoring, health monitoring, smart grids, and environmental energy harvesting, providing reliable, sustainable, and self-powered solutions[19; 82-89]. Continued advancements in liquid-solid TENG technology will further enhance the capabilities of self-powered sensors, contributing to the development of innovative and autonomous sensing systems.

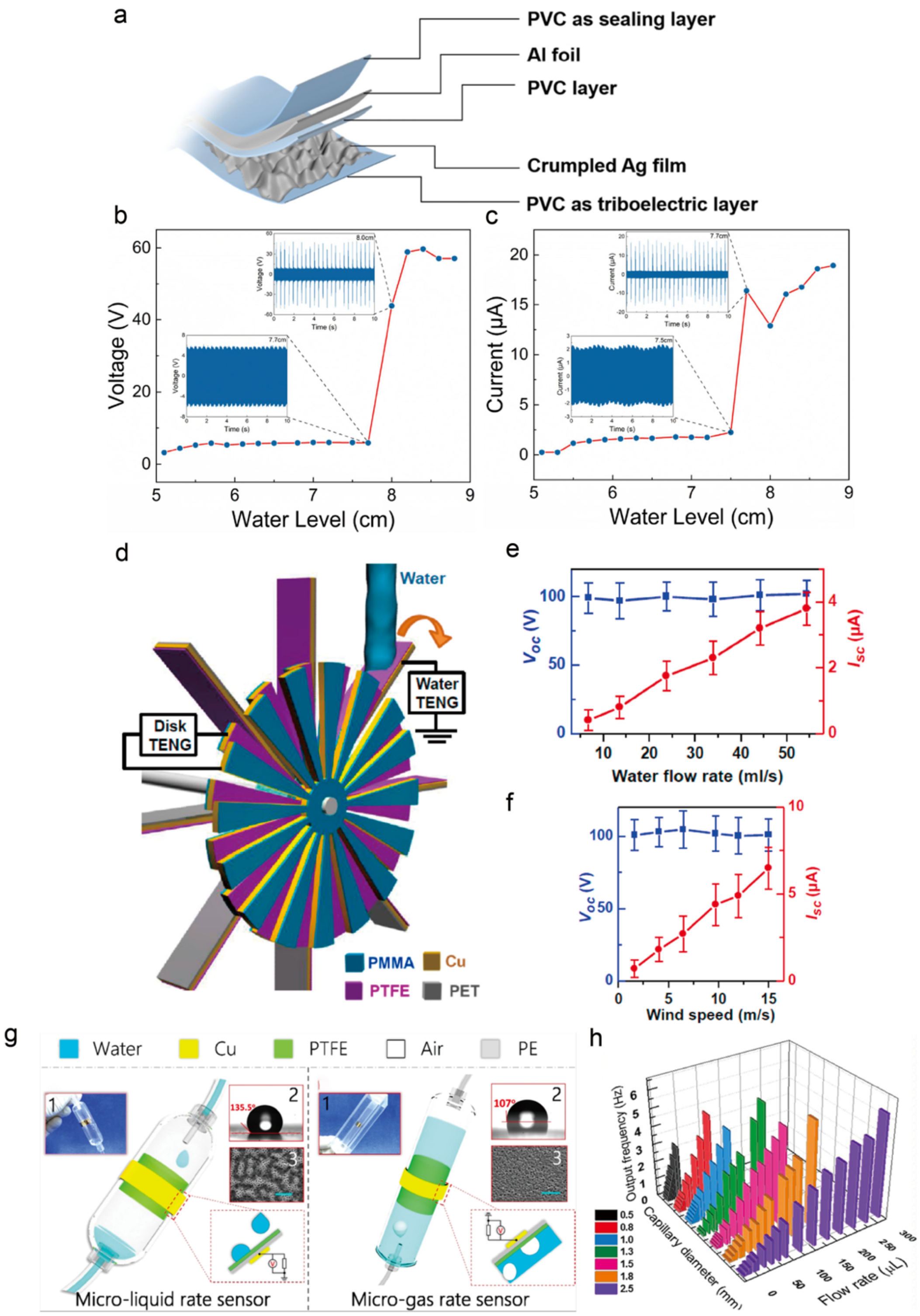

Figure 2.10. (a) Structure of the water wave motion sensor rooted in water wave friction, (b) peak values of voltage and (c) peak values of current for the device. (d) The structure diagram of the hybridized TENG. (e) The dependences of the V_{oc} and I_{sc} values on the flowing water rate of the disk-TENG. (f) The dependences of V_{oc}

and I_{sc} values on wind speed of the disk-TENG when it is driven by wind. (g) Structural schematic diagram of the liquid rate sensor and gas rate sensor. For liquid rate sensor, the inset 1 shows the photograph of the sensor fabricated on a medical infusion tube, the inset 2 shows the surface SEM image of PTFE layer (scale bar: 5 μm), the inset 3 shows the contact angle which indicates the hydrophobic property of the PTFE surface. For the gas flow rate sensor, the inset 1 shows the photograph of the sensor fabricated on a PE tube, the inset 2 shows the surface SEM image of PTFE layer (scale bar: 3 μm), the inset 3 shows the contact angle of the air bubble on the PTFE surface. (h) 3D graph shows the output frequency of self-powered triboelectric micro-fluidic sensor (TMS) with various capillaries under different external flow rate.

2.4.3 As scanning probe

The capability to measure and understand charge transfer at the liquid-solid interface holds promise for a range of scientific applications. Triboelectric nanogenerators (TENGs) have emerged as pivotal tools in this domain, not only as energy harvesters but also as insightful probes for charge transfer dynamics [90].

Jingyang Zhang et al. [91]pioneered in this field with the development of a droplet-TENG, distinguished by its dual spatially arranged electrodes (**Figure 2.11a**). This design aimed to systematically investigate the charge transfer dynamics between liquid droplets and solid substrates. Their findings revealed an intriguing accumulation process of charges during droplet interactions, with electrons emerging as the main charge-transfer agents. Notably, the sensitivity of the droplet-TENG to varying solvent ratios in mixed organic solutions paves the way for potential chemical sensing applications.

Diving deeper into this exploration, the same group unveiled the intricacies of charge transfer during the movement of a water droplet on hydrophobic surfaces[92]. This was achieved through the introduction of a high-density electrode array, termed the pixeled droplet triboelectric nanogenerator (pixeled droplet-TENG). This setup enabled a detailed visualization of charge transfer at the liquid-solid boundary (**Figure 2.11b**). A significant outcome was the generation of an "image" illustrating the transferred charges with remarkable spatial and temporal fidelity. The study revealed a non-uniform distribution of charges along the droplet's pathway, suggesting two-steps mechanism involving electron transfer and subsequent ion adsorption on the solid interface, leading to the formation of an electric double layer.

Such rigorous investigations underscore the profound probing capabilities of TENGs. With potential applications extending across surface chemistry, physics, materials science, and cell biology, the insights derived from these tools highlight the multifaceted roles and significance of TENGs in advanced scientific research.

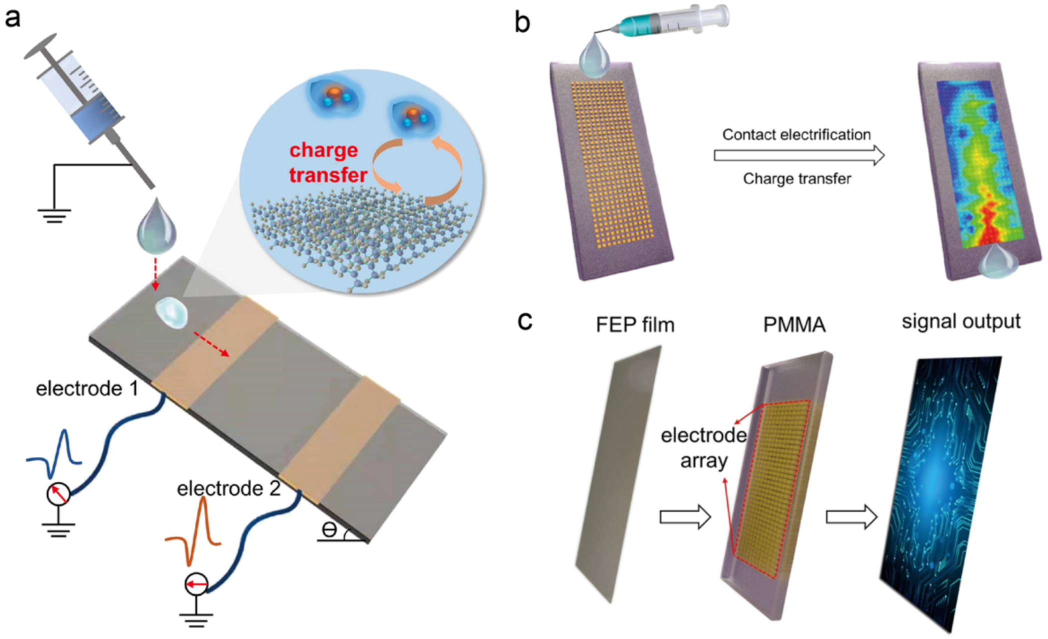

Figure 2.11. TENGs as scanning probe. (a) Working mechanism of the droplet-

TENG. When a drop of liquid flows through the polymer surface, the charge transfer between liquid and solid occurred, and the current signals were measured by the two Cu electrodes separately. (b) Working mechanism of the pixeled droplet-TENG. When a water droplet flows through the tilted fluorinated ethylene propylene surface, the charge transfer between liquid and solid occurred, and the induced charges at each point were measured by the electrode arrays on the backside. (c) Structure of the pixeled droplet-TENG: the top layer is dielectric polymer film (FEP film) for contact electrification with water droplet; the middle layer is a PMMA plate, and the Cu electrode array (12 × 36 Cu electrodes) penetrates the PMMA plate; the bottom layer is a signal processor.

2.4.4 Other applications

Except for the use in micro/nano-power sources, self-powered sensors, and scanning probe applications, liquid-solid TENGs have demonstrated promising potential for various other applications.

Blue energy stands out as one of the most promising sources of renewable energy for expansive applications [90; 93-100]. In this context, liquid-solid TENGs have been proven effective in harnessing large-scale blue energy. Xiaoyi Li and colleagues [101] developed a liquid-solid-contact (LS) buoy triboelectric nanogenerator specifically to harvest blue energy from the ocean (**Figure 2.12a and 2.12b**). This network of buoy LS TENGs can tap into vast energy reserves, capturing both surface wave energy and submarine current energy. Such harvested energy can power portable electric devices or navigation systems. Remarkably, in their study, the electrical energy generated from the LS TENGs was stored in capacitors, driving a wireless SOS (Save Our Souls) radio frequency (RF) transmitter for marine emergencies. Their research not only offers a more efficient way to tap into blue energy but also broadens its potential applications.

Additionally, liquid-solid TENGs can be employed in water and wastewater treatment systems to address energy challenges and enhance overall efficiency[102-104]. By harvesting the flowing kinetic energy of water using a rotating triboelectric nanogenerator (R-TENG), Shuwen Chen et al. [78] demonstrated a self-powered multi-functional system (**Figure 2.12c and 2.12d**). This system is capable of electrochemically eliminating rhodamine B (RhB) and copper ions from wastewater while simultaneously executing metal electrodeposition. With a collection of compelling features, such as high removal efficiency for RhB and copper ions, feasibility for organic pollutants with low concentration, extremely low cost, simplicity, and reusability, their work not only paves the way for sustainable wastewater treatment methods but also facilitates other self-powered electrochemical processes marked by minimal power use and pollution.

Delving into the realm of microfluidics [105-111], the Electrowetting technique serves as a method to manipulate the position and velocity of fluids within microchannels. By intergrating the electrowetting technique with a free-standing mode TENG, Jinhui Nie and his peers [107] have designed a self-powered microfluidic transport system (**Figure 2.12e**). In this setup, a mini vehicle is fabricated by using four droplets to carry a pallet, and it can transport some tiny object on the track electrodes under the drive of TENG. The motion of TENG can provide both driving power and control signal for the mini vehicle. Under the drive of TENG, the minimum volume of the droplet can reach 70-80 nL, while the tiny droplet can freely move on both horizontal and vertical planes. The team also showcased a technique to transport nanoparticles to specified positions. Such an innovative self-powered transportation mechanism holds promise in micro-solid/liquid manipulation, drug delivery systems, micro-robotics, and human-machine interfaces.

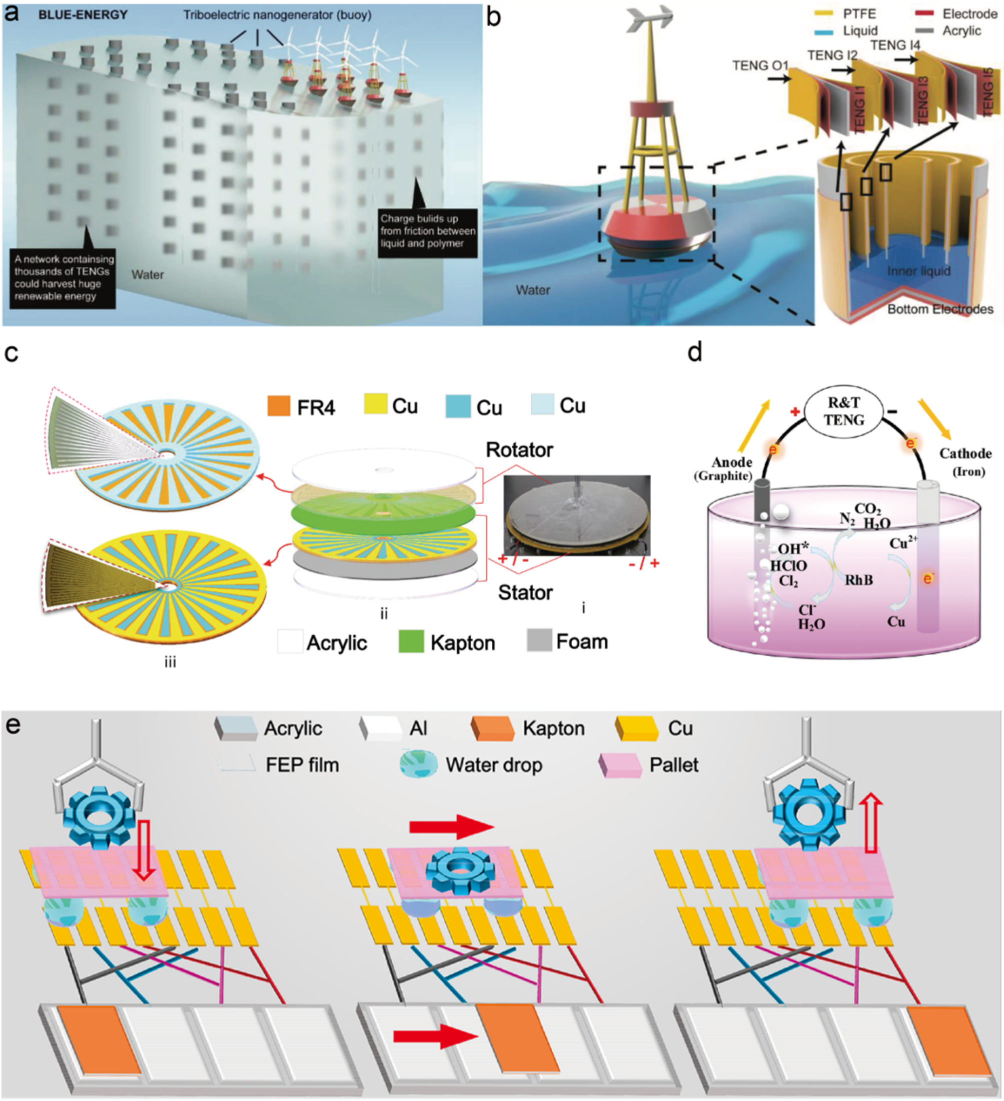

Figure 2.12. (a) The blue energy harvested by the network of the liquid–solid-contact buoy triboelectric nanogenerators. (b) The structure of a buoy, the buoy contains an inner liquid and several polymer films, which function as several TENGs. (c) Illustrations of the R-TENG. (i) the optical image and (ii) the schematic exploded view of the R-TENG which consists of a rotator and a stator. (iii) PCB patterns of the rotator and stator; inserts are the sectional optical images of PCBs.

(d) Schematic diagram of the Cu^{2+} and RhB removing powered by transformed and rectified TENG (R&T TENG). (e) Structure of the self-powered microfluidic transport system based on TENG and electrowetting technique to control the mini vehicle carrying a tiny gear.

2.5 Conclusions and perspectives

2.5.1 Conclusions

The exploration of solid-liquid interface triboelectricity has opened up new horizons in the field of energy harvesting and diverse technological applications. In this literature review paper, we have provided a comprehensive overview of the fundamental concepts, working modes, physical fundament, mechanisms, and applications of liquid-solid triboelectric nanogenerators.

We began by discussing the motivations behind the exploration of liquid-solid TENGs, highlighting the need for sustainable energy harvesting and the unique advantages offered by liquid-based environments. We explored the three fundamental working modes of liquid-solid TENGs: the liquid-dielectric mode, the liquid-semiconductor mode, and the liquid-metal mode. Each mode presented distinct properties and mechanisms, allowing for versatile energy harvesting capabilities.

The physical fundament of liquid-solid TENGs was examined, focusing on the "Wang Transition" for Contact Electrification and Wang's Hybrid Electric Double Layer model. These concepts provided a theoretical understanding of the charge transfer processes and the formation of electric double layers at the liquid-solid interface. Furthermore, we explored the mechanisms of liquid-solid CE based on density functional theory, shedding light on the underlying principles governing the charge transfer phenomenon. The charge states at the liquid-solid interface were investigated, emphasizing their significance in understanding the complex nature of charge transfer processes and their implications for device performance and energy harvesting efficiency. By employing advanced characterization techniques and theoretical models, researchers have made significant progress in unraveling the intricacies of charge states at the interface, paving the way for further improvements in liquid-solid TENGs.

Additionally, we discussed the broad range of applications enabled by liquid-solid TENGs. These applications encompassed micro/nano-power sources, self-powered sensors, scanning probe systems, as well as other emerging fields such as blue energy harvesting, water and wastewater treatment and the electrowetting techniques. These applications showcased the versatility and potential of liquid-solid TENGs in addressing energy challenges and contributing to technological advancements across various domains.

In conclusion, the exploration of solid-liquid interface triboelectricity has provided a new paradigm for energy harvesting and diverse applications. The unique characteristics of liquid-based environments, coupled with the advancements in understanding the fundamental principles and charge transfer mechanisms, have paved the way for the development of efficient and versatile liquid-solid TENGs. While significant progress has been made, there are still challenges to be addressed, such as improving device efficiency, stability, and scalability.

2.5.2 Perspectives

Despite its potential, interface triboelectricity is still a relatively new and emerging field. As such, there is still much to be discovered and optimized.

The rising demand for sustainable and renewable energy solutions positions TENGs as pivotal contributors, with their scalability and efficiency aligning with these global needs. Key to their advancement is the research focus on material optimization and design enhancement. The performance of TENGs heavily relies on the material properties, including their triboelectric behavior, electrical conductivity, and mechanical flexibility. Researchers can focus on discovering new materials or engineering existing ones to enhance the performance, stability, and durability of TENG devices. The integration of functional materials, such as piezoelectric or ferroelectric materials, can also enable multifunctional energy harvesting devices.

Additionally, the understanding and control of the liquid-solid interface play a critical role in the performance of TENGs. Future studies can focus on interface engineering to improve charge transfer efficiency and reduce energy loss. This includes exploring surface modification techniques, such as surface functionalization, nano structuring, and surface coatings, to enhance the interaction between the liquid and solid surfaces. Furthermore, optimizing the interface configuration and geometry can lead to improved charge generation and collection, thereby enhancing the overall performance of TENGs.

Despite significant progress, there is still much to learn about the fundamental mechanisms governing solid-liquid interface triboelectricity. Researchers can delve deeper into understanding the charge transfer processes, interface phenomena, and energy conversion mechanisms at the molecular and atomic levels. Advanced theoretical modeling, computational simulations, and experimental techniques can be employed to unravel the complex dynamics occurring during contact electrification and charge separation at the liquid-solid interface.

Chapter 3. Experiments and Modeling

3.1 Introduction

The pursuit of understanding and improving water-solid mode triboelectric nanogenerators necessitates a combination of practical experimentation and computational modeling. This chapter delves into the detailed experimental methodologies utilized throughout this doctoral thesis, offering insights into the fabrication processes of different TENG configurations. Additionally, a comprehensive overview of the equipment and software leveraged to derive and validate the research findings is provided. While the instruments highlighted in this section are mainly for observation, measurement, and the transfer or exportation of research data, it's important to note that common tools for data analysis, such as graphical representation software, are not included.

3.2 Fabrication Processes

3.2.1 Basic Water−solid Mode TENG

The Water-Solid Mode TENG signifies a pivotal advancement in the domain of triboelectric nanogenerators. A schematic representation of this innovative design is depicted in **Figure 4.1a**, while **Figure 4.1b** offers a real-life glimpse of its dynamic moving part structure.

The fabrication of this distinctive TENG model entailed the following process:

1. Selection of Triboelectric Materials: The chief materials chosen for their exceptional triboelectric properties were polyimide (often referred to as Kapton) tape and polytetrafluoroethylene (PTFE) films. The inherent properties of these materials make them suitable for efficient charge transfer and long-term durability.

2. Electrode Construction: A layer of copper (Cu) was meticulously deposited onto the Kapton tape, serving as the primary electrode. This composite was then

firmly anchored onto a 3D-printed substrate board, measuring 5 × 5 cm^2.

3. Secondary Electrode: A separate Cu layer was affixed to the base of a standard Petri dish, functioning as the secondary electrode. This ensures stable electron transfer and minimizes potential losses.

4. Circuit Connection: The two electrodes – one on the substrate board and the other on the Petri dish – were then interconnected using a conductive wire, culminating in the formation of the external circuit.

5. Operation Principle: As illustrated in **Figure 4.1a**, the moving part of the TENG undergoes vertical displacements within deionized (DI) water. This motion instigates potential disparities between the two electrodes. As a result, the ensuing potential gradient drives the electrons' flow across the external circuit, effectively producing an electric current.

3.2.2 Water-solid Mode based Single-Wire TENG

Building upon the foundational principles of the Water-Solid Mode TENG, the single-wire TENG introduces a compact and efficient configuration. **Figure 4.3a** provides a schematic representation of this innovative design. Central to its structure is a copper (Cu) wire, with a diameter of 1.2 mm, serving as the primary electrode. This choice was based on the wire's known conductive properties, ensuring optimal electron transfer, and its malleability, allowing for specific shape configurations. The wire was carefully treated and cleaned to remove any surface impurities, ensuring the best possible contact interface for the triboelectric process. The wire was then integrated into the TENG system, involving meticulous calibration steps to ensure its alignment, stability, and optimal performance. Such a unique configuration not only simplifies the design but also optimizes space utilization, paving the way for more efficient and scalable energy harvesting systems.

3.2.3 Three-Dimensional TENG Array

By capitalizing on the modular nature of the single-wire TENG design, a more extensive, three-dimensional water-solid TENG array can be realized. To construct this array, individual Single-Wire TENGs were first fabricated as described earlier. These units were then strategically placed in parallel configurations, ensuring minimal interference between adjacent units while maximizing collective output. Connections were established using highly conductive interfaces, ensuring loss-less electron flow between the units. A critical phase in this fabrication was ensuring the structural integrity of the array. To this end, specialized fixtures and mounts were used to hold the Single-Wire TENGs in place, ensuring a consistent spatial orientation across the array. Once the array was set up, tests were conducted to ascertain uniform movement across all TENG units when subjected to water-solid interactions. This would guarantee that all the Single-Wire TENGs in the array contributed uniformly to the overall energy generation. A clear depiction of this array is provided in **Figure 4.6a**'s schematic. This advanced design facilitates improved energy harvesting by leveraging the collective potential of individual TENG units, thereby enhancing the overall performance and scalability of the system.

3.3 Experimental equipment

3.3.1 Electrical measurement system

In the endeavor to measure the electric output signals from the TENG devices, a meticulous setup was established. Key indicators such as the transferred charges (Q_{SC}) and open-circuit voltage (V_{OC}) were of paramount importance in understanding the devices' performance. Central to this setup was the Agilent DSO-X 2014A digital oscilloscope, which offered precise visualization and tracking of the Q_{SC} and V_{OC} in real time. This provided immediate insights into the performance metrics and operational efficiency of the TENG devices. In parallel, the current generated by the devices was accurately measured using the Keithley 6514 current preamplifier. Delving further into the electrical measurements ecosystem, it comprises two main components: the digital multimeter (DMM) and the Labview platform. The relationship and functions of these components are illustrated in **Figure 3.1.** The DMM, specifically the Keithley 6514 model, stands out as the chief data collection instrument, adept at gauging a spectrum of electrical parameters, encompassing voltage, resistance, and electrical current. Once this data is collected, it is seamlessly transferred to the programmed Labview platform. This interface, tailored for this research, facilitates easy visualization of the data, enabling quick analysis of trends and variances. Beyond just visualization, the Labview platform also serves as a robust tool for data export, ensuring that findings can be archived, shared, or subjected to further analysis.

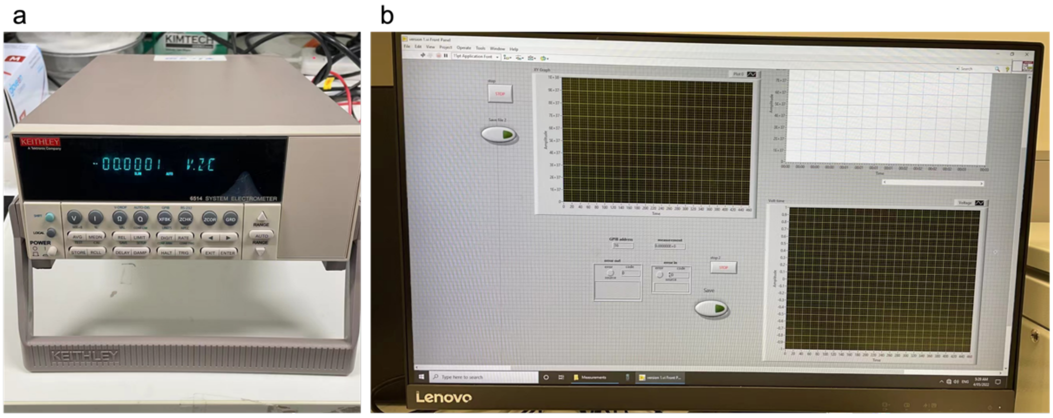

Figure 3.1. Electrical measurement system includes two parts: (a) digital multimeter and (b) the Labview platform.

3.3.2 Linear motor

The precision of solid-liquid contact is pivotal for the efficacy of the Water-Solid Mode TENG. For this purpose, a linear motor (**Figure 3.2**) was employed in our setup. Distinguished from conventional motors, linear motors enable direct, consistent, and controlled linear movements, ensuring optimal interaction within the TENG.

The benefits of the linear motor in this context are:

Positional Accuracy: Ensuring the solid component interfaces precisely with the liquid phase, optimizing the triboelectric effect.

Reproducible Motion: Guaranteeing consistent motion and contact across multiple test cycles, vital for credible data collection.

By automating the solid-liquid contact, the linear motor enhanced both the performance of the TENG and the reliability of the experimental outcomes.

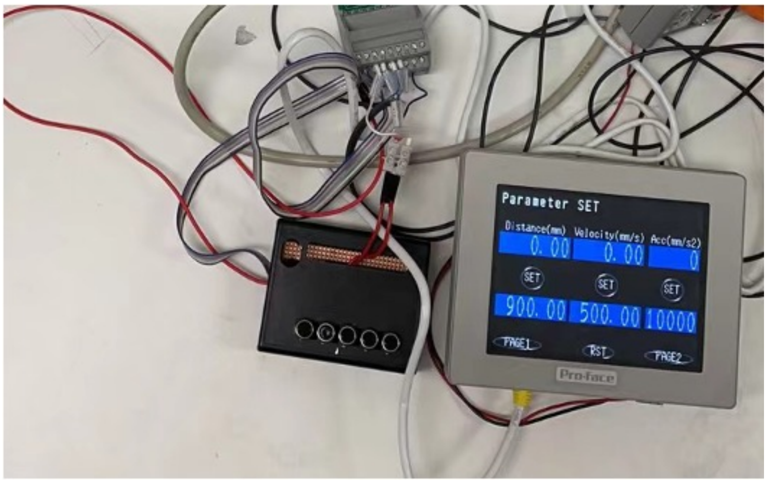

Figure 3.2.1 The controller of the liner motor.

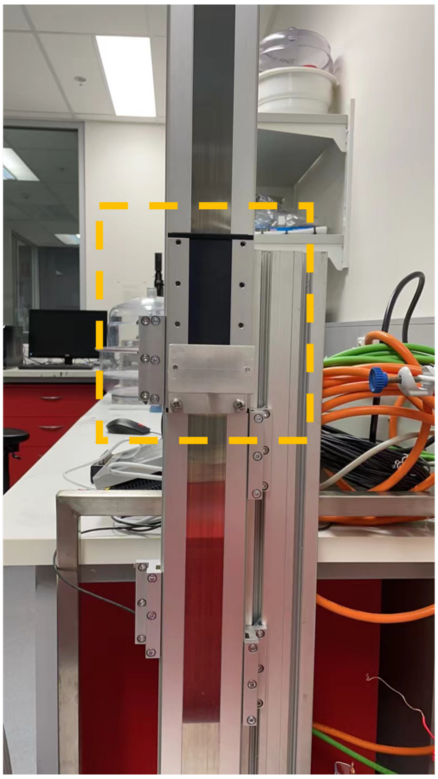

Figure 3.2.2 The moving motor of the liner motor.

3.3.3 3D Printer

3D printing, fundamentally a process of creating objects by adding layers of material through computer-controlled devices, offers unparalleled precision in materializing intricate three-dimensional designs. The printer, characterized by its simplicity yet effectiveness in this study, is fortified with a 3-axial stage and a motor (**Figure 3.3**). Directed by a custom-designed computer program, the motor ensures the accurate delivery of raw materials, forming each layer to exact specifications.

Leveraging this technology ensured that the substrate of the Water-Solid Mode TENG was tailored for optimal performance. The ability to iterate designs rapidly meant the substrate could be perfected to maximize the triboelectric effect. Moreover, the material chosen, primarily plastics in this context, ensured durability and compatibility with the TENG's other components.

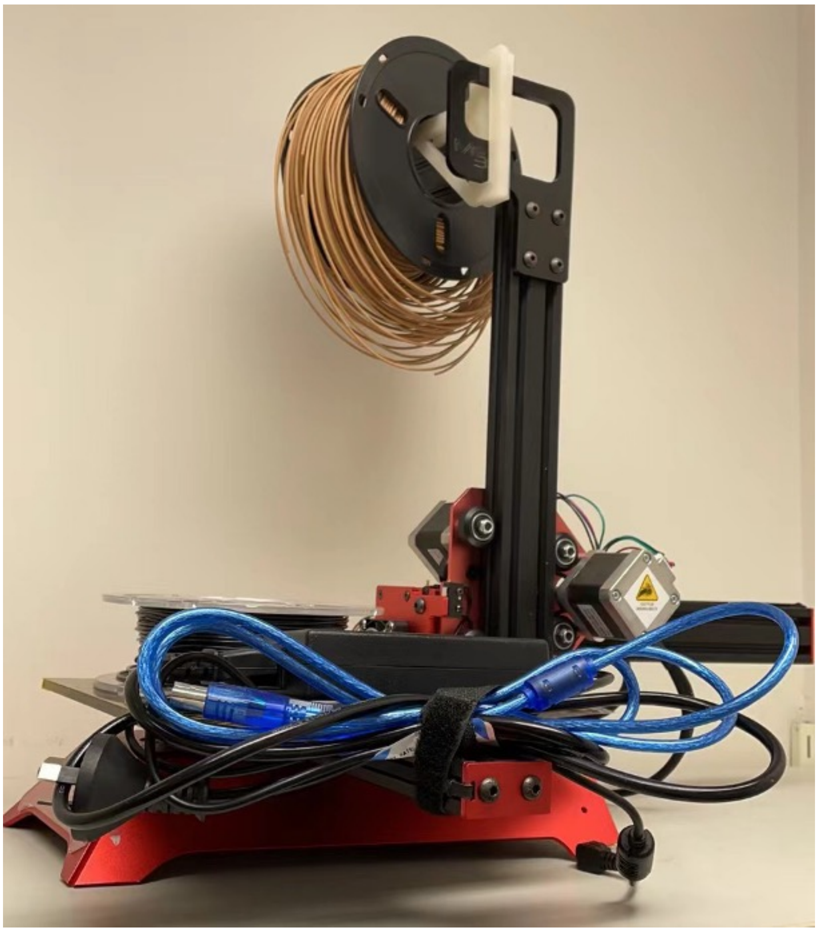

Figure 3.3. Me3D (Australia) 3D printer consists of a 3-axial stage and motor. The raw materials are driven by the motor which is controlled by a specially designed program on the computer.

3.4 Modeling and Simulation

3.4.1 Introduction to COMSOL Multiphysics

COMSOL, renowned for its versatile and comprehensive simulation capabilities, facilitated a deeper understanding of the dynamics at play within the TENG. This software suite, with its powerful multiphysics platform, enabled us to model complex interactions between different physical phenomena – an essential feature when examining the nuanced operations of TENGs. Several advantages of employing COMSOL in our research include:

Multi-domain Analysis: COMSOL's capacity to handle electrical, mechanical, and fluid dynamics allowed for a holistic evaluation of the TENG's behavior. This holistic approach provided a more comprehensive understanding of the TENG's performance and response to various conditions.

User-friendly Interface: Despite its intricate capabilities, COMSOL's intuitive design ensured a seamless learning curve, enabling swift design iterations.

Parameterized Studies: The software's ability to perform parameter sweeps allowed us to conduct optimization studies, fine-tuning various parameters to achieve maximum efficiency. This optimization process was crucial in refining the TENG's design and ensuring its performance met our expectations.

In summary, COMSOL's versatile simulation capabilities, user-friendly interface, and parameterized studies feature significantly contributed to our research on TENGs. The software suite enabled us to gain a deeper understanding of the TENG's dynamics, iterate on designs efficiently, and optimize its performance for maximum efficiency.

3.4.2 Detailed Simulation Process

For ensuring the accuracy and reproducibility of our simulation results, we adhered to a standardized procedure utilizing the COMSOL Multiphysics software, version 5.6. Our work centered on constructing a quasi-static model aimed at simulating the electrostatic induction between a dielectric sphere and copper rings using the AC/DC module in COMSOL.

Model Initialization: Each TENG design was virtually recreated in COMSOL, ensuring all dimensions, materials, and properties matched their real-world counterparts. The dielectric sphere was assigned a dielectric constant of 4.4, while the copper rings were modeled as perfect conductors with a conductivity of 5.998 × 10^7 S/m. Detailed geometric parameters for both elements were established based on the experimental setup and are provided in chapter 6.3.

Boundary and Initial Conditions: Conditions mimicking the experimental environment were set. This included setting up electrical potentials, defining solid-liquid interaction parameters, and ensuring all physical conditions were mirrored.

Meshing: Given the intricate nature of TENGs, a fine mesh was employed to capture the minutest of details. This ensured that all interactions, especially at interfaces, were accurately captured.

Simulation Run: With everything set, the simulation was run. During this phase, data on electrical outputs, potential differences, and other relevant parameters were captured.

Data Analysis: Post-simulation, the data was exported and analyzed. This step was crucial in drawing parallels between the simulation and experimental results.

By adhering to this meticulous procedure, we ensured that our simulations were not only accurate but also consistently reproducible, fortifying the credibility of our research findings.

Chapter 4. Electrification performance and working mechanism of water-solid mode TENG

4.1 Abstract

With the advantages of superior wear resistance, mechanical durability, and stability, the liquid-solid mode triboelectric nanogenerator (TENG) has been attracting much attention in the field of energy harvesting and self-powered sensors. However, most reports are primarily observational, and there still lacks a universal model of this kind of TENG. Here, an equivalent circuit model and corresponding governing equations of a water-solid mode TENG are developed, which could easily be extended to other types of liquid-solid mode TENGs. Based on the first-order lumped circuit theory, the full equivalent circuit model of water-solid mode TENG is modeled as a series connection of two capacitors and a water resistor. Accordingly, its output characteristics and critical influences are examined, to investigate the relevant physical mechanism behind them. Afterward, a three-dimensional water-solid TENG array constructed from many single-wire TENGs is fabricated, which can not only harvest tiny amounts of energy from any movement of water, but also can verify our theoretical predictions. The fundamentals of the water-solid mode TENG presented in this work could contribute to solving the problem of electrical phenomena on a liquid-solid interface, and may establish a sound basis for a thorough understanding of the liquid-solid mode TENG.

4.2 Introduction

Researchers have attempted to understand and utilize contact electrification (CE) for many centuries. [112-114] CE occurring at liquid−solid interfaces usually endows the liquid (water or an aqueous solution) with specific electric charges, which accordingly leads to the formation of an electrical double layer (EDL) within the fluid.[115-118] A well-known example is that when the water surface is broken or brought into contact with a solid, electric charges are generated on the interfaces, and an EDL is formed in this complex system. Recently, it has been proposed that there are two steps, including the electron exchange and ion adsorption, for the generation of an EDL, which will be comprehensively researched in the foreseeable future. This two-step model is called the Wang model for EDL, and the relevant hybrid layer is called Wang's hybrid layer.[12; 13; 69] On the other hand, CE occurring at water-solid interfaces is utilized to harvest energy in the small-scale energy range from macroscopic to microfluidic devices.[58; 59; 119-122] Moon et al. has demonstrated that mechanically changing the contact area at the liquid-solid interface essentially modulates the electrical double layer, thereby generating an electrical current.[115] In a recently study by Xu and Wang et al., it was found that spreading of a water droplet on an electric generator gains an enhancement to its instantaneous power density.[58] However, this type of small-scale energy harvesters have to overcome inevitable difficulties in actual applications, such as water evaporation, water splashing, or extremely small instantaneous currents generated under a low frequency.[119; 120]

To overcome the above problems, a special energy harvesting device, that is, the water-solid mode triboelectric nanogenerator (TENG) has been designed, which can improve the basic output by several orders of magnitude over the droplet-based devices as mentioned above. This is mainly because a droplet is replaced by great quantities of water, which leads to the increase in contact area, making the interfacial effect more obvious. For instance, a highly symmetric three-dimensional (3D) spherical-shaped water-based TENG was designed by Shi et al., which can be effectively utilized to harvest energy from water waves with random direction/amplitude because its inner surface and outer surface are in direct contact with the water. [123] To date, a large number of water-based mode TENGs have been invented, [121; 122] owing to the great advantages of this type of TENG, such as superior wear resistance, good mechanical durability, and stability, etc. [124-128] These consistent reports are primarily observational, however, and they are generally difficult to reproduce, especially because no universal model has been developed.

In this work, we have achieved a comprehensive understanding of the physical mechanisms of the water-solid mode TENG, through our equivalent circuit model and clear physical picture. First, the EDLs and corresponding EDL capacitors (EDLCs) formed on the water-solid interfacial areas are systematically analyzed. The two EDLCs and the resistance of the water are connected in series, from which a full equivalent circuit model and governing equation are proposed, based on the first-order lumped-circuit theory. On mechanically modulating the EDLs, the voltages across the EDLCs and the potential difference between the two electrodes change, consequently giving rise to the generation of a conduction current in the external circuit. In addition, a three-dimensional water-solid mode TENG array constructed from many single-wire TENGs is fabricated, which can not only convert energy from any movement of water, but also verify our predictions and theoretical analysis.

4.3 High-Electrification performance and working mechanism of the water-solid mode triboelectric nanogenerator

4.3.1 The basic water-solid mode TENG

The typical water-solid mode TENG comprises of a multidielectric layer constructed from polyimide (Kapton) tape and polytetrafluoroethylene (PTFE) films, deionized (DI) water, and two electrodes. **Figure 4.1a** shows a simple schematic diagram of this device, from which it is seen that the PTFE (hydrophobic) surface is directly exposed to DI water. A picture of the substrate attached with the multidielectric layer is presented in **Figure 4.1b**. When PTFE comes into contact with other materials, due to its high electronegativity, it tends to attract electrons from those materials. This attraction results in the accumulation of negative charges on the surface of PTFE. These negative charges do not dissipate immediately even when the contacting surfaces are completely separated. This stability is attributed to the electronegative characteristics of PTFE, which allow it to maintain the charges even in the absence of an external power source. In our experiments, when CE first occurs between the DI water and the PTFE, negative charges are generated on the hydrophobic surface and positive charges on the water surface (**Figure 4.1e**). Identifying the origins of the charges on water-hydrophobic interfaces is inherently challenging, owing to the uncertainties in their interfacial structures and known surface chemistry. Here, we accept the postulate that hydroxyl ion adsorption is the source of charge on hydrophobic surfaces and that EDLs are formed at the liquid-solid interfaces.[129] As shown in **Figure 4.1e**, the negative charges distributed on the PTFE surface generate an electric field, pulling oppositely charged ions toward this hydrophobic surface and pushing like charges away from it. Since the opposite electric charges (counterions) are distributed very near the PTFE surface, they then shield the water solution from those negative charges. According to the charge neutrality condition, the total charge is zero, but the dipole moment close to the interface region is not zero. This charge distribution structure in the fluid is well-known as the EDL or the Debye layer.[130] Because the geometry and structure of the charge distribution is equivalent to that of a conventional parallel plate capacitor, it is regarded as an electrical double layer capacitor (EDLC), as depicted in **Figure 4.1c**. There are two different EDLCs formed in the water-solid mode TENG, with the one distributed at the water-PTFE surface, while the other is formed at the water-bottom electrode surface.

Figure 4.1c illustrates the modeled EDL and EDLC in the water-solid mode TENG. Note that the double layer is formed by a compact layer of charges next to the charged surface (PTFE) followed by a diffuse layer extending into bulk solution (DI water). We assume that the capacitance near the water-PTFE surface (C_{top}) is comprised of two capacitors, C_i and $C_{EDLC,t}$, which are connected in series form. The C_i and $C_{EDLC,t}$ represent the capacitance of the dielectric and the EDLC formed at the water-PTFE interfacial area, respectively. It should be emphasized that the C_{top} is a nonlinear capacitor due to the change in the $C_{EDLC,t}$. Strictly speaking, this $C_{EDLC,t}$ is a typical voltage-dependent capacitor, and its capacitance is regarded as a differential capacitance, which can be calculated by the rate of the stored charge divided by the rate of change of the voltage across the EDLC. As the free charges distributed on the surface of the top electrode vary with time, the total electric field applied on the water-PTFE surface changes, leading to variation in the charges distributions in both the compact layer and the diffuse layer, and the length of the relevant EDL. Therefore, the $C_{EDLC,t}$ and C_{top} all change with time. By the same token, the $C_{EDLC,b}$ that is formed at the water-bottom electrode interfacial area is also a typical differential capacitor. Two points should be noted. The first one is about the fundamental basic of charge generation on the liquid-solid interfaces. It has been proposed by Wang that electron exchange between the liquid (water) and the solid (PTFE film) at the interface is an inevitable step when CE occurs, which can be described by an overlapped electron cloud model between water molecules and solid surface atoms.[130; 131] In particular, electron transfer and ion adsorption usually happen simultaneously. Furthermore, it is apparent that the EDLCs (including the $C_{EDLC,t}$ and $C_{EDLC,b}$) can be mechanically modulated under different structure parameters and motion conditions.

Based on the above analysis, a full equivalent circuit model of the water-solid mode TENG is proposed. As demonstrated in **Figure 4.1d**, the TENG is modeled by a series connection of C_i, $C_{EDLC,t}$, R_w, and $C_{EDLC,b}$, where C_i represents the time-invariant capacitance caused by the dielectric material such as nylon or PTFE. R_w is the resistance of water (the liquid).[115] Before the moving part comes into contact with water, there is a capacitance from the environment. Given that this capacitor is fairly small, it is regarded existing in at an open circuit condition, and is represented by a switch L. Moreover, R_L represents the external resistance in the external circuit. Assume that the contact area (S_w) between the water and the PTFE changes appreciably during external mechanical excitation. While the contact area (S_b) between the water and the bottom electrode is nearly fixed, the moving part moves up and down within the water. As a result, the total capacitance at the water-PTFE interface C_{top} is approximately proportional to S_w; on the contrary, the capacitance formed at the bottom electrode-water surface (C_{bot}, which is equal to the $C_{EDLC,b}$ in this device structure) is nearly a constant during the oscillation period. It should be clear that the thus-formed EDLC is much lager than that of the dielectric capacitance in general,[59] and these capacitors are connected in series, so that the $C_{EDLC,t}$ can be negligible when calculating the total capacitance.

When the moving part comes into contact with the DI water, an EDLC ($C_{EDLC,t}$)

is formed at the water-PTFE interface, and it is connected with the C_i in series. Here the C_i represents the capacitance of the multi-dielectric layer. Then the total capacitance of the $C_{top(t)}$ is calculated by:

$$C_{\mathrm{top}}(t)=(\frac{1}{C_{\mathrm{i}}}+\frac{1}{C_{\mathrm{EDLC,t}}})^{-1}=(\frac{d_0}{\varepsilon_0 S_{\mathrm{w}}(t)}+\frac{\lambda_{\mathrm{w}}}{\varepsilon_0\varepsilon_{\mathrm{w}}S_{\mathrm{w}}(t)})^{-1}=\varepsilon_0 S_{\mathrm{w}}(t)(d_0+\frac{\lambda_{\mathrm{w}}}{\varepsilon_{\mathrm{w}}})^{-1} \tag{1}$$

where d_0 represents the effective thickness of the multi-dielectric layer, i.e., $d_0 = d_1/\varepsilon_1 + d_2/\varepsilon_2$, where d_1, d_2, and ε_1, ε_2 are the thickness and relative permittivity of Kapton and PTFE respectively. The λ_w and ε_w are the width of the EDLC and the dielectric constant of DI water, respectively. In general, since d_0 is much large than λ_w/ε_w or the capacitance of EDLC is much larger than the dielectric capacitance, so the second approximation in Eq. (1) can be justified. Therefore, we have

$$C_{\mathrm{top}}(t)=(\frac{1}{C_{\mathrm{i}}}+\frac{1}{C_{\mathrm{EDLC,t}}})^{-1}\cong\frac{\varepsilon_0 S_{\mathrm{w}}(t)}{d_0} \tag{2}$$

$$C_{\mathrm{bot}}\cong\frac{\varepsilon_0\varepsilon_{\mathrm{w}}S_{\mathrm{b}}}{\lambda_{\mathrm{w}}} \tag{3}$$

Note that here the S_{w} defines the contact area between the water and the PTFE; and the S_{b} represents the contact area at the water-bottom electrode interface, respectively. Since the S_{b} is nearly fixed, the formed C_{bot} does not change over time. Besides, some typical parameters are provided based on our experimental conditions, in order to calculate the C_{top} and C_{bot}. Because we could not measure the Debye screening length λ_{w} directly, a typical value of λ_{w} = 300 nm is utilized from the published works.[1] Through Eqs. (2) and (3), and the parameters in **Table 4.1**, the capacitance per unit area of $C_{\mathrm{top}}/S_{\mathrm{w}} = 0.364$ μF/m^2 and $C_{\mathrm{bot}}/S_{\mathrm{b}} = 23.02$ μF/m^2. If we have $S_{\mathrm{w}} = S_{\mathrm{b}} = 9$ cm^2, the corresponding C_{top} and C_{bot} are 0.33 nF and 20.72 nF, respectively. As a results, the total capacitance of the water-solid mode TENG system is approximately 0.32 nF, which is in the same order when compared with the typical value of the capacitance of a lateral-slide mode TENG. [41] Therefore, variation of C_{top} mainly comes from the changes of effective thickness of the multidielectric layer d_0, while for C_{bot} it depends critically on the thickness of electrical double layer λ_w.

Table 4.1. Parameters utilized in the numerical calculation.

Structure component	Parameter utilized
Dielectric effective thickness, $d_0 = \sum d_i/\varepsilon_i$	2.43×10^{-5} m
Dielectric 1	$\varepsilon_1 = 3.5$, $d_1 = 50$ μm
Dielectric 2	$\varepsilon_2 = 2.0$, $d_2 = 50$ μm
Dielectric of DI water	$\varepsilon_w = 78$
Permittivity of vacuum, ε_0	8.854×10^{-12} F/m

Figure 4.1e illustrates the charge transfer process in an operation cycle of the water-solid mode TENG. It should be noticed that negative charges are generated on the PTFE surface, and this charged layer remains constant even after the contact surfaces are completely separated owing to the electronegative characteristics of PTFE. As depicted in **Figure 4.1e1**, when the moving part is immersed in water, the electrons are injected from the water surface to the PTFE surface, making the contact surfaces oppositely charged. As the TENG is separated from the water, negative charges remain distributed on the surface of PTFE, which leads to the electric potential of the moving electrode lower than that of the bottom electrode, causing the charges transferred between the two electrodes to maintain electrostatic equilibrium (**Figure 4.1e2**). The generated conduction current in the external circuit keeps flowing until the moving electrode is completely taken out (**Figure 4.1e3**) of DI water. As the moving part comes into contact with the DI water (**Figure 4.1e4**)

again, the charged PTFE surface will be screened due to the formation of EDL at the water-PTFE interface; charges flow from the bottom electrode to the top one, and the counterions in the DI water (liquid) have to redistribute themselves simultaneously to eliminate the potential difference between the two EDLCs ($C_{EDL,t}$ and $C_{EDL,b}$). As a result, alternating current (AC) is generated in the external circuit. When no electrons are transferred, the voltage between the two EDLCs becomes zero, and the system reaches at an equilibrium state. According to Kirchhoff's law, we have

$$\frac{S_{\mathrm{b}}\sigma_{\mathrm{b}}-Q}{C_{\mathrm{bot}}}-\frac{Q}{C_{\mathrm{top}}}=0 \tag{4}$$

here σ_b is the charge density distributed at the bottom electrode, and Q is the decrement or increment of charges in the $C_{EDL,b}$ or $C_{EDL,t}$ in the equilibrium state. In such state, since the C_{bot} is much larger than the C_{top} in most cases, the electric charges distributed in the top EDLC should be much smaller than those distributed in the bottom EDLC. As a result, the potential difference between the two EDLCs is strongly depended on the time-variation of C_{top}. In the nonequilibrium state, assume that the charges stored on C_{top} and C_{bot} are $Q_{top} + Q$ and $S_b\sigma_T - Q$, and that the voltage across each EDLC is φ_{top} and φ_{bot}, respectively. The voltage difference (V) between the two electrodes of the water-solid mode TENG is given by Kirchhoff's law:

$$\frac{S_{\mathrm{b}}\sigma_{\mathrm{b}}-Q}{C_{\mathrm{bot}}}-\frac{Q_{\mathrm{top}}+Q}{C_{\mathrm{top}}}-R_{\mathrm{w}}\frac{dQ}{dt}-R_{\mathrm{L}}\frac{dQ}{dt}=0 \tag{5}$$

and the governing equation can be simplified as

$$(R_{\mathrm{L}}+R_{\mathrm{w}})\frac{dQ}{dt}=-(\frac{1}{C_{\mathrm{bot}}}+\frac{1}{C_{\mathrm{top}}(t)})Q+(\frac{S_{\mathrm{b}}\sigma_{\mathrm{b}}}{C_{\mathrm{bot}}}-\frac{Q_{\mathrm{top}}}{C_{\mathrm{top}}(t)}) \tag{6}$$

where $Q(t)$ is the transferred charge. Accordingly, the time-dependent of C_{top} and the nearly constant of C_{bot} make this governing equation to be a non-linear first-order ordinary differential equation; giving rise to the difficulty of obtaining the analytical solution. If the voltage across the R_L is V_L, it is obtained by:

$$V_{\mathrm{L}} = \frac{VR_{\mathrm{L}}}{R_{\mathrm{L}} + R_{\mathrm{w}}} \tag{7}$$

On the other hand, it has been proved that the solid-solid mode TENG is neutral at any time, and this is the essential reason why it is equivalent to an open circuit voltage (V_{OC}) connected in series with a variable capacitor. [55; 57; 132-134] For the water-solid mode TENG, its full equivalent circuit model is modeled as a series connection of two capacitors C_{bot} and C_{top}, and a water resistor R_w. Through mechanically modulating the two EDLs along with the interfacial areas, mechanical work is converted into electrical energy. Some works have been published to demonstrate the exploitation of EDLC for energy conversion. [135; 136] In addition, we have proved that the total capacitance of this mode TENG is approximately in the same order when compared with a typical value of the capacitance of a lateral-slide mode TENG. [137]

To investigate the effects of key parameters and the relevant physical mechanism behind them, the open-circuit voltage $V_{OC(t)}$, short-circuit transfer charge $Q_{SC(t)}$, and total capacitance $C_{(t)}$ are derived according to the governing equation of the water-solid mode TENG:

$$V_{\mathrm{OC}}(t) = \frac{S_{\mathrm{b}}\sigma_{\mathrm{b}}}{C_{\mathrm{bot}}} - \frac{\sigma_{\mathrm{w}} d_0}{S_{\mathrm{w}}} \tag{8}$$

$$Q_{\mathrm{SC}}(t) = \frac{S_{\mathrm{b}}\sigma_{\mathrm{b}} - \sigma_{\mathrm{w}} d_0 C_{\mathrm{bot}} / \varepsilon_0}{1 + C_{\mathrm{bot}} / C_{\mathrm{top}}} \tag{9}$$

$$C(t) = \frac{\varepsilon_0 \varepsilon_{\mathrm{w}}}{\lambda_{\mathrm{w}} / S_{\mathrm{b}} + d_0 \varepsilon_{\mathrm{w}} / S_{\mathrm{w}}} \tag{10}$$

From Eqs. (8)−(10), the basic outputs of the water-solid mode TENG can be quantitatively predicted. It is important to point out that some reasonable assumptions have been made in this model. Firstly, the electric double layer capacitors formed at the water-solid interfaces are ignored due to the explanations in equation (1)-(4). When the moving part is separated from the DI water, there are no residual water droplets on the surface of the PTFE, *i.e.*, the capillary force between the water and the PTFE surface is not considered. Moreover, we assume that the surface charge densities on the surface of the PTFE film and water do not change with time when the TENG achieves a dynamic equilibrium. Since these methods may avoid some inappropriate approximate hypotheses, the simplified model developed here is no less accurate despite its brevity.

In addition, we have already pointed out that nanogenerators use displacement current as the driving force to convert mechanical energy into electric power/signals. [57; 112; 134] This definition also applies to the liquid-solid model TENGs from the first-principles of classical electrodynamics. In other words, the output characteristic of the water-solid mode TENG is controlled by the Maxwell's displacement current (ID). All-around analysis and simulation of this problem will be developed in our next work.

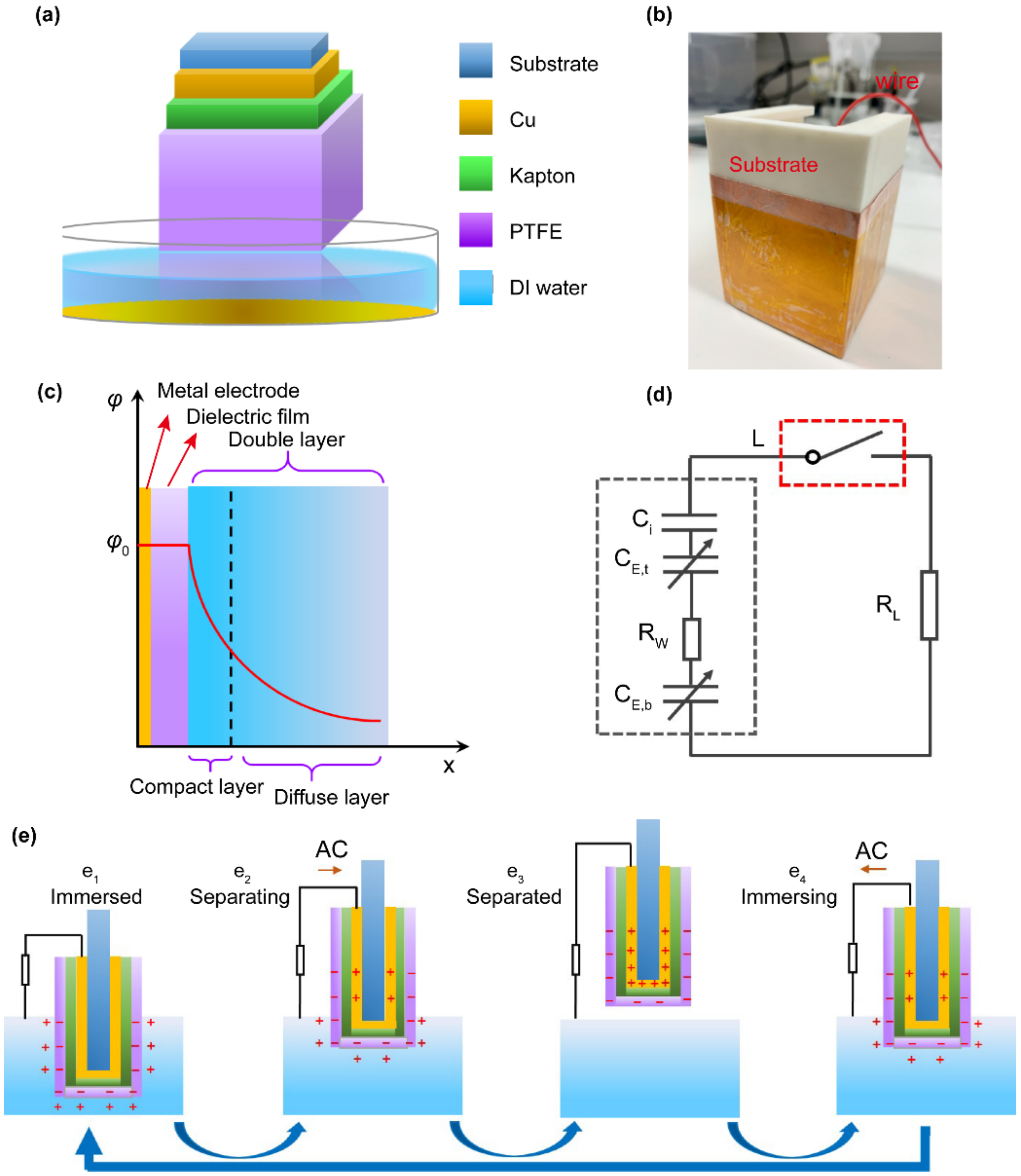

Figure 4.1. (a) Schematic diagram of the water-solid triboelectric nanogenerator and (b) photograph of the moving part setup. (c) Typical electrical double layer formed on the water-dielectric interface area and the relevant variation of electrostatic potential (φ) with distance x from the electrode. (d) The full equivalent circuit model of the water-solid triboelectric nanogenerator. (e) Step-by-step illustration showing the working principle of the water-solid triboelectric nanogenerator.

The basic outputs of the water−solid mode TENG are illustrated in **Figure 4.2**. The peak V_{OC} shown in **Figure 4.2a** is approximately 375 V, which is more than twice the V_{OC} reported in ref 12 and also is several orders of magnitude larger than that of the droplet device designed by Moon et al. [115] It is apparent that the peak Q_{SC} (**Figure 4.2b**) is as high as 160 nC. In the case of the droplet device, its outputs are usually limited by the capillary length of the water bridge formed between the contact surfaces or the interfacial effects. [138] Moreover, it has been proved that the electrical performance of a general solid-solid mode TENG is strongly affected by a group of factors, such as the device configuration, structure parameters, operation conditions, etc. [139; 140] These conclusions are also applicable to the liquid-solid mode TENGs. As illustrated in **Figure 4.2c**, the V_{OC} of the water-solid mode TENG is greatly enhanced when the multidielectric layer is utilized; but similar results cannot be achieved by the utilization of either the Kapton tape or the PTFE film. This is attributed to the larger effective thickness of the multidielectric layer (d_0), that is, increasing the d_0 results in a bigger V_{OC}. Note that the hydrophobic material PTFE leads to a higher output voltage primarily because of its high charge generation capability. [141]

The results presented in **Figures 4.2d−f** show that increasing the contact area improves the V_{OC} and Q_{SC}, which can be proved quantitatively using eqs 8 and 9. For instance, either increasing the L or the $x_{(t)}$ in eq 8 generates a larger V_{OC}. Apart from the contact area, the improvement of the relative velocity can enhance the basic outputs as well (**Figures 4.2g, h**). Assume that the moving part is driven with a typical sinusoidal motion and that the $x_{(t)}$ is described in the model via: $x_{(t)} = x_{max}/2/(1 - \cos \omega t)$, where x_{max} and ω represent the largest relative movement and angular frequency, respectively. It is easily found that the V_{OC} (and Q_{SC}) are functions of the velocity. A larger velocity results in a larger moving distance, and then the contact area at the water-PTFE interface is increased at the same time, so that many more charges are transported between the two electrodes. It should be clear, however, that the surface charge density at the water-PTFE interface is approximately 10 μC/m^2, which is significantly lower than that for the EDL (50 mC/m^2) reported by Wu et al.[59] In other words, although the formation of negative charge is observed on the hydrophobic surface in our experiment, the number of charges participating in transport is smaller than the available charges at the EDL. Hence, extracting more charges from the EDL to participate in the transport in the external circuit should be the focus of attention on in the next step of the work. **Figure 4.2f** presents a comparison of the V_{OC} densities reported in recent years, from which it is seen that the V_{OC} density of this work exhibits the largest value. [142-146]

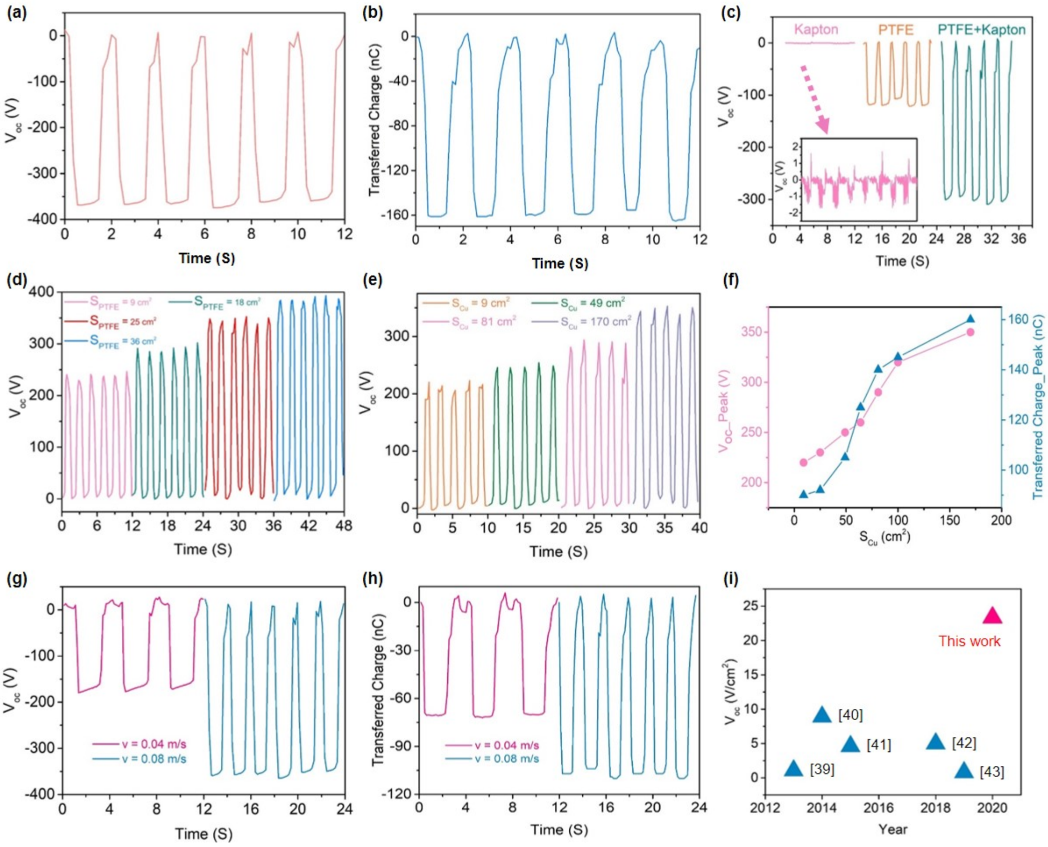

Figure 4.2. (a) Open-circuit voltage (V_{OC}) and (b) short-circuit transferred charges (Q_{SC}) of the water-solid triboelectric nanogenerator when the areas of the PTFE and Cu are 25 cm^2 and 170 cm^2, respectively. Comparison of the V_{OC} for different (c) material selections, (d) sizes of PTFE, (e) sizes of the bottom electrode. (f) Extracted peaks of V_{OC} and Q_{SC} for different sizes of the bottom electrode. Basic outputs of the (g) V_{OC} and (h) Q_{SC} for different velocities of the moving part. (i) Comparison of the open-circuit voltage densities reported in recent years. Note that the V_{OC} of this work exhibits the largest value.

4.3.2 single-wire TENG and three dimensional TENG array

Using the advantages of the water-solid mode TENG, a single-wire geometric structure device was designed. As demonstrated in **Figure 4.3a**, a single Cu wire with a diameter of 2 mm was utilized as one electrode. When the moving part constructed from the Cu wire and the multidielectric layer moves up and down in the DI water in a tube, leading to the generation of conduction current in the external circuit. Since there is no substrate, this method reduces the size and weight of the TENG, and thus improves the system's volume utilization. Although only very little DI water is stored in the tube, excellent outputs are observed in **Figures 4.3b, c**. As the immersion depth (represented by h) becomes gradually larger from 2 to 14 cm, the V_{OC} and Q_{SC} increase simultaneously, owing to the increase in the contact area between the water and the PTFE surface. Furthermore, there is nearly a linear relationship between the V_{OC} (and Q_{SC}) and the immersion depth (**Figure 4.3d**), and the similar phenomena can be found from the corresponding density of V_{OC} and Q_{SC} (**Figure 4.4**), from which a type of self-powered displacement sensor could be fabricated and applied in practical applications. It should be noticed that the depth of DI water is fixed closely to 14 cm in above-mentioned tests. Interestingly, we can observe the same phenomenon when the depth of DI water changing from 2 to 14 cm, as demonstrated in **Figure 4.3e** and **Figure 4.5**. As proved before, it is mainly because increasing the contact area contributes to the transport of more charges in the external circuit. Developing a set of experimental systems for dynamic measurements based on a special displacement sensor should be investigated in future studies. In particular, we have further noted that when the DI water moved only an extraordinarily small distance, a highly visible signal was obtained in the experiment, implying favorable precision and sensitivity of the device.

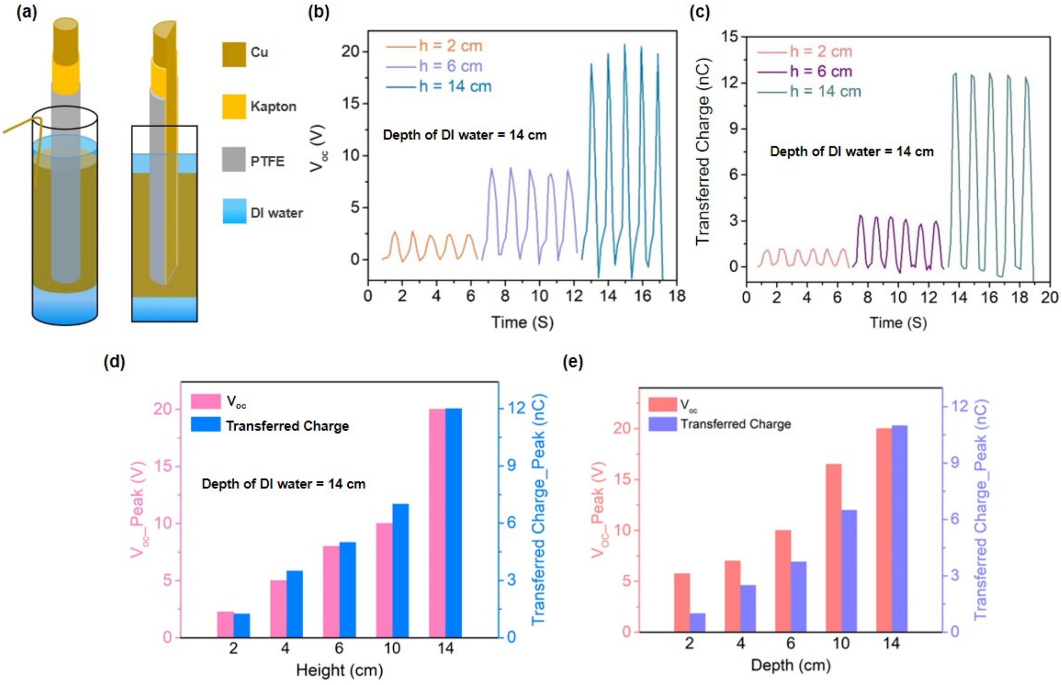

Figure 4.3. (a) Schematic diagram of the single-wire TENG. Comparison of the (b) V_{OC} and (c) Q_{SC} of the single-wire TENG with increasing immersion length, and (d) corresponding extracted peaks of V_{OC} and Q_{SC}; Note that the depth of DI water is fixed at 14 cm. (e) Extracted peaks of V_{OC} and Q_{SC} at different depths of the DI water.

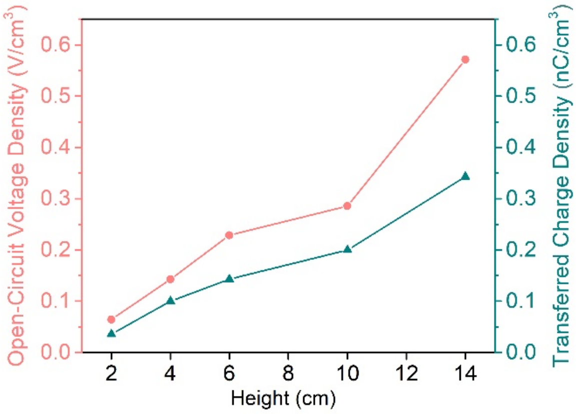

Figure 4.4. Open-circuit voltage density and transferred charge density of the single-wire TENG at different immersion length, with water depth fixed at 14 cm.

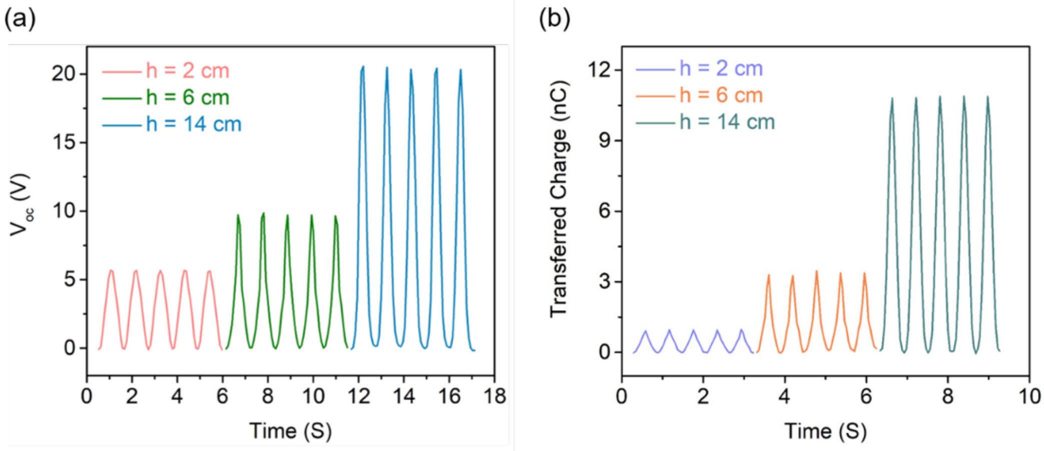

Figure 4.5. Comparison of the (a) open-circuit voltage V_{OC} and the (b) short-circuit transferred charge Q_{SC} of the single-wire TENG with increasing water depth.

Furthermore, a three-dimensional water-solid TENG array comprising many single-wire TENGs was fabricated, which can be utilized as an energy harvester to convert mechanical energy from micro to macro levels, or a self-powered sensor to detect static and dynamic processes through the voltage or current signals. As illustrated in **Figure 4.6a**, a large number of single-wire TENGs are connected in parallel to construct the three-dimensional TENG array. Its equivalent circuit model is proposed in **Figure 4.6b**, where the single-wire TENG is designated by the letter G. We note that although the basic output of the TENG array is approximately proportional to the number of single wires (**Figures 4.6c,e**), which is very obvious from the extracted peaks of V_{OC} and Q_{SC} (**Figures 4.6d,f**), it is almost impossible to obtain a very exact association between the number of wires and basic outputs due to the nonlinear variation of the total capacitance of this TENG energy harvesting system. But it suggests that the single-wire TENG exhibits a high scalability for constructing a TENG array, and offers the possibility of integrating and directly powering various functional sensors. On the other hand, due to the easily deformed nature of water, the TENG array system is flexible enough to absorb and convert every water movement while accommodating each small vibration from external mechanical triggering. For the better understanding of the TENG operation, optical photos and videos of the single-wire TENG and the three-dimensional TENG array are provided to show the behavior of water movement and the TENG in energy harvesting situation (**Figures 4.7 and 4.8**). Briefly speaking, connecting many single-wire TENGs together can effectively improve the electrical output.

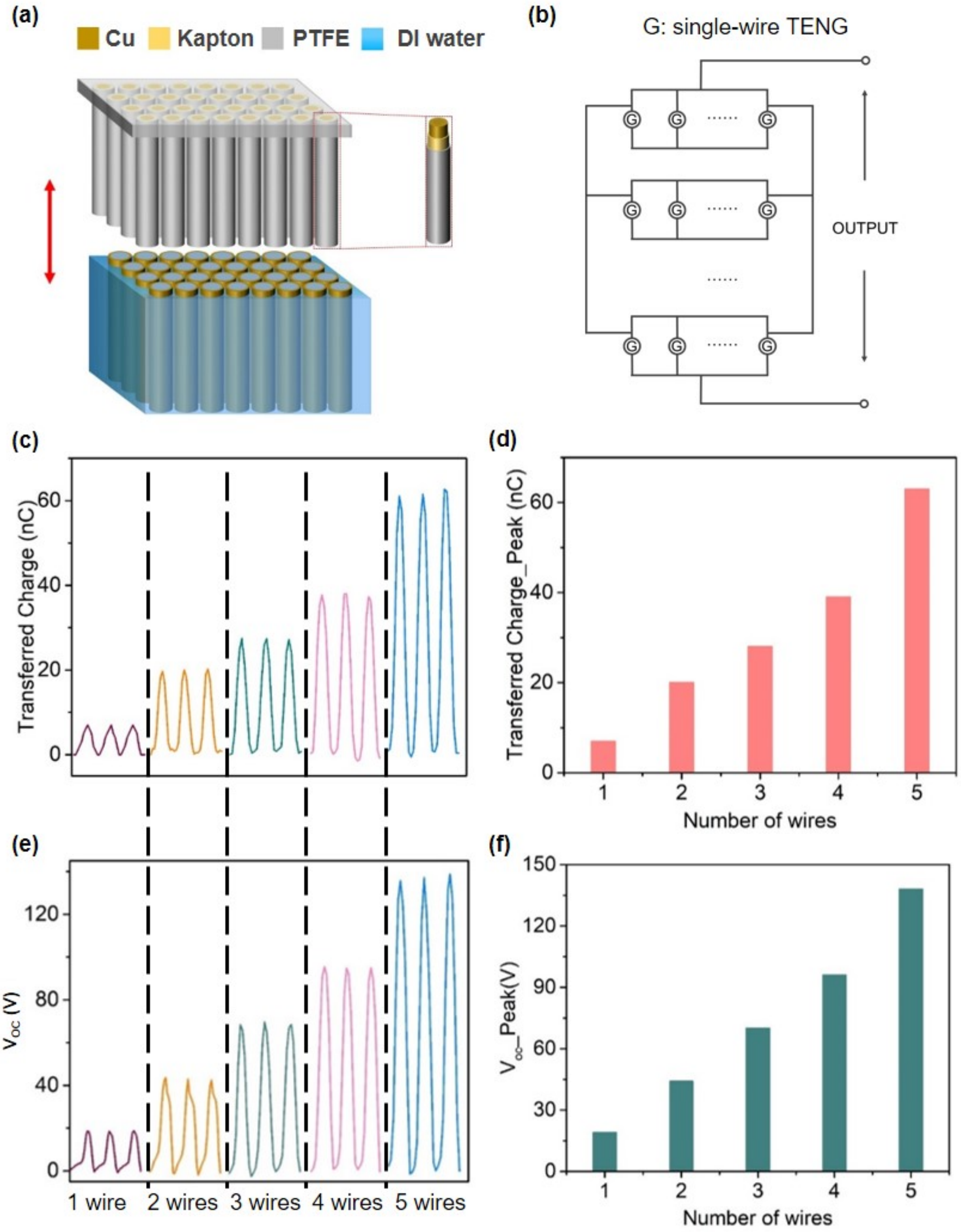

Figure 4.6. (a) Schematic diagram of the three-dimensional water-solid TENG array, constructed from many single-wire TENGs. (b) The equivalent circuit model of the TENG array. (c-d) Transferred charges Q_{SC} and the extracted peaks of Q_{SC} enhancement with the increase of the integrated wire number. (e-f) Open circuit voltage V_{OC} and the extracted peaks of V_{OC} with the increase of the integrated wire number.

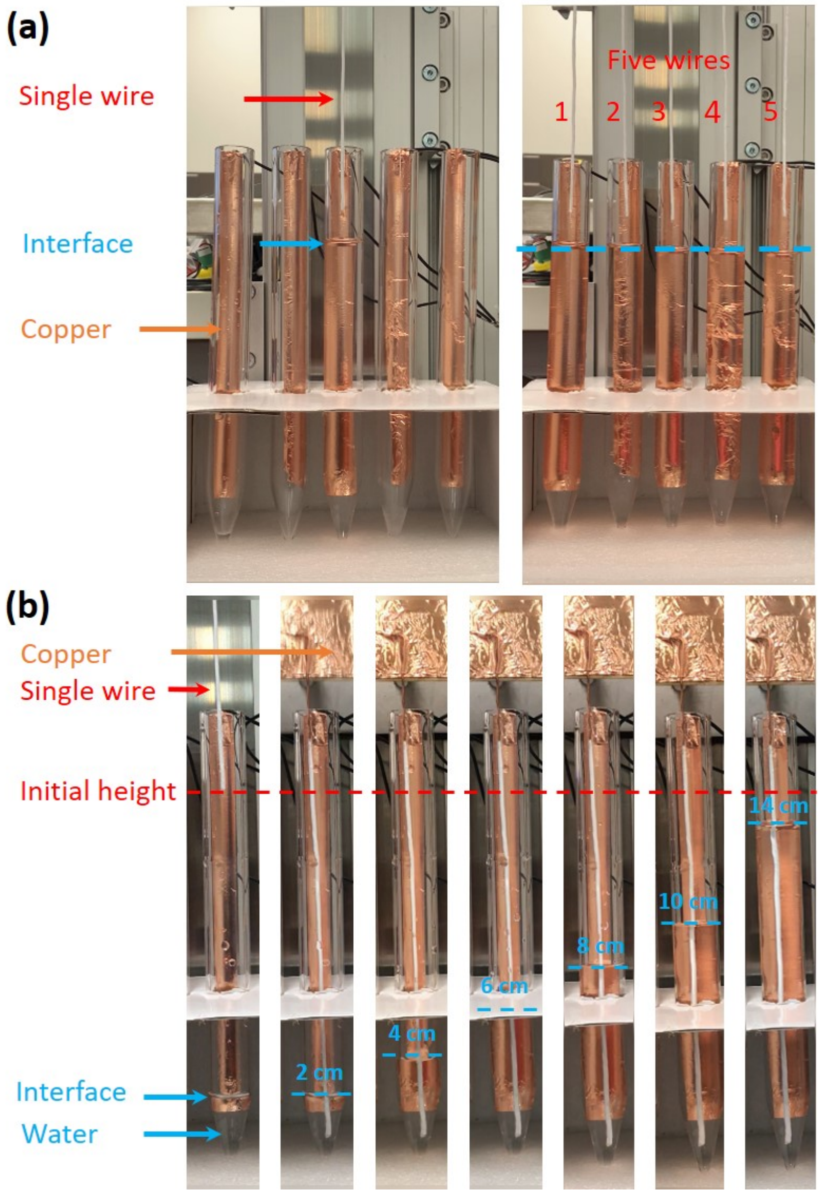

Figure 4.7. (a) Optical images of a single-wire TENG (left) and a TENG array with five single-wire TENG units (right). (b) Optical images of the single-wire TENG with increasing water depth from 2 cm to 14 cm.

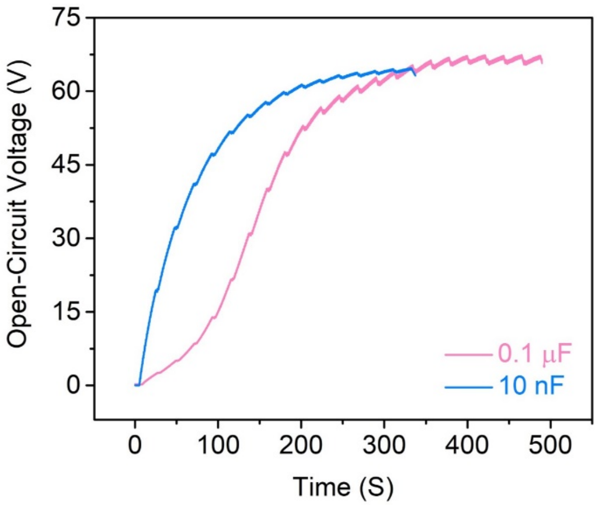

Figure 4.8. Both the rectified outputs of the single-wire TENG are used to charge commercial capacitors of 10 nF and 0.1 μF, respectively.

4.4 Conclusion

In summary, an equivalent circuit model of a water-solid mode TENG is proposed, which allow us to have a better understanding about the physical mechanism of this typical energy harvesting device. First, it was found that EDLs and EDLCs are formed on the water-solid interfaces, which includes the water-PTFE interface and the water-electrode interface. Then a full equivalent circuit model of the water-solid mode TENG is built by a series connection of the two EDLCs and the water resistor, according to the lumped-circuit theory. The EDLC is essentially a nonlinear capacitor with voltage-dependent capacitance, making it arduous to analytically solve the TENG's governing equation, but it is still an attractive option for us to quantitatively predict the energy harvesting process. Furthermore, the influences of structure parameters and operation conditions on the electrical response have been investigated directly, by which the relevant physical mechanism behind them are in depth discussed. The results suggest that selecting suitable materials, increasing the contact area, and increasing the velocity are beneficial to improve the basic output. On the other hand, a three-dimensional water-solid TENG array comprising many single-wire TENGs was designed. This special TENG array can not only convert the tiny mechanical energy from water movement in random directions into electricity, but also could be connected into a network structure for harvesting large-scale energy due to its high scalability, which would further verify our theoretical analysis. We expect that our equivalent circuit model and physical image of the water-solid mode TENG are equally applicable to a general liquid-solid mode TENG, although their rationality and practicality need to be confirmed in future work.

Chapter 5. Power generation based on electrostatic induction

5.1 Abstract

Using the principles of contact electrification and electrostatic induction, triboelectric nanogenerators (TENGs) have the unique capability to convert physical movement into usable electrical power. This feature places TENGs at the forefront of innovative energy solutions. Currently, a diverse range of TENG designs have been developed and studied. However, specific designs that predominantly utilize electrostatic induction have not been extensively explored, highlighting a potential gap in our understanding. In this study, we introduce and delve deeper into TENGs constructed with copper rings and a specially charged ball (or sphere). The central objective is to better understand the nuances and performance of TENGs that rely heavily on the electrostatic induction process. Two primary scenarios were investigated: one where the sphere is positively charged and the other where it's negatively charged. By doing so, we aimed to dissect their energy output characteristics and identify the fundamental factors that influence their performance. The insights garnered from our research not only contribute to a deeper understanding of TENG operations but also have practical implications. They can guide the future design of TENGs, especially those with more intricate structures. Furthermore, recognizing the broader applications of such devices could catalyze their adoption in a variety of fields, thereby advancing sustainable energy solutions.

5.2 Introduction

Triboelectric nanogenerators (TENGs) have made significant strides in the world of energy conversion[125; 147-152], primarily due to their reliance on the interplay between contact electrification (CE) and electrostatic induction. This innovative technology not only demonstrates the possibilities within the realm of energy conversion but also places TENGs firmly within the broader spectrum of mechanical energy harvesters[59; 101; 128; 153-155].

Historically, TENGs have been characterized into five primary modes[4; 5]. These are the vertical contact, single-electrode, lateral sliding, freestanding, and rolling modes. Each of these modes presents a unique architectural design and offers distinct energy output characteristics, catering to various applications and needs. Such diversity in design ensures that TENGs can be tailored for specific functions and environments, enhancing their adaptability and utility. The foundational principle behind the operation of TENGs is Maxwell's displacement current[156-160]. By harnessing this principle, TENGs demonstrate an uncanny ability to efficiently transform mechanical forces, such as motion or pressure[149; 161-163], directly into electrical energy. This transformative capability has opened doors to a myriad of applications that touch our daily lives[164-168]. From self-powered sensors that require no external energy sources to wearable technology that draws power from our movements, and even devices that can harvest the energy from falling raindrops, the possibilities seem endless[167; 169]. Despite the extensive research and numerous configurations of TENGs that have been proposed and studied, a particular area remains somewhat in the shadows. While many TENG designs synergistically utilize both CE and electrostatic induction, TENGs operating primarily or solely on the principles of electrostatic induction are less well-understood. This area of study, which could unlock even further potential and understanding, has not been given its due attention, signifying a promising avenue for future research.

Here, inspired by the principles behind Lord Kelvin’s electrostatic water dropper[170-173], we've crafted a TENG design that integrates a copper ring with a charged dielectric sphere, as depicted in **Fig. 5.1**. The core mechanism revolves around the passage of charged spheres through the copper ring, resulting in the induction of opposite electrical charges on the ring. Delving into this foundational induction concept[174-178], we've probed two distinct operational modes: one where positively charged dielectric spheres traverse the copper ring and another with negatively charged spheres. Our examination covered crucial attributes like the potential, current, and charge retained by the copper. This comprehensive analysis sheds light on the electrification dynamics of this non-contact TENG design. What's fascinating is that despite the seemingly uncomplicated design, the induction experiments have unveiled numerous intriguing outcomes. A notable observation, for example, is how the surface charge polarity on the dielectric spheres appears to govern the induced charge polarity on the copper ring. With these induction experiments complemented by theoretical scrutiny, our aim is to offer insights that define the output traits of TENGs, especially those primarily driven by electrostatic induction. This understanding holds promise for characterizing even the most intricate non-contact TENG devices with specific induced charge patterns.

We aim to delve deeply into the workings of non-contact mode triboelectric nanogenerators (TENGs) that exhibit intricate spatial charge distributions. By understanding the mechanics behind these non-contact mode TENGs, our objective is to pave the way for designs that harness mechanical energy most effectively.

Such TENGs have the potential to be more efficient, dependable, and cost-friendly, capturing energy from diverse sources like human movements, ambient wind, and vibrations to fuel electronic devices. Ultimately, our findings seek to propel advancements in sustainable energy collection, emphasizing the potential of both contact and non-contact model TENGs.

5.3 Electrical performance and mechanisms of the non-contact TENG unit

In our examination of the non-contact copper-ring TENG, as depicted in **Fig. 6.1**, its design hinges on two primary components: a charged dielectric sphere and a copper ring. The dynamics of this system become apparent when the charged dielectric sphere, which serves as the moving part, interacts with the copper ring. The interaction manifests through the induction and consequent distribution of electric charges on the copper ring's surface.

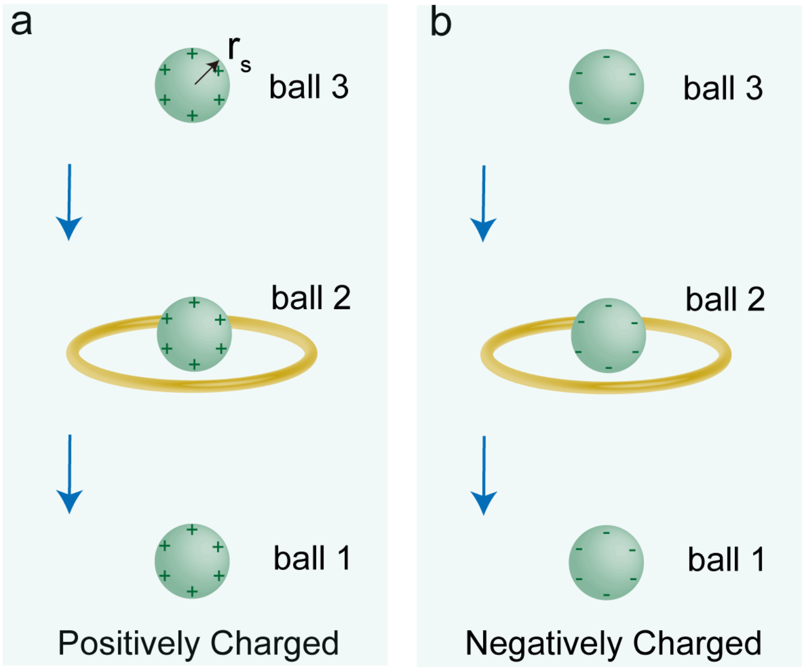

Figure 5.1. Experimental schematic of the copper ring-based power generation unit.

Starting with the behavior induced by charged spheres, we systematically investigated the outcomes for both positively and negatively charged spheres, as displayed in **Figs. 6.2** and **6.3**. A noteworthy observation is the distinct generation of a positive electric potential signal within the ring when a positively charged sphere navigates through it. This occurrence stands as clear evidence of the ring accommodating induced positive charges. An especially significant revelation is the magnitude of the induction effect. As seen in **Fig. 6.2b, c, and d**, measurements of electric potential, current, and surface charge reach their peak when the charged dielectric sphere is precisely aligned with the copper ring's center. This suggests that the spatial relationship between the sphere and the ring plays a crucial role in the efficiency of charge induction. Further scrutiny of **Fig. 6.2** reveals a consistent induction pattern. The emergence of three distinct peaks consecutively when three positively charged spheres pass through the copper ring implies a one-to-one relationship. Each sphere's transit is directly responsible for generating a singular, distinct peak. These findings not only provide clarity on the fundamental workings of the non-contact copper-ring TENG but also highlight the conditions optimizing its efficiency. Both the sphere's position relative to the copper ring and its charge type significantly influence the induction outcomes.

The behavior we observe is rooted in the principles of electrostatic induction[4; 119; 179-181]. At its core, electrostatic induction is a mechanism where the electric charge distribution of one material shifts due to the proximity of other charged objects. For instance, when we introduce a positively charged dielectric sphere to the vicinity of the copper ring, as shown in **Fig. 6.1**, it pulls the copper ring's negative charges towards itself while simultaneously pushing away the ring's positive charges. This action results in a rearrangement of charges within the copper ring, leading to the results: negative charges accumulate closer to the sphere (inside the ring), and positive charges position themselves away from the sphere (outside the ring).

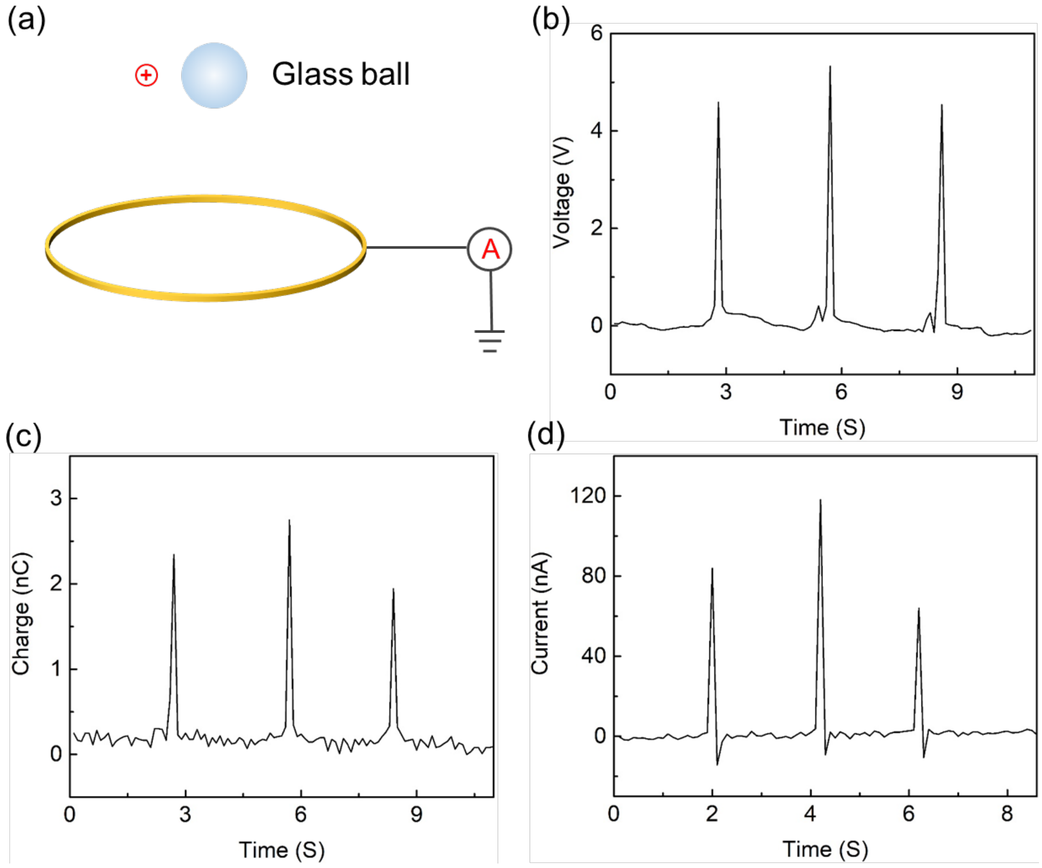

Figure 5.2. Electrical performance when positive charged spheres pass through a copper ring. Radius of the charged sphere is 0.5 cm. Radius of the copper ring is 1.5 cm.

Turning our attention to the interactions involving a negatively charged sphere, we observe a marked contrast from the earlier results. Specifically, as shown in **Figure 6.3**, when a negatively charged sphere passes through the copper ring, it induces a negative electric signal. This demonstrates a direct correlation between the polarity of the charge on the dielectric sphere and the subsequent electrical response within the copper ring. A more granular exploration into the spatial positioning unveils further intricacies. The electric potential and surface charge density reach their peak when the negatively charged dielectric sphere is precisely aligned with the center of the copper ring, as detailed in **Fig. 6.3b, 6.3c and 6.3d**. Such observations accentuate the pivotal role of the sphere's position in relation to the copper ring in determining the optimal induction effects. Consistent with the behavior elucidated in **Fig. 6.3**, a clear and repeatable pattern emerges. As three negatively charged spheres sequentially pass through the copper ring, the data indicates the formation of three distinct peaks. This continuous yet discrete induction pattern underscores a one-to-one relationship: each sphere's journey through the copper ring results in a singular and identifiable peak.

From the data collected, a comprehensive interpretation can be derived by grounding our understanding in foundational electrostatic principles, specifically the mechanism of electrostatic induction[176; 182-185]. This phenomenon encapsulates the redistribution of electric charges within a material when exposed to external charged bodies. To elucidate, when introducing a negatively charged dielectric sphere to the proximity of a copper ring, an intricate charge interaction ensues. The sphere's negative charges exert an attractive force on the ring's positive charges, concurrently exerting a repulsive force on its negative counterparts. This dynamic induces a transient charge redistribution within the copper matrix. This perturbed state persists as long as the charged sphere remains in close proximity. However, upon increasing the separation between the entities, the copper swiftly reverts to its electro-neutral equilibrium. This rapid neutralization can be attributed to the inherent thermal agitation of atomic constituents, facilitating the reintegration of charges. This sequence of electrostatic interactions culminates in pronounced peaks in both electric potential and induced surface charge.

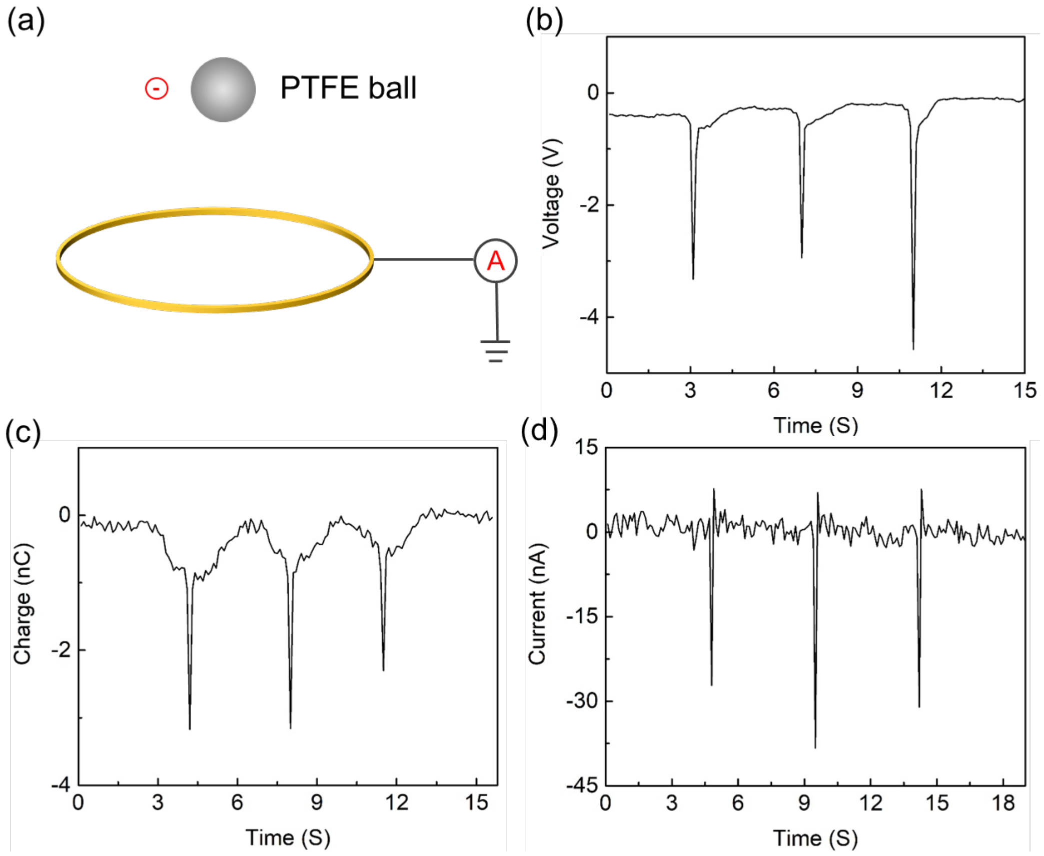

Figure 5.3. Electrical performance when a negative charged sphere pass through a copper ring. Radius of the charged sphere is 0.5 cm. Radius of the copper ring is 1.5 cm.

5.4 Conclusion

In summarizing our research, we find it essential to revisit the guiding force behind our work: Lord Kelvin's water-drop electrostatic generator. From it, we designed non-contact TENGs, focusing on the charged dielectric sphere-copper ring configuration. Our goal was straightforward: capture mechanical energy using only electrostatic induction. We examined both positively and negatively charged models. Despite the apparent simplicity of the non-contact copper ring model TENG, it revealed crucial information. This model, even in its basic form, helped us understand TENGs that solely rely on electrostatic induction. Revisiting our initial discussions, the potential of TENGs in energy conversion is clear. They offer practical solutions for everyday energy needs. Our research adds depth to the understanding of non-contact TENGs, especially those with detailed charge distributions. It's these insights that we believe will guide better TENG designs in the future, ensuring efficient energy capture from various mechanical sources. In conclusion, our work offers a clearer picture of non-contact TENGs and their workings. We hope that our findings will influence future research and design, pushing TENG technology forward.

Chapter 6. Simulation model of a non-contact triboelectric nanogenerator

6.1 Abstract

Based on the coupling effects of contact electrification and electrostatic induction, a triboelectric nanogenerator (TENG) can convert mechanical energy into electric power, which is at the cutting edge of alternative energy technology. Although a considerable number of TENGs with different configurations have been designed, some of them however, which only depend on the electrostatic induction effect have not received enough attention. Here, a non-contact TENG model consists of copper rings and charged dielectric sphere is presented, which is aimed at exploring the working process of TENGs caused by electrostatic induction. Two classical models, including vertical and horizontal double copper rings models are also proposed. Relevant advanced and accurate models of TENGs have been established through the finite element method. We anticipate that the constructed model and theoretical analysis are helpful for the design of non-contact model TENGs with complicated geometric construction, and expand their applications in various fields.

6.2 Introduction

Based on the coupling effects of contact electrification (CE) and electrostatic induction [9; 27; 39; 186], triboelectric nanogenerators (TENGs) have been fabricated and demonstrated as a cutting-edge technology in the field of energy conversion [93; 112; 187-191], which belongs to the class of mechanical energy harvesters [59; 192-197]. To date, five basic modes of TENGs have been designed, which are: vertical contact mode, single-electrode mode, lateral sliding mode, freestanding mode, and rolling mode[55]. Each mode has its own respective structure and output characteristics. Using Maxwell's displacement current as the driving force,[134; 156; 198; 199] a TENG device can effectively convert mechanical energy into electricity, giving TENGs many potential applications in our daily life, such as self-powered sensors, wearable electronics, raindrop energy collectors, etc. [200-207] A considerable number of TENGs with different configurations have been designed,[208; 209] but most of them are operated according to the coupling effects of CE and electrostatic induction. Very few investigations have been carried out, however, for elucidating the working mechanism of TENGs that depend on electrostatic induction alone. In other words, this is an aspect that has not received enough attention in the past.

Zuankai Wang's group (2020) have developed a droplet-based electricity generator (DEG) to harvest energy from impinging water droplets, based on the effect of contact electrification and electrostatic induction.[171] The DEG utilizes a structure that includes an aluminum electrode and a polytetrafluoroethylene (PTFE) film atop an indium tin oxide (ITO) substrate. As the droplets continuously fall on the device, charges are generated and stored in the PTFE as a result of contact electrification between the water droplets and the fabricated device; while opposite charges are electrostatically induced on the ITO for charge transfer to the aluminum electrode, so a closed-loop electrical system is formed. Dating from 1867, one of the most remarkable and impressive displays of static electricity is an experiment using Lord Kelvin's water-drop electrostatic generator.[170; 172; 173] This classical device uses falling water to generate voltage differences by electrostatic induction occurring between interconnected, oppositely charged systems. The generated voltage keeps growing as the water droplets continue to impinge on the device, which eventually leads to an electric arc discharge in the form of a spark. This is a typical example of how electric power can be generated just through electrostatic induction. It should be noted that its simple construction makes this device popular in physics education as a laboratory experiment for students, which has been a big inspiration for us to design a special TENG device.

Here, inspired by Lord Kelvin's electrostatic water dropper, a copper-ring-model TENG has been designed, which consists of a charged dielectric sphere and two copper rings (**Fig. 6.1a**). As a charged sphere passes through the center of the copper rings, opposite electrical charges are induced in the copper rings. Using this classical induction phenomenon, two types of models of TENGs have been constructed: a vertical double copper ring (metal electrode) model (VDR) and a horizontal double copper ring model (HDR). We have elaborated how the key parameters such as the radius of charged sphere and copper ring as well as the distances between the rings, etc., affect the basic output performance. Most importantly, the finite element method (FEM) through COMSOL software was utilized to simulate the whole energy harvesting system based on the TENGs. Despite the simple geometry of these structures, many interesting and surprising findings have been observed from the advanced simulations. For instance, some results indicate that the relative positions of the double copper rings sensitively influence the electric potentials of each ring. As the vertical distance between the two copper rings increases, the peak of electric potential begins to divide itself into two; but the two divided peaks are equal to each other. Through the established FEM models and the corresponding quantitative analysis, we expect to see these explorations help to characterize the output characteristics of TENGs, the operation of which only depends on the electrostatic induction, even when a non-contact model TENG device has an extremely complex and specific induced charge distribution.

Our research aims to provide significant insights into the operation of non-contact model triboelectric nanogenerators (TENGs) with a complex and spatially induced charge distribution. By gaining insights into the working mechanism of non-contact model TENGs, we can contribute to achieving optimal designs and applications of TENGs for efficient mechanical energy harvesting. The non-contact model TENGs could be more efficient, reliable, and cost-effective, allowing them to harness mechanical energy from various sources, including human motion, wind, and vibration, to power electronic devices. Overall, this research may provide reference information to drive the growth of sustainable energy harvesting technologies through not only by contact model TENGs but also by non-contact model TENGs.

6.3 Finite element method simulation of non-contact triboelectric nanogenerator models

As demonstrated in **Fig. 6.1a**, a non-contact copper-ring model TENG consists of two parts: a charged dielectric sphere and two copper rings. As the charged dielectric sphere (moving part) passes through a copper ring, electric charges are induced and distributed on the surface of the copper ring. In particular, when the charged dielectric sphere is passed through the center of the copper ring, the largest electric potential and surface charge density are observed (**Fig. 6.1c and d**). A series of experiments have been carried out to validate the simulation results, and the experimental schematic is demonstrated in **Fig. 6.1b**. We have found that there is a good agreement between the experimental and simulation results. As illustrated in **Figs. 6.1e and 6.1f**, three peaks are continuously produced when three positively charged spheres are passing through the copper ring. That is, it generates one peak at a time. Since the simulation model is proposed based on certain assumptions, such as assuming that the copper rings are perfect conductors and neglecting some small effects that may occur in the experimental setup, there are some differences between the experimental and simulation results, which does not influence the accuracy of our conclusions.

It should be noticed that two opposite induced charge signals are obtained in **Fig. 6.1g and Fig. 6.4** when a positive charged sphere is passing through the copper ring. This seemingly paradoxical results can be explained through the effect of electrostatic induction. Electrostatic induction is a physical process, which leads to a redistribution of electric charge on one material under the influence of one or more nearby objects that have electric charge. When the positively charged dielectric sphere is brought near a copper ring (metal conductor, in **Fig. 6.1a**), the positive charges start attracting the negative charges of the copper ring. Additionally, the positive charges repel the positive charges within the copper ring. This then creates a relocation of electrical charges within the metallic ring. That is why the induced negative charges and positive charges are located in and out of the copper ring, respectively (**Fig. 6.1g**). Need to be reminded that in order to focus our attention to the influence of electrostatic induction, the copper ring in our theoretical simulation model is no grounding. On the contrary, if the copper ring is grounded, only the opposite charges can be generated on the inside of the copper ring, because the like charges on the outside have been flowed into the ground at this condition. Therefore, there is a positive charge signal is observed in **Fig. 6.1f**. And in the experiments, the radii of the charged sphere (r_s), and copper ring (r_c) are 0.5 cm and 1.5 cm, respectively.

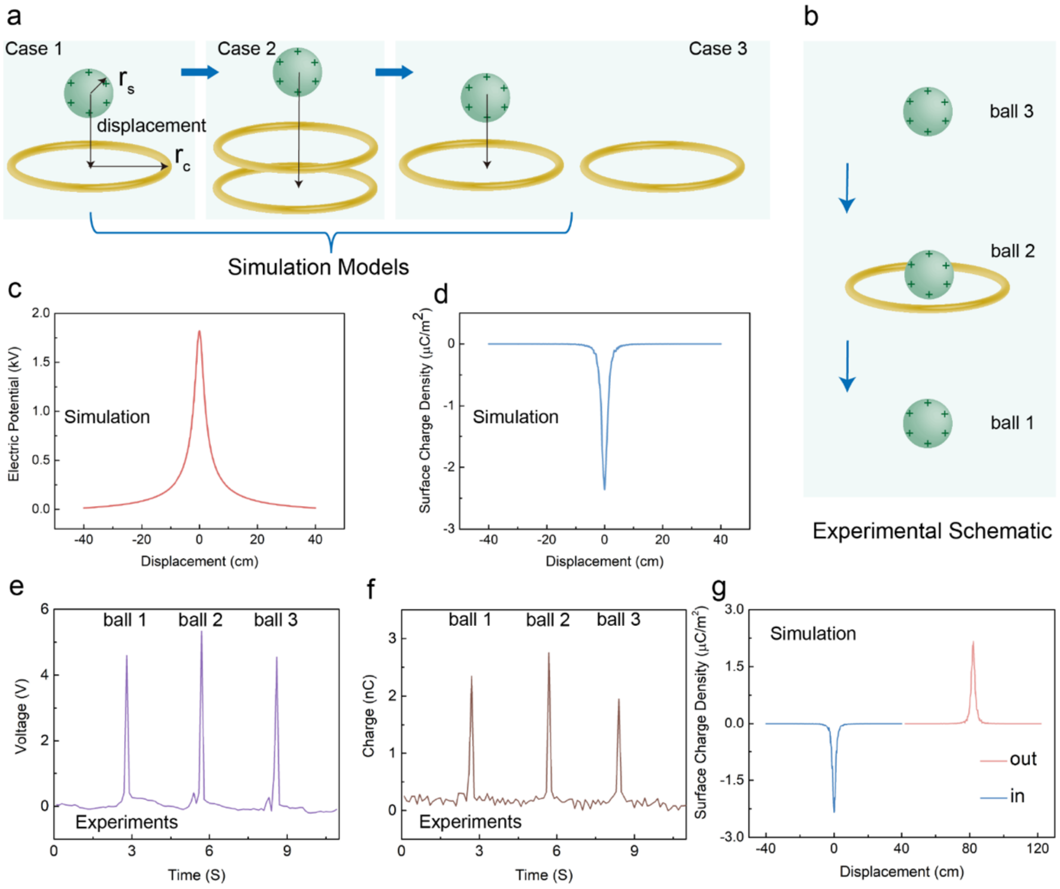

Figure 6.1. Schematic diagram showing the finite-element structure model, experimental schematic, and the comparison between the simulation results and experiments results. (a) Simulation model of charged sphere passing through a single copper ring, double vertical copper rings and double horizontal copper rings, respectively. (b) Experimental schematic of charged sphere passing through a single copper ring. The simulated (c, d) and experimental (e, f) electric potential and surface charge density of a single copper ring when a charged sphere passes through it (radius of charged sphere, r_s = 0.5 cm; radius of copper ring, r_c = 1.5 cm). (g) Surface charge density of inside and outside the copper ring when a positive charged sphere passed through.

More simulations were performed to investigate what are the key influences and how these influences affect the electric potential and induced charge density. Firstly, the influences of positively and negatively charged spheres were studied (**Figs. 6.2a and 6.2b**). It is observed that a positive electric potential signal is generated in the copper ring when a positively charged sphere passes through it, demonstrating the distribution of induced positive charges on the copper ring. In contrast, a negatively charged sphere passing through the copper ring results in a negative electric signal. The corresponding distributions of electric potential simulated by the FEM model are demonstrated in **Fig. 6.2g and Fig. 6.2h**. It is well known that the geometry of the TENG structure exerts a strong influence on the basic outputs. Here, we are first focusing on the radii of the charged sphere and the copper ring. **Figure 6.2c** reveals that there is a sharp rise of the electric potential when r_s is increased to 1.0 cm, while there is a marked drop as r_s is decreased to 0.5 cm. What can be clearly observed in **Figure 6.2e** is that the peak of the electric potential is proportional to the ratio of r_s/r_c. The electric potential peak reaches -7.28 kV when r_s/r_c is equal to 0.667, and it falls to -67 V as r_s/r_c decreases to 0.067. A similar phenomenon is shown in **Fig. 6.2d and 6.2f**, where the peak of the induced surface charge density is proportional to the ratio of r_s/r_c as well. The simulation results depicted in **Fig. 6.2f** show that the induced surface charge density peak grows to -10.157 μC/m^2 when r_s/r_c is 0.667, and it drops to -0.086 μC/m^2 as r_s/r_c decreases to 0.067.

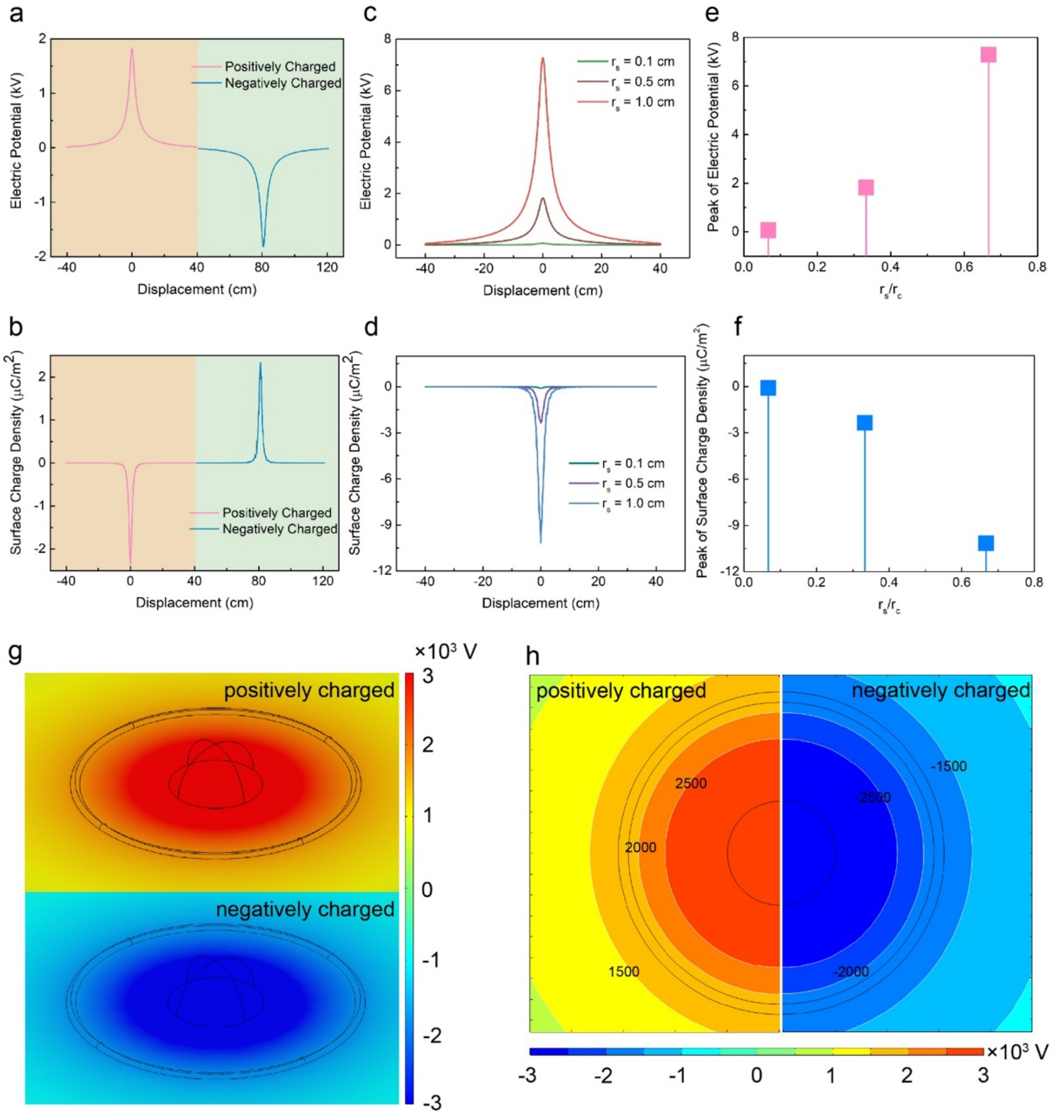

Figure 6.2. Basic simulation results for charged sphere passing through a single copper ring. (a) Electric potential and (b) surface charge density of the copper ring when a charged sphere passes through. (c) – (f) Electric potential and surface charge density of the copper ring when charged spheres with different radii pass through the charged sphere (the radius of the charged sphere, r_s = 0.1 cm, 0.5 cm, and 1.0 cm, while the radius of the copper ring, r_c = 1.5 cm). (g) Distribution of electric potential (*V*) and (*h*) its contours when the sphere is positively charged and negatively charged separately.

We then changed the radius of copper ring r_c to validate the above findings.

Figure 6.3a and 6.3b illustrates how the variation of r_c affects the electric potential and surface charge density of the copper ring, respectively. As the r_c increases from 0.6 cm to 3.0 cm, the electric potential of the copper ring decreases from 4.619 kV to 0.884 kV (**Figure 6.3a**), and the surface charge density exhibits a similar downward trend, which decreases from -15.117 μC/m^2 to -0.566 μC/m^2 (**Figure 6.3b**). The electric potential contours calculated for different radii of the copper ring are illustrated in **Figure 6.3e**. These results further validate what is shown in **Figure 6.2e and 6.2f**. When the radius of the charged sphere is close to that of the copper ring (**Figure 6.3e1**), we can obtain a large electric potential and induced surface charge density in the copper ring. On the contrary, the reverse trend is seen if there is a bigger r_c (**Figure 6.3e3**). In addition, if the r_s and r_c remain constant but the surface charge density of the charged sphere varies, we can get some really interesting findings. The results presented in **Figure 6.3c and 6.3d** show that the electric potential and induced surface charge density are proportional to the surface charge density ρ_s of the charged sphere. When the ρ_s becomes gradually larger, from 1 μC/m^2 to 50 μC/m^2, the electric potential of the copper ring is increased from 0.182 kV to 9.103 kV (Fig. 3c and 3d); while the relevant induced surface charge density of the copper ring rises from 0.226 μC/m^2 to 11.318 μC/m^2. Note that, since there is only one copper ring, this special structure can be regarded as a single mode TENG. So, we can reach the general conclusion that the basic output performance of this single mode TENG is strongly linked to the surface charge density of the charged sphere.

Table 6.1. Parameters utilized in the numerical calculations for the single-copper-ring mode TENG.

Model component	Parameter utilized

r_s	0.1 – 1.0 cm
r_c	0.6 – 3.0 cm
Surface charge density, ρ_s	1 – 50 μC/m^2
Maximum falling height, z_{max}	40 cm

The above results are easily to understand and can be interpreted through electrostatics and the phenomenon of electrostatic induction. This electrostatic influence is a redistribution of electric charge on one material under the influence of one or more nearby objects that have electric charge. The charged object acts through its electric field even to more distant bodies, thus changing their original non-electrical state. For instance, when a negatively charged dielectric sphere (charged object) is brought near a copper ring (metal conductor), the negative charges start attracting the positive charges of the copper ring. Additionally, the negative charges repel the negative charges within the copper ring. This then creates a relocation of electrical charges within the metallic ring. The electrical charges will remain in the redistributed state as long as the charged dielectric sphere is kept near the copper ring. When the charged sphere starts moving away, however, the metallic ring loses its charge instantaneously, which is because of the thermal motion of the atoms, which causes the charges to integrate again. Finally, an electric potential peak and induced surface charge peak are created.

Furthermore, when either the radius of the charged sphere or that of the copper ring (or both) increases/decreases, it will change the distance between them, changing the electric field intensity, which affects the charge redistribution of the copper ring. It should also be clear that the electric potential of the copper ring is determined by the special charge distributions both in the sphere and copper ring. In our simulations, the copper ring is never grounded, so the electrically charged sphere can induce equal and opposite charges in the copper ring (**see the Figure 6.4**). When the charged sphere is either close to or far away from the copper ring, it does not receive or transfer any electrons from/to the copper ring (or metal electrode) by electrical induction., However, if the copper ring is grounded, charges opposite in polarity will become attracted according to the electrostatics; in other words, the copper ring will display the charge that is opposite to the inducing charge.

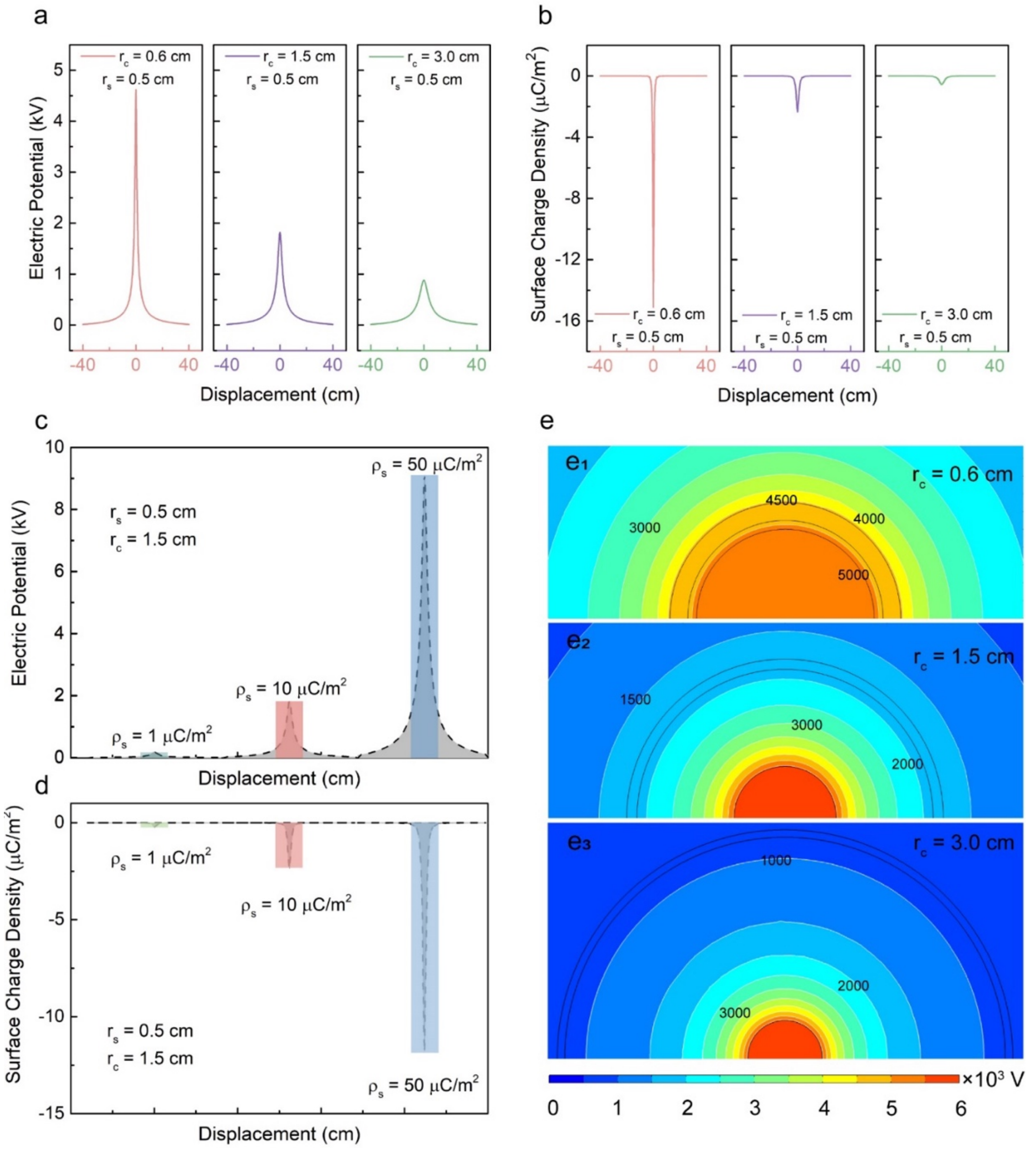

Figure 6.3. Simulation results for a charged sphere passing through single copper ring. (a) Electric potential and (b) surface charge density of the copper ring when a

charged sphere passes through single copper rings with different radii (r_s = 0.5 cm, r_c = 0.6 cm, 1.5 cm, and 3.0 cm). (c) Electric potential and (d) surface charge density of the copper ring when charged spheres pass through with different charge densities (r_s = 0.5 cm, r_c = 1.5 cm, ρ_s = 1 μC/m^2, 10 μC/m^2, and 50 μC/m^2). (e) Contours of electric potential (V) when charged spheres (ρ_s = 10 μC/m2, r_s = 0.5 cm) pass through single copper rings with different radii (r_c = 0.6 cm, 1.5 cm, and 3.0 cm).

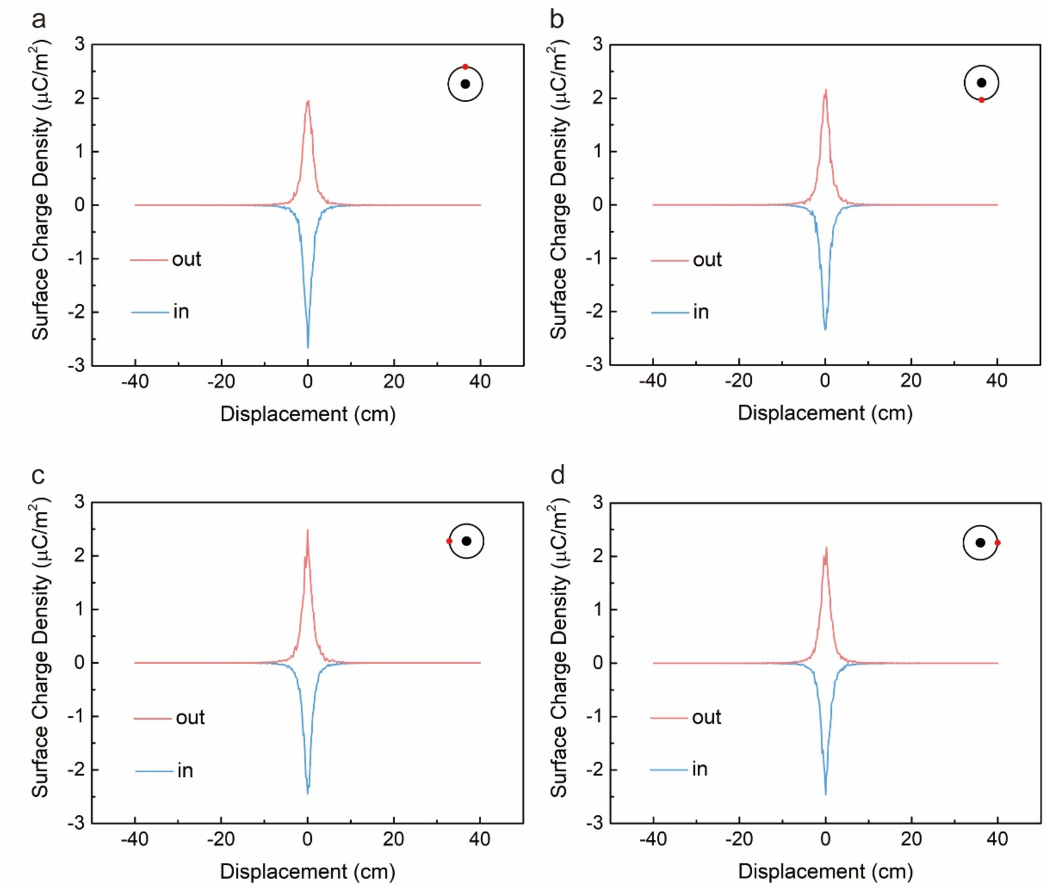

Figure 6.4. Surface charge density for different positions of the copper ring in the single copper ring model.

In addition, a vertical double copper ring model (VDR) was introduced to further investigate the variation of the output characteristic of a TENG based on electrostatic induction and to provide a thorough understanding of the charge distribution (**Fig. 6.1a**). The VDR TENG model consists of a charged dielectric sphere (moving part, $r_s = 0.5$ cm) and double copper rings with the same radius ($r_c = 1.5$ cm). The double copper rings are vertically oriented and centered on the same y axis. As the charged dielectric sphere passes through the two copper rings successively, electric charges are induced and distributed on the surfaces of both of the copper rings. We have investigated the influence of geometrical parameters in the single copper ring model, such as the radius of the charged sphere and copper ring, here we are focusing on the vertical distance between the vertical double copper rings. Under open circuit (OC) conditions, no charges are transferred between the two copper rings, and consequently, only induced electric charges are distributed on the surfaces of the copper rings, so the electric potential difference between the double copper rings is presented. Under short-circuit (SC) conditions, free charges flow in the double copper rings to reduce the potential difference, so the transferred charged density of the double copper rings is presented. The electric potential difference at OC condition and the transferred charge density at SC condition between double copper rings with different vertical separations (heights) are presented in **Fig 6.5a**. It can be easily observed that the open circuit voltage and transferred charge density are proportional to the vertical distance, illustrating that the relative distance sensitively affects the output performance of the VDR TENG model. Several other intriguing findings have been found also, such as the fact that the surface charge density varies significantly among the various positions of the copper ring (**Fig. 6.5b and Fig. 6.5c**). The surface charge density at the two points of the vertical double copper rings has a similar value but a different trend while they are operating under OC conditions. On the other hand, the surface charge density of both points shows the same trend but a different value when the vertical double copper rings are under SC conditions. The above mentioned phenomena are attributed to the symmetrical structure of the double copper rings. When the charged dielectric sphere passes through the center of the copper ring, it induces equal and opposite charges on both sides of the copper ring due to the symmetry. Note that because the double copper rings whether at OC or SC conditions are not grounded, the similar surface charge density can be obtained. In theory, the surface charge densities at any point in the copper rings should be same at SC conditions, since it must keep the same electrical potential of the two copper rings. However, the copper rings have no grounding in our simulations, which make the free charges distributed in these rings cannot flow freely, thus generating a non-uniform surface charge density. But what is certain is that the total charges stay the same. This is the reason why there are different peak shapes of the up and down in **Fig. 6.1c**.

Fig. 6.5d presents the electric potential of both copper rings under SC conditions. The electric potential of each copper ring in the VDR model drops with increasing vertical separation. The peak electric potential of double copper rings at 0.5 cm in height is 1.787 kV, which is comparable to the basic output of the single copper ring model (1.82 kV). The peak value only reaches 0.949 kV when the height is 20 cm. Another finding is that when the vertical separation is large enough (in this case, 3 cm), the peak of the electric potential is divided into two, and the two newly formed peaks are equal to one another while maintaining symmetry. This phenomenon indicates that as the vertical separation increases, the effect of induced electrification caused by one copper ring enhances gradually, which generates peak one by one when the charged sphere passing through.

Table 6.2. Parameters utilized in the numerical calculations for the vertical double-

copper-ring mode TENG.

Model component	Parameter utilized
r_s	0.5 cm
r_c	1.5 cm
Surface charge density, ρ_s	10 μC/m^2
Maximum falling height, z_{max}	40 cm
Vertical height between double copper rings, h	0.1 – 1.0 cm

When the charged dielectric sphere approaches the open-circuited double copper rings, the free electrons in the ring experience a static electric force and move to the area farther away from the charged sphere, leading to the creation of induced charges on the ring. These induced charges create an electric field and induce an electric potential. The magnitude of the induced potential depends on the distribution and variation of the electric field. When the charged sphere passes through the copper rings vertically, the induced charges concentrate at the top and bottom of the vertical double copper ring model, creating an electric potential and inducing an electric current on the ring. As the vertical separation increases, the electric field lines generated by the two copper rings become more diffused, and the total strength of the electric field decreases, either, which generates a lower electric potential. Most importantly, when the vertical separation increases to some extent (h = 5 cm), the time difference through the copper ring plays an increasingly important role, thus generating peaks one by one and each corresponding to the induction effect of a single copper ring. *So*, this is in fact a revelation to us that an appropriate architecture is strongly important for a non-contact model TENG. **Fig. 6.5e** demonstrates the three-dimensional distributions of electric potential and electric field (arrows) when the charged dielectric sphere is passing through the center of the copper rings. The electric potential contours calculated at different vertical distances of the double copper rings are described in **Fig. 6.5f**, which directly depicts the effect of the vertical separation of the rings on the output performance of the VDR model.

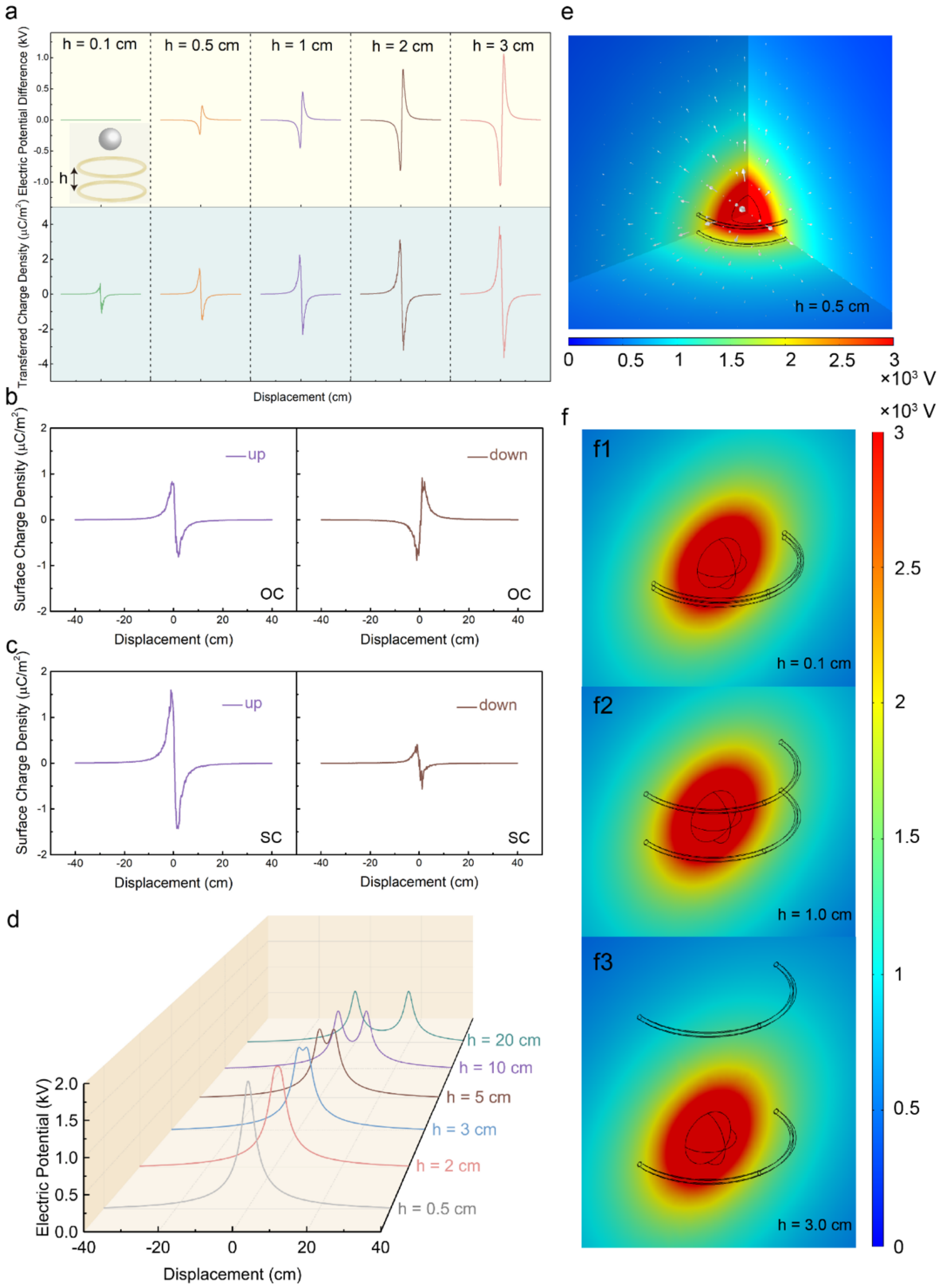

Figure 6.5. Simulation results for a charged sphere passing through vertical double copper rings (ρ_s = 10 μC/m^2, r_s = 0.5 cm, with the radius of the double vertical copper rings the same, r_c = 1.5 cm). (a) Electric potential difference (in the open-circuit condition) and transferred charge density (in the short-circuit condition) between double vertical copper rings when a charged sphere pass through at different heights of the top ring (where the height between the double vertical copper rings, h = 0.1 cm, 0.5 cm, 1 cm, 2 cm, and 3 cm). Surface charge density of different positions on the copper ring under (b) open-circuit (OC) conditions and (c) short-circuit (SC) conditions. (d) Electric potential of vertical double rings in the OC condition when h changes (h = 0.5 cm, 2 cm, 3 cm, 5 cm, 10 cm, and 20 cm). (e) three-Dimensional distribution of electric potential (indicated by colors) and electric field (indicated by arrows) when a charged sphere pass through the double vertical copper rings separated by 0.5 cm. (f) Distribution of electric potential under OC conditions when h changes (h = 0.1 cm, 1.0 cm, and 3.0 cm).

Moreover, the VDR model was converted to an offset double-copper-ring model (with horizontal as well as vertical separation of the centers of the rings) to validate the above findings. A schematic illustration of a charged sphere passing through the offset double rings model is presented in **Fig. 6.5c** with its key parameters attached. Here, the horizontal distance s between the centers of double copper rings is treated as the most important factor in the model, and the investigation covered the situations where both double copper rings were at OC condition and where they were at SC condition. The electric potential difference between the double copper rings in the OC condition is shown in detail according to the variation of s in **Fig. 6.5a**. It can be clearly seen that the electric potential difference grows with s, and what is also interestingly found is that two electric potential peaks are first created, and then they merge into a single peak as the horizontal distance between the centers of the copper rings varies from 0.8 cm to 2.2 cm. The same phenomenon is also exhibited for the peak of transferred charge density at SC condition (**Fig. 6.6b**). **Fig. 6.6e** shows slices of the electric potential distribution when the charged dielectric sphere is at the center of the lower copper ring (with the double copper rings at OC condition), which validates the above results again. A three-dimensional electric potential distribution of the offset double-copper-ring model at SC condition is given in **Fig. 6.6d**, with the arrows representing the electric field and the charged sphere at the center of the lower copper ring at a distance s of 0.5 cm. Note that we fixed the radius of the charged sphere r_s, the radius of both copper rings r_c, the surface charge density of the sphere, and the vertical height between the double copper rings h at 0.5 cm, 1.5 cm, 10 $\mu C/m^2$, and 0.5 cm, respectively, in the offset double copper rings model.

Table 6.3. Parameters utilized in the numerical calculations for the horizontal double-copper-ring mode TENG.

Model component	Parameter utilized
r_s	0.5 cm
r_c	1.5 cm
Surface charge density, ρ_s	10 $\mu C/m^2$
Maximum falling height, z_{max}	40 cm
Horizontal distance between double copper rings, s	0.1 ~ 1.0 cm

Whether the two created peaks merged into one single peak for the offset double-copper-ring model, or the one single peak derived into two equal and symmetry peaks of the vertical double copper ring model, the essential reason of generating above two phenomena is the same, both of which are caused by electrostatic induction. When the positions of the two copper rings are strongly close to each other, the induced charges can be created at about the same time, giving rise to the generation of one electric potential peak (**Fig. 6.5**). For the offset double-copper-ring model, if the distance *s* is small enough, such as when it is equal to 0.2 cm, the charged sphere can pass through the two copper rings instantaneously and simultaneously. That is why two peaks of electric potential and surface charge density has been observed; in other words, the geometry structure of the VDR model is similar to that of the offset double-copper-ring model. However, as the distance of *s* increases until it is sufficiently large (for instance, s = 2.2 cm), two copper rings (partitions) cannot interfere with each other (**Fig. 6.7**). As a result, the charged sphere just passes one copper ring each time, and only one single peak is observed. On the other hand, through the positions of the two electric potential or transferred charges peaks, one can design and fabricate a special kind of position sensors to detect the moving objects in practice.

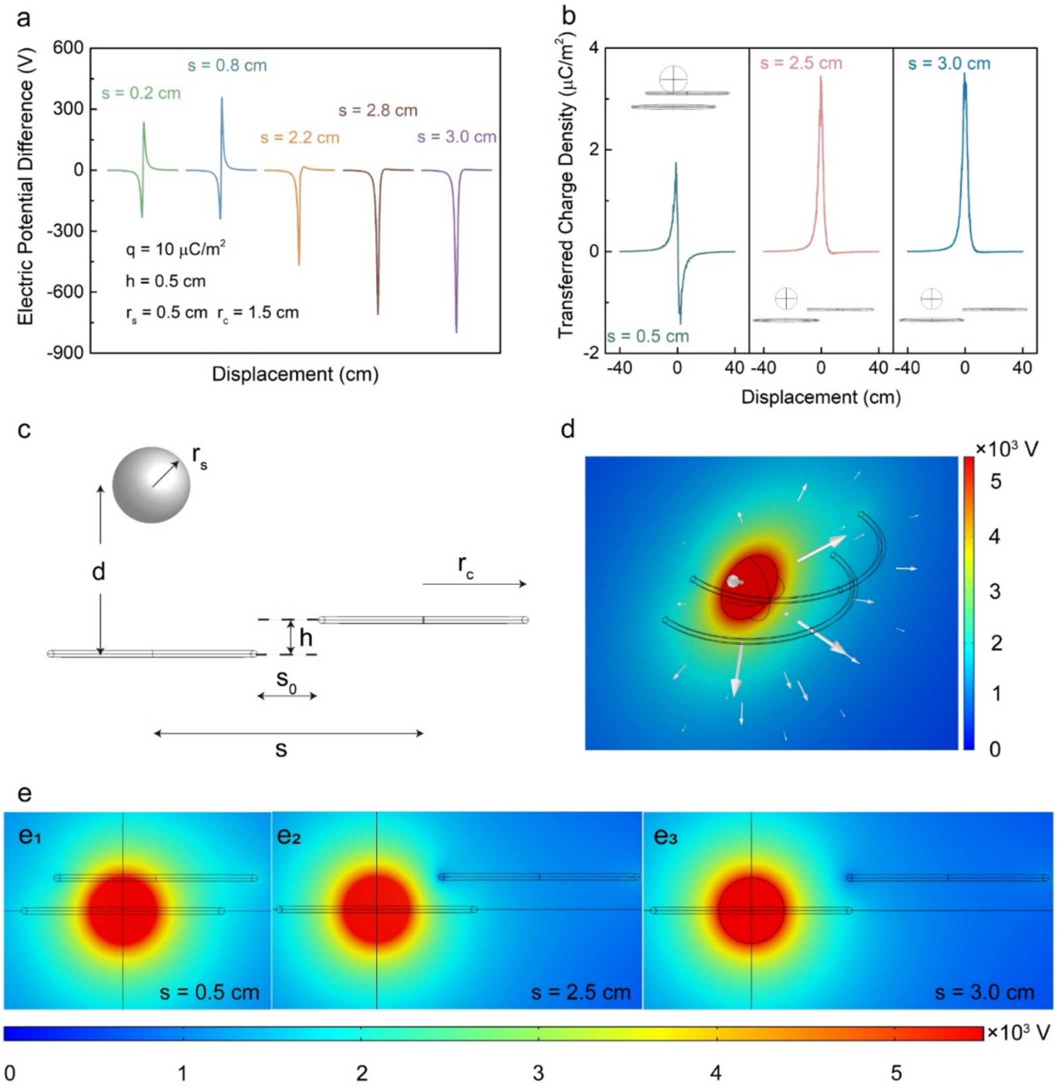

Figure 6.6. Simulation results for a charged sphere passing through offset double copper rings ($\rho_s = 10$ μC/m^2, $r_s = 0.5$ cm, with the radii of the double vertical copper rings the same, $r_c = 1.5$ cm). (a) Electric potential difference between double offset copper rings in the OC condition when the charged sphere passes through at different horizontal offsets s ($s = 0.2$ cm, 0.8 cm, 2.2 cm, 2.8 cm, and 3.0 cm). (b) Transferred charge density between double offset copper rings in the SC condition when s changes ($s = 0.5$ cm, 2.5 cm, and 3.0 cm). (c) Structure of charged sphere passing through double copper rings and relevant parameters. The variables in the structure are defined as follows: r_s represents the radius of the charged dielectric sphere, r_c represents the radius of both copper rings, d represents the displacement

of the sphere, h represents the vertical height between the double copper rings, S_0 represents the minimum horizontal distance between the double copper rings, and S represents the horizontal distance between the center of the double copper rings. (d) 3-Dimensional distribution of electric potential (colors) and electric field (arrows) when the charged sphere passes through the offset vertical copper rings horizontal offset of 0.5 cm. (e) Distribution of electric potential in the OC conditions when s changes (s = 0.5 cm, 2.5 cm, and 3.0 cm).

Finally, the HDR model was constructed to illustrate whether interaction effects occur between the two copper rings. Two copper rings are placed on the same horizontal plane, while the charged dielectric sphere passes through the left copper ring only. Here, the key factor is the minimum distance S_0 between the horizontal double copper rings (**Fig. 6.6c**), and the output performance of the HDR models were investigated under both OC and SC conditions. Under OC conditions, it can be clearly seen from **Fig. 6.9a** that the open circuit voltage between the double copper rings increases proportionally with S_0. **Fig. 6.9b** presents the electric potential of both the horizontal copper rings in detail, respectively (outputs of different distances are presented in **Fig. 6.7-6.8**). It should be noted that the electric potential of the left copper ring that charged dielectric sphere passes through is constant at 1820 V, which is same as the output in the single-copper-ring model. Since the distance between the charged sphere and the left copper ring remains constant, there is no variation of the electric field intensity, which means that the charge redistribution of the left copper ring remains constant. The variation of the horizontal distance S_0 affects the charges redistribution of the right copper ring, thus affecting the open circuit voltage between double copper rings.

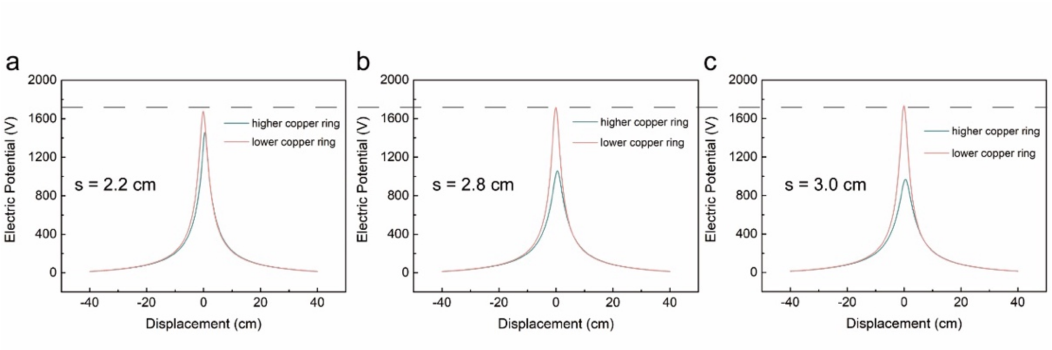

Figure 6.7. Electric potentials of both copper rings in the OC condition in the crossed double copper rings model, with varying horizontal distance *s* between the double copper rings.

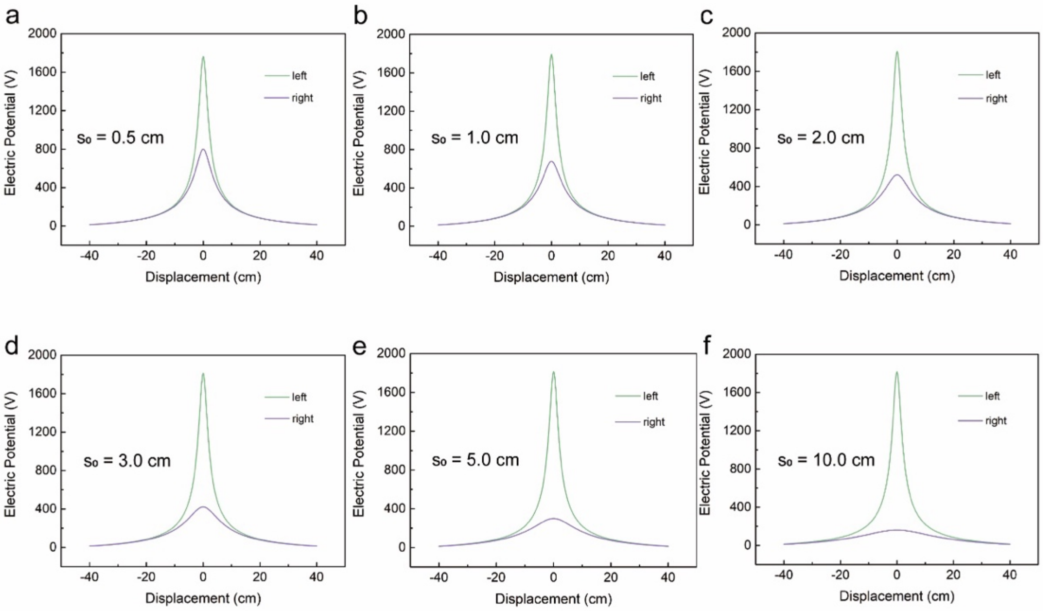

Figure 6.8. Electric potentials of both copper rings in the OC condition in the horizontal double copper ring model, where the minimum distance S_0 between double copper rings varied from 0.5 cm to 10 cm.

Although there is no charge transfer between the copper rings when they are under OC conditions, the surface charge densities of both copper rings (**Fig. 6.9c**) at the minimum distance S_0 of 0.5 cm are different with each other. We find that the surface charge density of the left copper ring where the charged sphere passes through is obviously larger than that of the right copper ring, which is mainly because the left copper ring is closer to the charged body. To keep the process of electrostatic equilibrium, large number of charges are induced rapidly in this copper ring, resulting a higher peak than that of the right copper ring. The contours of the double copper rings under OC conditions when S_0 is changed are depicted in **Fig. 6.9f**, which obviously demonstrates the variation of electric potential when S_0 is varied from 0.5 cm to 3.0 cm. The output performance was also simulated for the situation where the double horizontal copper rings are under SC conditions, and the results were compared with those under OC conditions at the distance S_0 of 0.5 cm. The surface charge density of the left copper ring that the charged sphere passes through is given in **Fig. 6.9d** under both OC and SC conditions. The electric potentials under both conditions are compared in **Fig. 6.9e** with the arrows representing the electric field. From the above findings, we can reach the general conclusion that the relative distances and positions of the double copper rings extraordinarily affect the basic output performances of HDR TENG models. The detailed reason about why these phenomena has been happened were mentioned above.

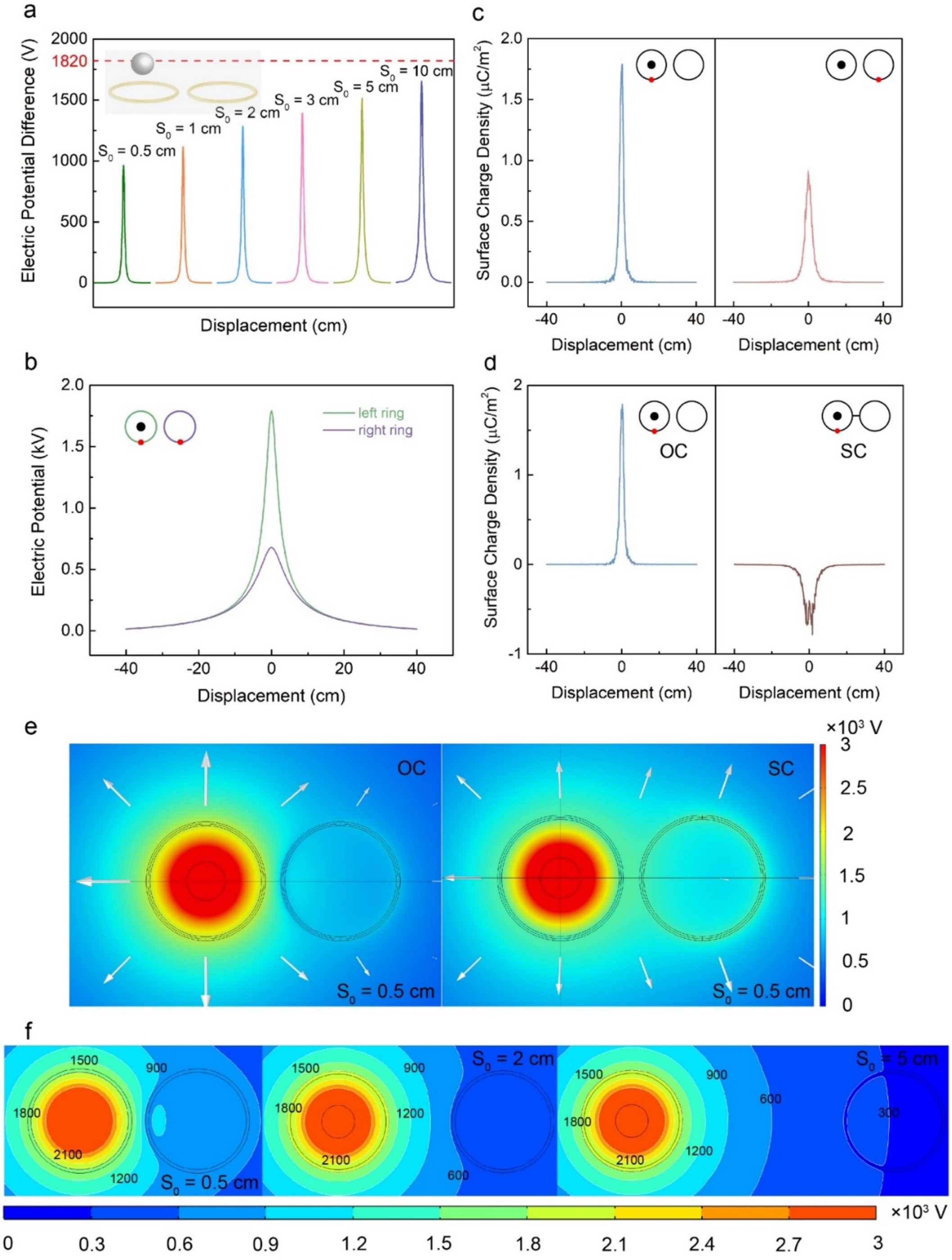

Figure 6.9. Simulation results of charged sphere passing through horizontal double copper rings ($\rho_s = 10\ \mu C/m^2$, $r_s = 0.5$ cm, the radii of the double horizontal copper rings are the same, $r_c = 1.5$ cm). (a) Electric potential difference between double horizontal copper rings when the closest distance between the double horizontal copper rings S0 changes ($S_0 = 0.5$ cm, 1 cm, 2 cm, 3 cm, 5 cm, and 10 cm). (b)

Electric potential and (c) surface charge density of both horizontal copper rings under OC conditions when S_0 = 0.5 cm. (d) Surface charge density comparison when the horizontal double copper rings are under OC and SC conditions. (e) Distribution of electric potential (colors) and electric field (arrows) when the charged sphere passes through the double horizontal copper rings. (f) Contours of the electric potential (V) under OC conditions when the distance between the double horizontal copper rings S_0 changes (S_0 = 0.5 cm, 2 cm, and 5 cm).

6.4 Conclusion

Inspired by Lord Kelvin's water-drop electrostatic generator, non-contact copper ring TENGs, including vertical and horizontal models are developed in this work, which are intended to harvest mechanical energy only through the effect of electrostatic induction. By using COMSOL, the large finite element method software package, we have explained how different key parameters, such as the size of the charged sphere and copper ring, the surface charge density, and the relative positions of the copper rings, affect and control the basic output performance of TENGs. It was observed that the electric potential and induced surface charge density are proportional to the radius of the charged sphere, and interestingly they are inversely proportional to the radius of copper ring. What needs to be emphasized is that the electric potential and transferred charges of the designed TENGs are powerfully influenced by the relative positions of these copper rings.

In the case of the vertical double copper ring (VDR) model TENG, its open circuit voltage is proportional to the vertical distance between the two copper rings. Under short circuit conditions, however, the electric potential of each copper ring decreases with increasing vertical spacing. When the vertical spacing was large enough (for instance, 3 cm in this work), the peak of the electric potential began to divide itself into two; and the two generated two peaks were equal to each other, always maintaining symmetry. In the case of the horizontal double copper ring (HDR) model TENG, it is interestingly found that the two electric potential peaks are created first, and they then merge into one peak as the distances between the copper rings increases from 0.2 cm to 2.2 cm. The same phenomenon was also exhibited by the peak of the transferred charge density for the HDR model TENG. The non-contact copper ring model TENG is chiefly characterized by the simplicity of its structure, but it could exhibit enough information to describe the basic output characteristics of TENGs that harvests energy just by the electrostatic induction effect alone. This work is likely to provide special insights to understand the working mechanism of non-contact model TENGs with a complex and spatially induced charge distribution, thus contributing to the achievement of optimum designs and applications of TENGs for mechanical energy harvesting.

Chapter 7. Conclusions and Prospects

7.1 Conclusions

In this doctoral work, electrical output performance and working mechanisms of solid-liquid triboelectric nanogenerators are investigated. The major conclusions are as following:

1. An equivalent circuit model of a water-solid mode TENG is proposed, which allow us to have a better understanding about the physical mechanism of this typical energy harvesting device. First, it has been found that EDLs and EDLCs are formed on the water-solid interfaces, which includes the water-PTFE interface and the water-electrode interface. Then a full equivalent circuit model of the water-solid mode TENG is built by a series connection of the two EDLCs and the water resistor, according to the lumped-circuit theory. The EDLC is essentially a nonlinear capacitor with voltage-dependent capacitance, making it arduous to analytically solve the TENG’s governing equation, but it is still an attractive option for us to quantitatively predict the output performances. Furthermore, the influences of structure parameters and operation conditions on the electrical response have been carried out directly, by which the relevant working mechanism behind them are in depth discussed. The results suggest that selecting suitable materials, increasing the contact area, and increasing the velocity are beneficial to improve the basic output. Moreover, a three-dimensional water-solid TENG array comprising many single-wire TENGs was designed. This special TENG array can not only convert the tiny mechanical energy from water movement in random directions into electricity, but also could be connected into a network structure for harvesting large-scale energy due to its high scalability, which would further verify our theoretical analysis.

2. Inspired by the Lord Kelvin's water-drop electrostatic generator, we

developed non-contact copper ring TENGs, encompassing both vertical and horizontal models, in order to harvest mechanical energy exclusively via electrostatic induction. Utilizing the finite element method, we analyzed key determinants like charged sphere and copper ring dimensions, surface charge density, and relative ring positions, on TENG performance. Obviously, electric potential and induced surface charge density are proportionate to the charged sphere's radius, but inversely with the copper ring's radius. One important aspect to note is that the electric potential and charge transfer are substantially determined by the positions of the copper rings. The non-contact copper ring TENG stands out for its structural simplicity, yet it illuminates fundamental characteristics of TENGs that solely harness electrostatic induction, offering insights into the operation of non-contact TENGs and enhancing mechanical energy harvesting designs and applications.

7.2 Prospects

The exploration of solid-liquid TENGs has provided a new paradigm for energy harvesting and diverse applications. The unique characteristics of liquid-based environments, coupled with the advancements in understanding the fundamental principles and charge transfer mechanisms, have paved the way for the development of efficient and versatile liquid-solid TENGs. Although significant progress has been made, there are still challenges to be addressed such as enhancing device efficiency, stability, and scalability.

Despite its potential, interface triboelectricity is still a relatively new and emerging field. As such, there is still much to be discovered and optimized.

The rising demand for sustainable and renewable energy solutions positions TENGs as pivotal contributors, with their scalability and efficiency aligning with these global needs. Key to their advancement is the research focusing on material optimization and design enhancement. The performance of TENGs heavily relies on the material properties, including their triboelectric behavior, electrical conductivity, and mechanical flexibility. Researchers can focus on discovering new materials or engineering existing ones to enhance the performance, stability, and durability of TENG devices. The integration of functional materials, such as piezoelectric or ferroelectric materials, can also enable multifunctional energy harvesting devices.

Additionally, the understanding and controlling of the liquid-solid interface play a critical role in the output performance of TENGs. Future studies can be carried out on interface engineering to improve charge transfer efficiency and reduce energy loss, which includes exploring surface modification techniques, such as surface functionalization, nano structuring, and surface coatings, to enhance the interaction between the liquid and solid surfaces. Furthermore, optimizing the interface configuration and geometry could lead to the enhancement of charge generation and collection, thereby improving the overall performance of TENGs.

Despite significant progress, there is still much to learn about the fundamental mechanisms of governing solid-liquid interface triboelectricity. Researchers can delve deeper into addressing the charge transfer processes, interface phenomena, and energy conversion mechanisms at the molecular and atomic levels. Advanced theoretical modeling, computational simulations, and experimental techniques can be employed to reveal the complex dynamics occurring during contact electrification and electron transfer at the liquid-solid interface.

Bibliography or List of References

1. Furfari, F. A. (2005). A history of the Van de Graaff generator. *IEEE Industry Applications Magazine*, *11*(1), 10-14.

2. Fan, F., Tian, Z., & Wang, Z. L. (2012). Flexible triboelectric generator. *Nano Energy*, *1*(2), 328-334.

3. LináWang, Z. (2014). Triboelectric nanogenerators as new energy technology and self-powered sensors–Principles, problems and perspectives. *Faraday discussions*, *176*, 447-458.

4. Lin, L., Xie, Y., Niu, S., Wang, S., Yang, P.K., & Wang, Z. L. (2015). Robust triboelectric nanogenerator based on rolling electrification and electrostatic induction at an instantaneous energy conversion efficiency of~ 55%. *ACS Nano*, *9*(1), 922-930.

5. Cheng, T., Shao, J., & Wang, Z. L. (2023). Triboelectric nanogenerators. *Nature Reviews Methods Primers*, *3*(1), 39.

6. Helmholtz, H. v. (1853). Ueber einige Gesetze der Vertheilung elektrischer Ströme in körperlichen Leitern, mit Anwendung auf die thierisch-elektrischen Versuche (Schluss.). *Annalen der Physik*, *165*(7), 353-377.

7. Chapman, D. (1913). LI. A contribution to the theory of electrocapillarity. *Lond Edinb Dublin Philos Mag J Sci* 25: 475–481. In.

8. Stern, O. (1924). Theory of a double-electric layer with the consideration of the adsorption processes. *Z. Electrochem*, *30*, 508-516.

9. Wang, Z. L., & Wang, A. C. (2019). On the origin of contact-electrification. *Materials Today*, *30*, 34-51.

10. Gauduel, Y., Pommeret, S., Migus, A., & Antonetti, A. (1990). Some evidence of ultrafast H2O+-water molecule reaction in femtosecond

photoionization of pure liquid water: Influence on geminate pair recombination dynamics. *Chemical physics*, *149*(1-2), 1-10.

11. Loh, Z., Doumy, G., Arnold, C., Kjellsson, L., Southworth, S., Al Haddad, A., Kumagai, Y., Tu, M.-F., Ho, P., & March, A. (2020). Observation of the fastest chemical processes in the radiolysis of water. *Science*, *367*(6474), 179-182.

12. Lin, S., Xu, L., Chi Wang, A., & Wang, Z. L. (2020). Quantifying electron-transfer in liquid-solid contact electrification and the formation of electric double-layer. *Nature Communications*, *11*(1), 399.

13. Nie, J., Ren, Z., Xu, L., Lin, S., Zhan, F., Chen, X., & Wang, Z. L. (2020). Probing contact-electrification-induced electron and ion transfers at a liquid–solid interface. *Advanced Materials*, *32*(2), 1905696.

14. Li, J., & Wang, X. (2017). Research Update: Materials design of implantable nanogenerators for biomechanical energy harvesting. *APL Materials*, *5*(7).

15. Song, C., Zhu, X., Wang, M., Yang, P., Chen, L., Hong, L., & Cui, W. (2022). Recent advances in ocean energy harvesting based on triboelectric nanogenerators. *Sustainable Energy Technologies and Assessments*, *53*, 102767.

16. Guo, X., Liu, L., Zhang, Z., Gao, S., He, T., Shi, Q., & Lee, C. (2021). Technology evolution from micro-scale energy harvesters to nanogenerators. *Journal of Micromechanics and Microengineering*, *31*(9), 093002.

17. Rodrigues, C., Nunes, D., Clemente, D., Mathias, N., Correia, J., Rosa-Santos, P., Taveira-Pinto, F., Morais, T., Pereira, A., & Ventura, J. (2020). Emerging triboelectric nanogenerators for ocean wave energy harvesting: state of the art and future perspectives. *Energy & Environmental Science*, *13*(9), 2657-2683.

18. Tang, J., Liu, T., Miao, S., & Cho, Y. (2021). Emerging energy harvesting

technology for electro/photo-catalytic water splitting application. *Catalysts*, *11*(1), 142.

19. Zhu, J., Zhu, M., Shi, Q., Wen, F., Liu, L., Dong, B., Haroun, A., Yang, Y., Vachon, P., & Guo, X. (2020). Progress in TENG technology—A journey from energy harvesting to nanoenergy and nanosystem. *EcoMat*, *2*(4), e12058.

20. Chung, J., Chung, S.-H., Lin, Z.-H., Jin, Y., Hong, J., & Lee, S. (2021). Dielectric liquid-based self-operating switch triboelectric nanogenerator for current amplification via regulating air breakdown. *Nano Energy*, *88*, 106292.

21. Kim, T., Yong, H., Kim, B., Kim, D., Choi, D., Park, Y. T., & Lee, S. (2018). Energy-loss return gate via liquid dielectric polarization. *Nature Communications*, *9*(1), 1437.

22. Luo, H., Wang, H., Yang, L., Wu, H., Kang, S., Yong, S., Liao, R., Wang, J., & Wang, Z. L. (2022). In situ nanofluid dispersion monitoring by liquid–solid triboelectric nanogenerator based on tuning the structure of the electric double layer. *Advanced Functional Materials*, *32*(27), 2200862.

23. Wang, J., Wu, Z., Pan, L., Gao, R., Zhang, B., Yang, L., Guo, H., Liao, R., & Wang, Z. L. (2019). Direct-current rotary-tubular triboelectric nanogenerators based on liquid-dielectrics contact for sustainable energy harvesting and chemical composition analysis. *ACS Nano*, *13*(2), 2587-2598.

24. Yu, A., Chen, X., Cui, H., Chen, L., Luo, J., Tang, W., Peng, M., Zhang, Y., Zhai, J., & Wang, Z. L. (2016). Self-powered random number generator based on coupled triboelectric and electrostatic induction effects at the liquid–dielectric interface. *ACS Nano*, *10*(12), 11434-11441.

25. You, J., Shao, J., He, Y., Yun, F. F., See, K. W., Wang, Z. L., & Wang, X. (2021). High-Electrification Performance and Mechanism of a Water-Solid Mode

Triboelectric Nanogenerator. *ACS Nano*, *15*(5), 8706-8714.

26. Zhao, J., Wang, D., Zhang, F., Pan, J., Claesson, P., Larsson, R., & Shi, Y. (2022). Self-Powered, Long-Durable, and Highly Selective Oil-Solid Triboelectric Nanogenerator for Energy Harvesting and Intelligent Monitoring. *Nanomicro Lett*, *14*(1), 160.

27. Nie, J., Ren, Z., Xu, L., Lin, S., Zhan, F., Chen, X., & Wang, Z. L. (2020). Probing Contact-Electrification-Induced Electron and Ion Transfers at a Liquid-Solid Interface. *Adv Mater*, *32*(2), e1905696.

28. Lin, S., Xu, L., Chi Wang, A., & Wang, Z. L. (2020). Quantifying electron-transfer in liquid-solid contact electrification and the formation of electric double-layer. *Nat Commun*, *11*(1), 399.

29. Zou, H., Zhang, Y., Guo, L., Wang, P., He, X., Dai, G., Zheng, H., Chen, C., Wang, A. C., Xu, C., & Wang, Z. L. (2019). Quantifying the triboelectric series. *Nat Commun*, *10*(1), 1427.

30. Luo, Q., Xiao, K., Zhang, J., & Sun, W. (2022). Direct-Current Triboelectric Nanogenerators Based on Semiconductor Structure. *ACS Applied Electronic Materials*, *4*(9), 4212-4230.

31. Wang, Z., Zhang, Z., Chen, Y., Gong, L., Dong, S., Zhou, H., Lin, Y., Lv, Y., Liu, G., & Zhang, C. (2022). Achieving an ultrahigh direct-current voltage of 130 V by semiconductor heterojunction power generation based on the tribovoltaic effect. *Energy & Environmental Science*, *15*(6), 2366-2373.

32. Xu, C., Yu, J., Huo, Z., Wang, Y., Sun, Q., & Wang, Z. L. (2023). Pursuing the tribovoltaic effect for direct-current triboelectric nanogenerators. *Energy & Environmental Science*.

33. Lin, S., Chen, X., & Wang, Z. L. (2020). The tribovoltaic effect and

electron transfer at a liquid-semiconductor interface. *Nano Energy*, *76*.

34. Zheng, M., Lin, S., Zhu, L., Tang, Z., & Wang, Z. L. (2021). Effects of Temperature on the Tribovoltaic Effect at Liquid-Solid Interfaces. *Advanced Materials Interfaces*, *9*(3).

35. Le, J., Fan, Q., Perez-Martinez, L., Cuesta, A., & Cheng, J. (2018). Theoretical insight into the vibrational spectra of metal-water interfaces from density functional theory based molecular dynamics. *Phys Chem Chem Phys*, *20*(17), 11554-11558.

36. Q. T. N., & , C. P. V., Thanh Ha Nguyen and Kyoung Kwan Ahn. (2022). A Direct-Current Triboelectric Nanogenerator Energy Harvesting System Based on Water Electrification for Self-Powered Electronics. *Applied Science*.

37. Lin, S., Xu, C., Xu, L., & Wang, Z. L. (2020). The overlapped electron-cloud model for electron transfer in contact electrification. *Advanced Functional Materials*, *30*(11), 1909724.

38. Luo, J., & Wang, Z. L. (2020). Recent progress of triboelectric nanogenerators: From fundamental theory to practical applications. *EcoMat*, *2*(4), e12059.

39. Wang, Z. L. (2021). From contact electrification to triboelectric nanogenerators. *Reports on Progress in Physics*, *84*(9), 096502.

40. Lin, S., Chen, X., & Wang, Z. L. (2021). Contact Electrification at the Liquid–Solid Interface. *Chemical Reviews*.

41. Wang, Z. L., & Wang, A. C. (2019). On the origin of contact-electrification. *Materials Today*.

42. Lin, S., & Lin Wang, Z. (2022). The tribovoltaic effect. *Materials Today*.

43. Sriphan, S., & Vittayakorn, N. (2023). Tribovoltaic effect: Fundamental

working mechanism and emerging applications. *Materials Today Nano*, *22*.

44. Zheng, M., Lin, S., Tang, Z., Feng, Y., & Wang, Z. L. (2021). Photovoltaic effect and tribovoltaic effect at liquid-semiconductor interface. *Nano Energy*, *83*.

45. Zhang, Z., Jiang, D., Zhao, J., Liu, G., Bu, T., Zhang, C., & Wang, Z. L. (2020). Tribovoltaic Effect on Metal–Semiconductor Interface for Direct-Current Low-Impedance Triboelectric Nanogenerators. *Advanced Energy Materials*, *10*(9).

46. Zheng, M., Lin, S., Xu, L., Zhu, L., & Wang, Z. L. (2020). Scanning Probing of the Tribovoltaic Effect at the Sliding Interface of Two Semiconductors. *Adv Mater*, *32*(21), e2000928.

47. Huang, Y., Liu, D., Gao, X., Zhu, J., Zhang, Y., & Zhang, M. (2022). Flexible Liquid-Based Continuous Direct-Current Tribovoltaic Generators Enable Self-Powered Multi-Modal Sensing. *Advanced Functional Materials*, *33*(1).

48. Atlas, I., & Ramon, G. Z. (2018). Periodic energy conversion in an electric-double-layer capacitor. *J Colloid Interface Sci*, *530*, 675-685.

49. Hartel, A., Janssen, M., Samin, S., & van Roij, R. (2015). Fundamental measure theory for the electric double layer: implications for blue-energy harvesting and water desalination. *J Phys Condens Matter*, *27*(19), 194129.

50. Moon, J. K., Song, M. W., & Pak, H. K. (2015). Investigation of surface charge density on solid-liquid interfaces by modulating the electrical double layer. *J Phys Condens Matter*, *27*(19), 194102.

51. Niu, S., Liu, Y., Chen, X., Wang, S., Zhou, Y. S., Lin, L., Xie, Y., & Wang, Z. L. (2015). Theory of freestanding triboelectric-layer-based nanogenerators. *Nano Energy*, *12*, 760-774.

52. Niu, S., Liu, Y., Wang, S., Lin, L., Zhou, Y. S., Hu, Y., & Wang, Z. L. (2013). Theory of sliding-mode triboelectric nanogenerators. *Adv Mater*, *25*(43),

6184-6193.

53. Niu, S., Wang, S., Lin, L., Liu, Y., Zhou, Y. S., Hu, Y., & Wang, Z. L. (2013). Theoretical study of contact-mode triboelectric nanogenerators as an effective power source. *Energy & Environmental Science*, *6*(12).

54. Niu, S., Liu, Y., Wang, S., Lin, L., Zhou, Y. S., Hu, Y., & Wang, Z. L. (2014). Theoretical Investigation and Structural Optimization of Single-Electrode Triboelectric Nanogenerators. *Advanced Functional Materials*, *24*(22), 3332-3340.

55. Niu, S., & Wang, Z. L. (2015). Theoretical systems of triboelectric nanogenerators. *Nano Energy*, *14*, 161-192.

56. Jiang, T., Chen, X., Han, C. B., Tang, W., & Wang, Z. L. (2015). Theoretical Study of Rotary Freestanding Triboelectric Nanogenerators. *Advanced Functional Materials*, *25*(19), 2928-2938.

57. Shao, J., Willatzen, M., & Wang, Z. L. (2020). Theoretical modeling of triboelectric nanogenerators (TENGs). *Journal of Applied Physics*, *128*(11).

58. Xu, W., Zheng, H., Liu, Y., Zhou, X., Zhang, C., Song, Y., Deng, X., Leung, M., Yang, Z., Xu, R. X., Wang, Z. L., Zeng, X. C., & Wang, Z. (2020). A droplet-based electricity generator with high instantaneous power density. *Nature*.

59. Wu, H., Mendel, N., van den Ende, D., Zhou, G., & Mugele, F. (2020). Energy Harvesting from Drops Impacting onto Charged Surfaces. *Phys Rev Lett*, *125*(7), 078301.

60. Jun Wu *, J. C., Hailin Bi , Jun Zhang , Qing Cao *. (2023). Liquid-solid contact electrification and its effect on the formation of electric double layer: An atomic-level investigation. *Nano Energy*.

61. Nan, Y., Shao, J., Willatzen, M., & Wang, Z. L. (2022). Understanding Contact Electrification at Water/Polymer Interface. *Research 2022*, 9861463.

62. Dong, Y., Xu, S., Zhang, C., Zhang, L., Wang, D., Xie, Y., Luo, N., Feng, Y., Wang, N., & Feng, M. (2022). Gas-liquid two-phase flow-based triboelectric nanogenerator with ultrahigh output power. *SCIENCE ADVANCES*, *8*(48), eadd0464.

63. Wang, D., Zhang, D., Tang, M., Zhang, H., Sun, T., Yang, C., Mao, R., Li, K., & Wang, J. (2022). Ethylene chlorotrifluoroethylene/hydrogel-based liquid-solid triboelectric nanogenerator driven self-powered MXene-based sensor system for marine environmental monitoring. *Nano Energy*, *100*, 107509.

64. Dong, Y., Wang, N., Yang, D., Wang, J., Lu, W., & Wang, D. (2023). Robust Solid-Liquid Triboelectric Nanogenerators: Mechanisms, Strategies and Applications. *Advanced Functional Materials*, 2300764.

65. Khan, A., Ginnaram, S., Wu, C.-H., Lu, H.-W., Pu, Y.-F., Wu, J. I., Gupta, D., Lai, Y.-C., & Lin, H.-C. (2021). Fully self-healable, highly stretchable, and anti-freezing supramolecular gels for energy-harvesting triboelectric nanogenerator and self-powered wearable electronics. *Nano Energy*, *90*, 106525.

66. Nawaz, S. M., Saha, M., Sepay, N., & Mallik, A. (2022). Energy-from-waste: A triboelectric nanogenerator fabricated from waste polystyrene for energy harvesting and self-powered sensor. *Nano Energy*, *104*, 107902.

67. Singh, S., Tripathi, R. K., Gupta, M. K., Dzhardimalieva, G. I., Uflyand, I. E., & Yadav, B. (2021). 2-D self-healable polyaniline-polypyrrole nanoflakes based triboelectric nanogenerator for self-powered solar light photo detector with DFT study. *Journal of Colloid and Interface Science*, *600*, 572-585.

68. Yang, H., Fan, F. R., Xi, Y., & Wu, W. (2021). Design and engineering of high-performance triboelectric nanogenerator for ubiquitous unattended devices. *EcoMat*, *3*(2), e12093.

69. Zhan, F., Wang, A. C., Xu, L., Lin, S., Shao, J., Chen, X., & Wang, Z. L. (2020). Electron transfer as a liquid droplet contacting a polymer surface. *ACS Nano*, *14*(12), 17565-17573.

70. Tang, W., Han, Y., Han, C. B., Gao, C. Z., Cao, X., & Wang, Z. L. (2015). Self-powered water splitting using flowing kinetic energy. *Adv Mater*, *27*(2), 272-276.

71. Zou, Y., Tan, P., Shi, B., Ouyang, H., Jiang, D., Liu, Z., Li, H., Yu, M., Wang, C., Qu, X., Zhao, L., Fan, Y., Wang, Z. L., & Li, Z. (2019). A bionic stretchable nanogenerator for underwater sensing and energy harvesting. *Nat Commun*, *10*(1), 2695.

72. Phan, H., Hoa, P. N., Tam, H. A., & Thang, P. D. (2021). Q-switched pulsed laser direct writing of aluminum surface micro/nanostructure for triboelectric performance enhancement. *Journal of Science: Advanced Materials and Devices*, *6*(1), 84-91.

73. Suo, X., Li, B., Ji, H., Mei, S., Miao, S., Gu, M., Yang, Y., Jiang, D., Cui, S., & Chen, L. (2023). Dielectric Layer Doping for Enhanced Triboelectric Nanogenerators. *Nano Energy*, 108651.

74. Wu, C., Wang, A. C., Ding, W., Guo, H., & Wang, Z. L. (2019). Triboelectric nanogenerator: a foundation of the energy for the new era. *Advanced Energy Materials*, *9*(1), 1802906.

75. Huang, J., Fu, X., Liu, G., Xu, S., Li, X., Zhang, C., & Jiang, L. (2019). Micro/nano-structures-enhanced triboelectric nanogenerators by femtosecond laser direct writing. *Nano Energy*, *62*, 638-644.

76. Wang, S., Lin, L., & Wang, Z. L. (2012). Nanoscale triboelectric-effect-enabled energy conversion for sustainably powering portable electronics. *Nano Lett*,

12(12), 6339-6346.

77. Zheng, Q. (2016). Biodegradable triboelectric nanogenerator as a life-time designed implantable power source. *SCIENCE ADVANCES*.

78. Chen, S., Wang, N., Ma, L., Li, T., Willander, M., Jie, Y., Cao, X., & Wang, Z. L. (2016). Triboelectric Nanogenerator for Sustainable Wastewater Treatment via a Self-Powered Electrochemical Process. *Advanced Energy Materials*, *6*(8).

79. Liu, H., Xu, Y., Xiao, Y., Zhang, S., Qu, C., Lv, L., Chen, H., & Song, G. (2022). Highly Adaptive Liquid–Solid Triboelectric Nanogenerator-Assisted Self-Powered Water Wave Motion Sensor. *ACS Applied Electronic Materials*, *4*(8), 3870-3879.

80. Cheng, G., Lin, Z.-H., Du, Z., & Wang, Z. L. (2014). Simultaneously harvesting electrostatic and mechanical energies from flowing water by a hybridized triboelectric nanogenerator. *ACS Nano*, *8*(2), 1932-1939.

81. Chen, J., Guo, H., Zheng, J., Huang, Y., Liu, G., Hu, C., & Wang, Z. L. (2016). Self-Powered Triboelectric Micro Liquid/Gas Flow Sensor for Microfluidics. *ACS Nano*, *10*(8), 8104-8112.

82. Tang, M., Guan, Q., Wu, X., Zeng, X., Zhang, Z., & Yuan, Y. (2019). A high-efficiency multidirectional wind energy harvester based on impact effect for self-powered wireless sensors in the grid. *Smart Materials and Structures*, *28*(11), 115022.

83. Qiu, C., Wu, F., Lee, C., & Yuce, M. R. (2020). Self-powered control interface based on Gray code with hybrid triboelectric and photovoltaics energy harvesting for IoT smart home and access control applications. *Nano Energy*, *70*, 104456.

84. Munirathinam, K., Kim, D.S., Shanmugasundaram, A., Park, J., Jeong, Y.-

J., & Lee, D.W. (2022). Flowing water-based tubular triboelectric nanogenerators for sustainable green energy harvesting. *Nano Energy*, *102*, 107675.

85. Wang, Z. L., & Wu, W. (2012). Nanotechnology-enabled energy harvesting for self-powered micro-/nanosystems. *Angewandte Chemie International Edition*, *51*(47), 11700-11721.

86. Pavana, H., & Deshpande, R. (2020). Energy harvesting techniques for monitoring devices in smart grid application. 2020 Third International Conference on Advances in Electronics, Computers and Communications (ICAECC),

87. Maharjan, P., Salauddin, M., Cho, H., & Park, J. Y. (2018). An indoor power line based magnetic field energy harvester for self-powered wireless sensors in smart home applications. *Applied Energy*, *232*, 398-408.

88. Liu, L., Guo, X., & Lee, C. (2021). Promoting smart cities into the 5G era with multi-field Internet of Things (IoT) applications powered with advanced mechanical energy harvesters. *Nano Energy*, *88*, 106304.

89. Liu, H., Fu, H., Sun, L., Lee, C., & Yeatman, E. M. (2021). Hybrid energy harvesting technology: From materials, structural design, system integration to applications. *Renewable and sustainable energy reviews*, *137*, 110473.

90. Lin, S., & Wang, Z. L. (2021). Scanning triboelectric nanogenerator as a nanoscale probe for measuring local surface charge density on a dielectric film. *Applied Physics Letters*, *118*(19).

91. Zhang, J., Lin, S., Zheng, M., & Wang, Z. L. (2021). Triboelectric Nanogenerator as a Probe for Measuring the Charge Transfer between Liquid and Solid Surfaces. *ACS Nano*.

92. Zhang, J., Lin, S., & Wang, Z. L. (2023). Triboelectric Nanogenerator Array as a Probe for In Situ Dynamic Mapping of Interface Charge Transfer at a

Liquid-Solid Contacting. *ACS Nano*.

93. Wang, Z. L., Jiang, T., & Xu, L. (2017). Toward the blue energy dream by triboelectric nanogenerator networks. *Nano Energy*, *39*, 9-23.

94. Wang, W., Yang, D., Yan, X., Wang, L., Hu, H., & Wang, K. (2023). Triboelectric nanogenerators: The beginning of blue dream. *Frontiers of Chemical Science and Engineering*, *17*(6), 635-678.

95. Wang, H., Xu, L., & Wang, Z. (2021). Advances of high-performance triboelectric nanogenerators for blue energy harvesting. *Nanoenergy Advances*, *1*(1), 32-57.

96. Liu, L., Shi, Q., Ho, J. S., & Lee, C. (2019). Study of thin film blue energy harvester based on triboelectric nanogenerator and seashore IoT applications. *Nano Energy*, *66*, 104167.

97. Liu, G., Xiao, L., Chen, C., Liu, W., Pu, X., Wu, Z., Hu, C., & Wang, Z. L. (2020). Power cables for triboelectric nanogenerator networks for large-scale blue energy harvesting. *Nano Energy*, *75*, 104975.

98. Khan, U., & Kim, S.-W. (2016). Triboelectric nanogenerators for blue energy harvesting. *ACS Nano*, *10*(7), 6429-6432.

99. Feng, J., Zhou, H., Cao, Z., Zhang, E., Xu, S., Li, W., Yao, H., Wan, L., & Liu, G. (2022). 0.5 m Triboelectric Nanogenerator for Efficient Blue Energy Harvesting of All-Sea Areas. *Advanced Science*, *9*(35), 2204407.

100. Chen, J., Yang, J., Li, Z., Fan, X., Zi, Y., Jing, Q., Guo, H., Wen, Z., Pradel, K. C., & Niu, S. (2015). Networks of triboelectric nanogenerators for harvesting water wave energy: a potential approach toward blue energy. *ACS Nano*, *9*(3), 3324-3331.

101. Li, X., Tao, J., Wang, X., Zhu, J., Pan, C., & Wang, Z. L. (2018). Networks

of High Performance Triboelectric Nanogenerators Based on Liquid-Solid Interface Contact Electrification for Harvesting Low-Frequency Blue Energy. *Advanced Energy Materials*, *8*(21).

102. Zhao, E., Jiang, K., Li, B., Liu, X., Zeng, F., Chen, L., Zhang, H., & Zhu, Z. (2022). Classification and utilization of waste electronic components based on triboelectric nanogenerator. *Nanotechnology*, *33*(49), 495401.

103. Rani, G. M., Wu, C.M., Motora, K. G., & Umapathi, R. (2022). Waste-to-energy: Utilization of recycled waste materials to fabricate triboelectric nanogenerator for mechanical energy harvesting. *Journal of Cleaner Production*, *363*, 132532.

104. Ahn, J., Kim, J. S., Jeong, Y., Hwang, S., Yoo, H., Jeong, Y., Gu, J., Mahato, M., Ko, J., & Jeon, S. (2022). All-Recyclable Triboelectric Nanogenerator for Sustainable Ocean Monitoring Systems. *Advanced Energy Materials*, *12*(30), 2201341.

105. Zhou, J., Tao, Y., Liu, W., Sun, H., Wu, W., Song, C., Xue, R., Jiang, T., Jiang, H., & Ren, Y. (2021). Self-powered AC electrokinetic microfluidic system based on triboelectric nanogenerator. *Nano Energy*, *89*, 106451.

106. Yu, J., Wei, X., Guo, Y., Zhang, Z., Rui, P., Zhao, Y., Zhang, W., Shi, S., & Wang, P. (2021). Self-powered droplet manipulation system for microfluidics based on triboelectric nanogenerator harvesting rotary energy. *Lab on a Chip*, *21*(2), 284-295.

107. Nie, J., Ren, Z., Shao, J., Deng, C., Xu, L., Chen, X., Li, M., & Wang, Z. L. (2018). Self-powered microfluidic transport system based on triboelectric nanogenerator and electrowetting technique. *ACS Nano*, *12*(2), 1491-1499.

108. Nie, J., Ren, Z., Bai, Y., Shao, J., Jiang, T., Xu, L., Chen, X., & Wang, Z.

L. (2019). Long distance transport of microdroplets and precise microfluidic patterning based on triboelectric nanogenerator. *Advanced Materials Technologies*, *4*(1), 1800300.

109. Nie, J., Chen, X., & Wang, Z. L. (2019). Electrically responsive materials and devices directly driven by the high voltage of triboelectric nanogenerators. *Advanced Functional Materials*, *29*(41), 1806351.

110. Li, X., Tat, T., & Chen, J. (2021). Triboelectric nanogenerators for self-powered drug delivery. *Trends in Chemistry*, *3*(9), 765-778.

111. Chen, J., Guo, H., Zheng, J., Huang, Y., Liu, G., Hu, C., & Wang, Z. L. (2016). Self-powered triboelectric micro liquid/gas flow sensor for microfluidics. *ACS Nano*, *10*(8), 8104-8112.

112. Wang, Z. L. (2020). Triboelectric Nanogenerator (TENG)—Sparking an Energy and Sensor Revolution. *Advanced Energy Materials*, *10*(17).

113. Lacks, D. J., & Shinbrot, T. (2019). Long-standing and unresolved issues in triboelectric charging. *Nature Reviews Chemistry*, *3*(8), 465-476.

114. Shaw, P. (1926). The electrical charges from like solids. *Nature*, *118*(2975), 659-660.

115. Moon, J. K., Jeong, J., Lee, D., & Pak, H. K. (2013). Electrical power generation by mechanically modulating electrical double layers. *Nature Communications*, *4*(1), 1487.

116. Moon, J. K., Song, M. W., & Pak, H. K. (2015). Investigation of surface charge density on solid–liquid interfaces by modulating the electrical double layer. *Journal of Physics: Condensed Matter*, *27*(19), 194102.

117. Favaro, M., Jeong, B., Ross, P. N., Yano, J., Hussain, Z., Liu, Z., & Crumlin, E. J. (2016). Unravelling the electrochemical double layer by direct

probing of the solid/liquid interface. *Nature Communications*, *7*(1), 12695.

118. Yun, F. F., Yu, Z., He, Y., Jiang, L., Wang, Z., Gu, H., & Wang, X. (2020). Voltage-induced penetration effect in liquid metals at room temperature. *National science review*, *7*(2), 366-372.

119. Lin, Z. H., Cheng, G., Lee, S., Pradel, K. C., & Wang, Z. L. (2014). Harvesting water drop energy by a sequential contact-electrification and electrostatic-induction process. *Advanced Materials*, *26*(27), 4690-4696.

120. Helseth, L., & Guo, X. (2015). Contact electrification and energy harvesting using periodically contacted and squeezed water droplets. *Langmuir*, *31*(10), 3269-3276.

121. Tang, W., Chen, B. D., & Wang, Z. L. (2019). Recent progress in power generation from water/liquid droplet interaction with solid surfaces. *Advanced Functional Materials*, *29*(41), 1901069.

122. Chatterjee, S., Burman, S. R., Khan, I., Saha, S., Choi, D., Lee, S., & Lin, Z.-H. (2020). Recent advancements in solid–liquid triboelectric nanogenerators for energy harvesting and self-powered applications. *Nanoscale*, *12*(34), 17663-17697.

123. Shi, Q., Wang, H., Wu, H., & Lee, C. (2017). Self-powered triboelectric nanogenerator buoy ball for applications ranging from environment monitoring to water wave energy farm. *Nano Energy*, *40*, 203-213.

124. Choi, D., Lee, S., Park, S. M., Cho, H., Hwang, W., & Kim, D. S. (2015). Energy harvesting model of moving water inside a tubular system and its application of a stick-type compact triboelectric nanogenerator. *Nano Research*, *8*, 2481-2491.

125. Li, X., Tao, J., Zhu, J., & Pan, C. (2017). A nanowire based triboelectric nanogenerator for harvesting water wave energy and its applications. *APL*

Materials, *5*(7).

126. Tian, Y., Wang, Z., Fu, J., Xia, K., Lu, J., Tang, H., Rabia, K., Chen, H., Zhu, Z., & Zhang, Q. (2019). FeSe 2/carbon nanotube hybrid lithium-ion battery for harvesting energy from triboelectric nanogenerators. *Chemical Communications*, *55*(73), 10960-10963.

127. Xia, K., Tang, H., Fu, J., Tian, Y., Xu, Z., Lu, J., & Zhu, Z. (2020). A high strength triboelectric nanogenerator based on rigid-flexible coupling design for energy storage system. *Nano Energy*, *67*, 104259.

128. Yang, X., Chan, S., Wang, L., & Daoud, W. A. (2018). Water tank triboelectric nanogenerator for efficient harvesting of water wave energy over a broad frequency range. *Nano Energy*, *44*, 388-398.

129. Lefrou, C., Fabry, P., & Poignet, J.-C. (2012). *Electrochemistry: the basics, with examples*. Springer Science & Business Media.

130. Holze, R. (1994). CMA Brett, AMO Brett: Electrochemistry—Principles, methods and applications, OXford University Press, Oxford, ISBN 0-19-855388-9, 1993, 427 pages. In: Wiley Online Library.

131. Knoblauch, O. (1902). Versuche über die Berührungselektrizität. *Zeitschrift für Physikalische Chemie*, *39*(1), 225-244.

132. Niu, S., Wang, S., Lin, L., Liu, Y., Zhou, Y. S., Hu, Y., & Wang, Z. L. (2013). Theoretical study of contact-mode triboelectric nanogenerators as an effective power source. *Energy & Environmental Science*, *6*(12), 3576-3583.

133. Shao, J., Liu, D., Willatzen, M., & Wang, Z. L. (2020). Three-dimensional modeling of alternating current triboelectric nanogenerator in the linear sliding mode. *Applied Physics Reviews*, *7*(1).

134. Shao, J., Willatzen, M., Jiang, T., Tang, W., Chen, X., Wang, J., & Wang,

Z. L. (2019). Quantifying the power output and structural figure-of-merits of triboelectric nanogenerators in a charging system starting from the Maxwell's displacement current. *Nano Energy*, *59*, 380-389.

135. Squires, T. M., & Bazant, M. Z. (2004). Induced-charge electro-osmosis. *Journal of Fluid Mechanics*, *509*, 217-252.

136. Levine, S., & Neale, G. H. (1974). The prediction of electrokinetic phenomena within multiparticle systems. I. Electrophoresis and electroosmosis. *Journal of Colloid and Interface Science*, *47*(2), 520-529.

137. Shao, J., Jiang, T., Tang, W., Chen, X., Xu, L., & Wang, Z. L. (2018). Structural figure-of-merits of triboelectric nanogenerators at powering loads. *Nano Energy*, *51*, 688-697.

138. De Gennes, P. (1985). Statics and Dynamics: Wetting. *Rev. Mod. Phys*, *57*(3), 827-863.

139. Dharmasena, R. D. I. G., Jayawardena, K., Mills, C., Deane, J., Anguita, J., Dorey, R., & Silva, S. (2017). Triboelectric nanogenerators: providing a fundamental framework. *Energy & Environmental Science*, *10*(8), 1801-1811.

140. Dharmasena, R. I. G., Deane, J. H., & Silva, S. R. P. (2018). Nature of power generation and output optimization criteria for triboelectric nanogenerators. *Advanced Energy Materials*, *8*(31), 1802190.

141. Tandon, V., Bhagavatula, S. K., Nelson, W. C., & Kirby, B. J. (2008). Zeta potential and electroosmotic mobility in microfluidic devices fabricated from hydrophobic polymers: 1. The origins of charge. *Electrophoresis*, *29*(5), 1092-1101.

142. Jiang, P., Zhang, L., Guo, H., Chen, C., Wu, C., Zhang, S., & Wang, Z. L. (2019). Signal output of triboelectric nanogenerator at oil–water–solid multiphase interfaces and its application for dual-signal chemical sensing. *Advanced Materials*,

31(39), 1902793.

143. Li, X., Tao, J., Wang, X., Zhu, J., Pan, C., & Wang, Z. L. (2018). Networks of high performance triboelectric nanogenerators based on liquid–solid interface contact electrification for harvesting low-frequency blue energy. *Advanced Energy Materials*, *8*(21), 1800705.

144. Lin, Z. H., Cheng, G., Lin, L., Lee, S., & Wang, Z. L. (2013). Water–solid surface contact electrification and its use for harvesting liquid-wave energy. *Angewandte Chemie International Edition*, *52*(48), 12545-12549.

145. Zhao, X. J., Zhu, G., Fan, Y. J., Li, H. Y., & Wang, Z. L. (2015). Triboelectric charging at the nanostructured solid/liquid interface for area-scalable wave energy conversion and its use in corrosion protection. *ACS Nano*, *9*(7), 7671-7677.

146. Zhu, G., Su, Y., Bai, P., Chen, J., Jing, Q., Yang, W., & Wang, Z. L. (2014). Harvesting water wave energy by asymmetric screening of electrostatic charges on a nanostructured hydrophobic thin-film surface. *ACS Nano*, *8*(6), 6031-6037.

147. Liang, X., Jiang, T., Liu, G., Xiao, T., Xu, L., Li, W., Xi, F., Zhang, C., & Wang, Z. L. (2019). Triboelectric Nanogenerator Networks Integrated with Power Management Module for Water Wave Energy Harvesting. *Advanced Functional Materials*.

148. Tang, W., Chen, B. D., & Wang, Z. L. (2019). Recent Progress in Power Generation from Water/Liquid Droplet Interaction with Solid Surfaces. *Advanced Functional Materials*.

149. Aji, A. S., Nishi, R., Ago, H., & Ohno, Y. (2020). High output voltage generation of over 5 V from liquid motion on single-layer MoS2. *Nano Energy*, *68*.

150. Pan, L., Wang, J., Wang, P., Gao, R., Wang, Y.-C., Zhang, X., Zou, J.-J., &

Wang, Z. L. (2018). Liquid-FEP-based U-tube triboelectric nanogenerator for harvesting water-wave energy. *Nano Research*, *11*(8), 4062-4073.

151. Zhao, X., Zhu, G., Fan, Y, Li, H., and Wang, Z. L. (2015). Triboelectric Charging at the Nanostructured Solid/Liquid Interface for Area-Scalable Wave Energy Conversion and Its Use in Corrosion Protection. *ACS Nano*.

152. Zhang, N., Gu, H., Lu, K., Ye, S., Xu, W., Zheng, H., Song, Y., Liu, C., Jiao, J., Wang, Z., & Zhou, X. (2021). A universal single electrode droplet-based electricity generator (SE-DEG) for water kinetic energy harvesting. *Nano Energy*, *82*.

153. Choi, D., Lee, S., Park, S. M., Cho, H., Hwang, W., & Kim, D. S. (2015). Energy harvesting model of moving water inside a tubular system and its application of a stick-type compact triboelectric nanogenerator. *Nano Research*, *8*(8), 2481-2491.

154. Nie, J., Wang, Z., Ren, Z., Li, S., Chen, X., & Lin Wang, Z. (2019). Power generation from the interaction of a liquid droplet and a liquid membrane. *Nature Communications*, *10*(1).

155. Chatterjee, S., Burman, S. R., Khan, I., Saha, S., Choi, D., Lee, S., & Lin, Z. H. (2020). Recent advancements in solid-liquid triboelectric nanogenerators for energy harvesting and self-powered applications. *Nanoscale*, *12*(34), 17663-17697.

156. Wang, Z. L. (2017). On Maxwell's displacement current for energy and sensors: the origin of nanogenerators. *Materials Today*, *20*(2), 74-82.

157. Wang, Z. L. (2021). From contact electrification to triboelectric nanogenerators. *Rep Prog Phys*, *84*(9).

158. Wang, Z. L. (2021). On the expanded Maxwell’s equations for moving charged media system – General theory, mathematical solutions and applications in

TENG. *Materials Today*.

159. Wang, Z. L. (2022). Maxwell's equations for a mechano-driven, shape-deformable, chargedmedia system, slowly moving at an arbitrary velocity field. *Journal of Physics Communications*.

160. Wang, Z. L. (2019). On the first principle theory of nanogenerators from Maxwell's equations. *Nano Energy*.

161. Yu, Y., Gao, Q., Zhao, D., Li, X., Wang, Z. L., & Cheng, T. (2022). Influence of mechanical motions on the output characteristics of triboelectric nanogenerators. *Materials Today Physics*, *25*.

162. Li, X., Bista, P., Stetten, A. Z., Bonart, H., Schür, M. T., Hardt, S., Bodziony, F., Marschall, H., Saal, A., Deng, X., Berger, R., Weber, S. A. L., & Butt, H.-J. (2022). Spontaneous charging affects the motion of sliding drops. *Nature Physics*, *18*(6), 713-719.

163. Nie, J., Jiang, T., Shao, J., Ren, Z., Bai, Y., Iwamoto, M., Chen, X., & Wang, Z. L. (2018). Motion behavior of water droplets driven by triboelectric nanogenerator. *Applied Physics Letters*, *112*(18).

164. Xu, W. , Zhou, X., Hao, C., Zheng, H, Liu, Y., Yan, X, Yang, Z, Leung, M., Zeng, X, Xu, R., Wang, Z. (2019). SLIPS-TENG: robust triboelectric nanogenerator with optical and charge transparency using slippery interface. *MATERIALS SCIENCE*.

165. Sun, Q., Wang, D., Li, Y., Zhang, J., Ye, S., Cui, J., Chen, L., Wang, Z., Butt, H. J., Vollmer, D., & Deng, X. (2019). Surface charge printing for programmed droplet transport. *Nat Mater*, *18*(9), 936-941.

166. An, J., Wang, Z. M., Jiang, T., Liang, X., & Wang, Z. L. (2019). Whirling-Folded Triboelectric Nanogenerator with High Average Power for Water Wave

Energy Harvesting. *Advanced Functional Materials*.

167. Wang, Z. L. (2014). Triboelectric nanogenerators as new energy technology and self-powered sensors - principles, problems and perspectives. *Faraday Discuss*, *176*, 447-458.

168. Wang, Z. L. (2013). Triboelectric Nanogenerators as New Energy Technology for Self-Powered Systems and as Active Mechanical and Chemical Sensors. *ACS Nano*.

169. Chen, J., Chen, B., Han, K., Tang, W., & Wang, Z. L. (2019). A Triboelectric Nanogenerator as a Self-Powered Sensor for a Soft–Rigid Hybrid Actuator. *Advanced Materials Technologies*.

170. Evans, L., & Stevens, J. T. (1977). Kelvin water dropper revisited. *The Physics Teacher*, *15*(9), 548-549.

171. Lloyd, J. (1980). Lord Kelvin demonstrated. *The Physics Teacher*, *18*(1), 16-24.

172. Sady, M. (1984). The kelvin water dropper: An elementary experience. *The Physics Teacher*, *22*(8), 516-516.

173. Mak, S. (1997). The Kelvin water-drop electrostatic generator—an improved design. *The Physics Teacher*, *35*(9), 549-551.

174. Zhao, S., Castle, G., & Adamiak, K. (2005). The effect of space charge on the performance of an electrostatic induction charging spray nozzle. *Journal of Electrostatics*, *63*(3-4), 261-272.

175. Anaya, D. V., He, T., Lee, C., & Yuce, M. R. (2020). Self-powered eye motion sensor based on triboelectric interaction and near-field electrostatic induction for wearable assistive technologies. *Nano Energy*, *72*, 104675.

176. Gunn, J. (1964). A general expression for electrostatic induction and its

application to semiconductor devices. *Solid-State Electronics*, *7*(10), 739-742.

177. Han, C. B., Du, W., Zhang, C., Tang, W., Zhang, L., & Wang, Z. L. (2014). Harvesting energy from automobile brake in contact and non-contact mode by conjunction of triboelectrication and electrostatic-induction processes. *Nano Energy*, *6*, 59-65.

178. Janasek, D., Schilling, M., Manz, A., & Franzke, J. (2006). Electrostatic induction of the electric field into free-flow electrophoresis devices. *Lab on a Chip*, *6*(6), 710-713.

179. Mostafaie Maynagh, B., Ghobadian, B., Tavakkoli Hashjin, T., & Jahannama, M. (2009). Effect of electrostatic induction parameters on droplets charging for agricultural application. *Journal of Agricultural Science and Technology*, *11*(3), 249-257.

180. Zeng, Q., Chen, A., Zhang, X., Luo, Y., Tan, L., & Wang, X. (2023). A Dual-Functional Triboelectric Nanogenerator Based on the Comprehensive Integration and Synergetic Utilization of Triboelectrification, Electrostatic Induction, and Electrostatic Discharge to Achieve Alternating Current/Direct Current Convertible Outputs. *Advanced Materials*, *35*(7), 2208139.

181. Maski, D., & Durairaj, D. (2010). Effects of electrode voltage, liquid flow rate, and liquid properties on spray chargeability of an air-assisted electrostatic-induction spray-charging system. *Journal of Electrostatics*, *68*(2), 152-158.

182. Chang, J.S., Kelly, A. J., & Crowley, J. M. (1995). *Handbook of electrostatic processes*. CRC Press.

183. Mitcheson, P. D., Sterken, T., He, C., Kiziroglou, M., Yeatman, E., & Puers, R. (2008). Electrostatic microgenerators. *Measurement and Control*, *41*(4), 114-119.

184. Murray, J. S., & Politzer, P. (2011). The electrostatic potential: an overview. *Wiley Interdisciplinary Reviews: Computational Molecular Science*, *1*(2), 153-163.

185. Lee, S., Chung, J., Kim, D. Y., Jung, J.Y., Lee, S. H., & Lee, S. (2016). Cylindrical water triboelectric nanogenerator via controlling geometrical shape of anodized aluminum for enhanced electrostatic induction. *ACS applied materials & interfaces*, *8*(38), 25014-25018.

186. Kaponig, M., Mölleken, A., Nienhaus, H., & Möller, R. (2021). Dynamics of contact electrification. *SCIENCE ADVANCES*, *7*(22), eabg7595.

187. Shao, J., Yang, Y., Yang, O., Wang, J., Willatzen, M., & Wang, Z. L. (2021). Designing rules and optimization of triboelectric nanogenerator arrays. *Advanced Energy Materials*, *11*(16), 2100065.

188. Kim, J., Cho, H., Han, M., Jung, Y., Kwak, S. S., Yoon, H. J., Park, B., Kim, H., Kim, H., & Park, J. (2020). Ultrahigh power output from triboelectric nanogenerator based on serrated electrode via spark discharge. *Advanced Energy Materials*, *10*(44), 2002312.

189. Huang, L., Lin, S., Xu, Z., Zhou, H., Duan, J., Hu, B., & Zhou, J. (2020). Fiber-based energy conversion devices for human-body energy harvesting. *Advanced Materials*, *32*(5), 1902034.

190. Hinchet, R., Yoon, H.-J., Ryu, H., Kim, M.-K., Choi, E.-K., Kim, D.-S., & Kim, S.-W. (2019). Transcutaneous ultrasound energy harvesting using capacitive triboelectric technology. *Science*, *365*(6452), 491-494.

191. Shao, J., Willatzen, M., Shi, Y., & Wang, Z. L. (2019). 3D mathematical model of contact-separation and single-electrode mode triboelectric nanogenerators. *Nano Energy*, *60*, 630-640.

192. Qin, H., Xu, L., Lin, S., Zhan, F., Dong, K., Han, K., Wang, H., Feng, Y.,

& Wang, Z. L. (2022). Underwater energy harvesting and sensing by sweeping out the charges in an electric double layer using an oil droplet. *Advanced Functional Materials*, *32*(18), 2111662.

193. Zhao, X. J., Kuang, S. Y., Wang, Z. L., & Zhu, G. (2018). Highly adaptive solid–liquid interfacing triboelectric nanogenerator for harvesting diverse water wave energy. *ACS Nano*, *12*(5), 4280-4285.

194. Wang, J., Wu, C., Dai, Y., Zhao, Z., Wang, A., Zhang, T., & Wang, Z. L. (2017). Achieving ultrahigh triboelectric charge density for efficient energy harvesting. *Nature Communications*, *8*(1), 88.

195. Vallem, V., Roosa, E., Ledinh, T., Jung, W., Kim, T. i., Rashid-Nadimi, S., Kiani, A., & Dickey, M. D. (2021). A Soft Variable-Area Electrical-Double-Layer Energy Harvester. *Advanced Materials*, *33*(43), 2103142.

196. Su, Y., Wen, X., Zhu, G., Yang, J., Chen, J., Bai, P., Wu, Z., Jiang, Y., & Wang, Z. L. (2014). Hybrid triboelectric nanogenerator for harvesting water wave energy and as a self-powered distress signal emitter. *Nano Energy*, *9*, 186-195.

197. Liang, X., Jiang, T., Liu, G., Xiao, T., Xu, L., Li, W., Xi, F., Zhang, C., & Wang, Z. L. (2019). Triboelectric nanogenerator networks integrated with power management module for water wave energy harvesting. *Advanced Functional Materials*, *29*(41), 1807241.

198. Wang, Z. L. (2022). On the expanded Maxwell's equations for moving charged media system–General theory, mathematical solutions and applications in TENG. *Materials Today*, *52*, 348-363.

199. Wang, Z. L. (2020). On the first principle theory of nanogenerators from Maxwell's equations. *Nano Energy*, *68*, 104272.

200. Yang, Y., Sun, N., Wen, Z., Cheng, P., Zheng, H., Shao, H., Xia, Y., Chen,

C., Lan, H., & Xie, X. (2018). Liquid-metal-based super-stretchable and structure-designable triboelectric nanogenerator for wearable electronics. *ACS Nano*, *12*(2), 2027-2034.

201. Li, Z., Yang, D., Zhang, Z., Lin, S., Cao, B., Wang, L., Wang, Z. L., & Yin, F. (2022). A droplet-based electricity generator for large-scale raindrop energy harvesting. *Nano Energy*, *100*, 107443.

202. Lee, D.M., Rubab, N., Hyun, I., Kang, W., Kim, Y.J., Kang, M., Choi, B. O., & Kim, S.W. (2022). Ultrasound-mediated triboelectric nanogenerator for powering on-demand transient electronics. *SCIENCE ADVANCES*, *8*(1), eabl8423.

203. Huo, Z. Y., Lee, D. M., Jeong, J. M., Kim, Y. J., Kim, J., Suh, I. Y., Xiong, P., & Kim, S. W. (2022). Microbial disinfection with supercoiling capacitive triboelectric nanogenerator. *Advanced Energy Materials*, *12*(15), 2103680.

204. Han, S. A., Seung, W., Kim, J. H., & Kim, S.-W. (2021). Ultrathin noncontact-mode triboelectric nanogenerator triggered by giant dielectric material adaption. *ACS Energy Letters*, *6*(4), 1189-1197.

205. Dong, K., Peng, X., & Wang, Z. L. (2020). Fiber/fabric-based piezoelectric and triboelectric nanogenerators for flexible/stretchable and wearable electronics and artificial intelligence. *Advanced Materials*, *32*(5), 1902549.

206. Ryu, H., Park, H.-m., Kim, M.-K., Kim, B., Myoung, H. S., Kim, T. Y., Yoon, H.J., Kwak, S. S., Kim, J., & Hwang, T. H. (2021). Self-rechargeable cardiac pacemaker system with triboelectric nanogenerators. *Nature Communications*, *12*(1), 4374.

207. Guo, X., Shao, J., Willatzen, M., Yang, Y., & Wang, Z. L. (2022). Theoretical model and optimal output of a cylindrical triboelectric nanogenerator. *Nano Energy*, *92*, 106762.

208. Zhang, N., Zhang, H., Xu, W., Gu, H., Ye, S., Zheng, H., Song, Y., Wang, Z., & Zhou, X. (2022). A droplet-based electricity generator with ultrahigh instantaneous output and short charging time. *Droplet*, *1*(1), 56-64.

209. Gravesen, J., Willatzen, M., Shao, J., & Wang, Z. L. (2022). Energy Optimization of a Mirror-Symmetric Spherical Triboelectric Nanogenerator. *Advanced Functional Materials*, *32*(18), 2110516.

Publication List

1. **You, J.**, Shao, J., He, Y., Yun, F. F., See, K. W., Wang, Z. L., & Wang, X. (2021). High-electrification performance and mechanism of a water–solid mode triboelectric nanogenerator. *ACS nano*, 15(5), 8706-8714.

2. **You, J.**, Shao, J., He, Y., Guo, X., See, K. W., Wang, Z. L., & Wang, X. (2023). Simulation model of a non-contact triboelectric nanogenerator based on electrostatic induction. *EcoMat*, e12392.

3. **You, J.**, Shao, J., He, Y., Guo, X., Yu, Z., See, K. W., Wang, Z. L., & Wang, X. (2023). Interface triboelectricity. *EcoEnergy* (under submission)

4. He, Y., **You, J.**, Dickey, M., & Wang, X. (2023). Controllable Flow and Manipulation of Liquid Metals. *Advanced Functional Materials*, 2309614.

5. He, Y., **You, J.**, Dickey, M., & Wang, X. (2023). Non-contact Transfer of Liquid Metal from an Anode to Cathode without Short Circuiting. *Nature Chemical Engineering* (in press)

6. Guo, X., **You, J.**, Wei, D., Shao, J. & Wang, Z. L. (2023). A generalized model for tribovoltaic nanogenerator. *Applied Physics Reviews* (under review)